Experimental and Theoretical Studies of Aerosol Agglomerates

Thesis by

Paul Jeffrey Drayton

In Partial Fulfillment of the Requirements
for the Degree of
Doctor of Philosophy

California Institute of Technology
Pasadena, California

1997

(Submitted October 3,1996)

To Mum and Dad

Acknowledgements

Five years is a long time to spend on anything, especially when at the end of those five years a coherent and erudite work has to be produced. I would like to thank my advisor, Professor R.C. Flagan for ensuring that these goals were, if not reached, then kept firmly in sight. His time and efforts over the years have been most appreciated, especially his patience and politeness, for not complaining when told he had to review my thesis after a trans-Atlantic flight. I would like to thank my candidacy and thesis committee members for taking the time to review my work and offer suggestions.

No one works in a vacuum, and at Caltech I have had the pleasure of having my atmosphere comprised of many friends and colleagues. I have enjoyed the friendship of and helpful conversations with the members, past and present, of the Flagan/Seinfeld/Cass groups. Thanks to Melissa Lunden for showing me the ways of the lab and having the patience to explain the inner workings of Swagelok. Dr. Shou-hua Zhang has always been there with his consumate skills to fix any problem that was plaguing me in the lab. Thanks also to Patrick Chuang, for sharing his expertise; scientific, musical and sporting. Hali Forstner was always considerate of my extensive use of the cylindrical DMAs and other equipment, especially as the heat of summer drew close. I hope that in time, Denis, Jim and Richard will be able to locate the equipment that I placed in the lab. Rob has been very patient and considerate about being in the office with me during the final crush. Enjoy the window desks Rob, you deserve them. Thanks also to all the members of my Chem E. class, who started out with me five years ago and particularly made the first few years much more fun than they should have been.

Outside of the lab and classroom, I thoroughly enjoyed the weekly meetings of the Treehuggers. The afternoon sessions were always the highlight of the week. Thanks to all those with whom I played, for not complaining when this stiff shot from outside. Thanks to the Chem E. and Real Scared soccer teams for letting me play keeper. Who knew that letting the ball hit the net was a bad thing?

I have been very fortunate in my friends here and at Canterbury. Thanks Neil, Matthew and Andrew for travelling to share our big day. Thanks Neil, for being there to be homesick with, talk rugby, and to keep alive the Kiwi tradition of afternoon tea in this strange land. Four o'clock will long be red door time. Thanks to Mike, Lisa, Pat, Matt, Dave, Moira, Hali, Cecilia, Roger, Chris, Nancy, John, Rich for many dinners eaten, stories told, and trips taken.

Thanks Yvette, for all your love, encouragement and understanding over the course of our studies. Spalding seemed much more pleasant with you just across the hall. Thanks most of all for saying Yes. We both know I wouldn't be typing this if you hadn't been there.

I'd like to thank my family for their unwavering support over the years. Thanks Michael for letting me follow in your footsteps and especially for the suggestion to apply to CalTech. Thanks Lynley for being a friend as well as a great sister. Thank you, Mum and Dad, for having faith in me, planning that I'd go to university and supporting me in my endeavours since then. You were my first teachers and I hope you are proud of what your pupil has become.

Thanks to you, the reader, for picking up this tome. Please blow the dust off before you return it to the shelf.

Abstract

The behavior and properties of aerosol agglomerates were experimentally and theoretically probed. Brownian coagulation coefficient rates for titania aerosol agglomerates of mobility diameters from 20 nm to 250 nm were measured. The experimental results agree reasonably well with the predictions of Rogak and Flagan, with the smallest agglomerates showing some enhancement of the coagulation coefficient by electrical image and van der Waals forces.

In order to analyze the coagulation experiments,the bipolar diffusion charging of aerosol agglomerates was studied. The steady-state bipolar charge distribution of titania agglomerates with primary particle diameters of 6.5 ± 3 nm, were measured using a Tandem Differential Mobility Analyzer (TDMA) system. The experimental results were compared to an extended Fuchs steady-state charge distribution. The agglomerates were more likely to carry multiple charges than the theory predicted. The extended Fuchs theory was found to be strongly dependent on the properties of the ions.

Alignment of non-spherical particles with the electric field in a DMA, can bias size measurements. To investigate this phenomenon, a theoretical study of agglomerate particle alignment was undertaken. The tendency of a particle to align with the imposed field was found to be characterized by the ratio of the Coulombic to the thermal energies, Γ. The electrical mobility ratio Φ, of a linear chain aggregate was calculated to develop the orientation theory. As the number of primary particles increases, Φ reaches a maximum and then declines. Experimental observations of particle alignment were compared to the theoretical predictions with the experimental data showing alignment effects for Γ over 5.0.

Contents

List of Figures

List of Tables

Chapter 1 Introduction

This is not the age of pamphleteers. It is the age of the engineers. The spark-gap is mightier than the pen. Democracy will not be salvaged by men who talk fluently, debate forcefully and quote aptly.

Lancelot Hogben
Science for the Citizen,1938

1.1 Introduction

Aerosols are liquid or solid spherical particles that have formed or been suspended in a gas. The simple geometry of a sphere has facilitated the study of the processes that aerosols undergo; coagulation, condensational growth, and deposition. An aerosol agglomerate is made up of small primary particles that have coagulated at too low a temperature for the primary particles to coalesce or sinter completely within the available time. Agglomerates have complex shapes that preclude exact description of their behavior and properties difficult to obtain. Models for agglomerate properties have drawn heavily from the exact spherical expressions, often comparing agglomerates to a sphere with an equivalent diameter which is defined such that a property such as sedimentation velocity or electrical mobility is the same as that of the agglomerate.

Agglomerates are generally random arrangements of primary particles that show no short range order. Forrest and Witten (1979) observed, however, that the densities of soot agglomerates scale as the radius of the agglomerate to an exponent, later called a fractal dimension (Meakin 1990) This fractal dimension has been used in the study of the behavior and the properties of aerosol agglomerates.

Aerosol agglomerates form by coagulation. In this process two aerosol particles collide and stick together. The resulting particle can, in turn, collide with other particles. When the particles are brought together by their random Brownian motions, the process is called Brownian coagulation. Smoluchowski (1917) derived a population balance for aerosol coagulation. The key parameters in the balance are the coagulation coefficients, also called coagulation kernels, which are the reaction rate coefficients for collision of a particle of size i with a particle of size j. Fuchs (1964) derived approximate expressions for the coagulation rate coefficients of spheres that spanned the continuum to the free molecular regime. The corresponding coagulation coefficients for agglomerates have been suggested theoretically by many authors, but experimental validation has been difficult to obtain. The theoretical coagulation coefficents are included in the models of aerosol processes. For aerosol agglomerates, these models are mostly based on empirical relations. Also the studies of coagulation coefficents have dealt with monodisperse coagulation and not with the coagulation of differently sized particles. As the difference in size between two spherical particles increases then the coagulation rate also increases. For aerosol

agglomerates, the exact nature of this trend is not fully understood.

The first chapter of this thesis describes an experimental study of the Brownian coagulation of aerosol agglomerates that was conducted in order to obtain coagulation coefficients. To validate the experimental setup and procedures, coagulation coefficents for spherical particles were measured and compared to the Fuchs theory. With this satisfactorily completed, titania agglomerates with a primary particle diameter of 6nm, and overall particle mobility diameters up to 250nm were produced and classified using Differential Mobility Analyzers (DMAs). The sized aerosols were then introduced into a laminar flow pipe reactor with a 380 second residence time. The outlet particle concentrations from the reactor were analyzed and coagulation coefficents obtained. The experimental coagulation coefficients were compared to the theory of Rogak and Flagan (1992) which takes into account the fractal dimension of the agglomerate and the primary particle size.

This experimental investigation into Brownian coagulation raised additional questions about the agglomerates. To invert the size distributions from the coagulation experiments, knowledge of the distribution of electrical charges on the agglomerates was needed. The charging of spherical particles has been studied extensively, but little was known about the charging of transition regime agglomerates with primary particles in the free molecular regime. Indeed, no data was available in the literature about the steady state distribution of charges on agglomerates comprised of primary particles below 20nm in diameter. To determine the charge distribution for the titania agglomerates used in the coagulation study, the steady-state charge distribution produced upon exposure to a bipolar ion cloud was measured. Chapter 2 reports on these experiments and their interpretation.

Agglomerates differ from spheres in another important way. The projected area of a sphere in the flow direction is independent of its orientation. The same cannot be said for an agglomerate, especially for agglomerates with small fractal dimensions. The alignment of nonspherical particles in shear flow has been known in the colloids field for many years (Alexander and Johnson 1949). Alignment of aerosol particles in laminar shear flow has also been predicted by Krushkal and Gallily (1984).

The DMA classifies particles with respect to their migration velocities in an ap-

plied electric field. The ratio of the steady-state migration velocity to the electric field strength is known as the electrical mobility. A sphere's electrical mobility is independent of its orientation but as discussed earlier, the agglomerate's drag can change with orientation. To determine when agglomerates are aligned in an electrostatic mobility analyzer, a theoretical investigation was undertaken and can be found in the third chapter.

The orientation was found to depend on the ratio of the Coulombic and thermal energies. The example of a linear chain aggregate comprised of equally sized primary particles was used to show how orientation varied with the size and number of primary particles. Comparisons were made to experimental data of agglomerate orientation.

The characterization of the CalTech cylindrical DMA that was used in this study and the computer codes used in size distribution inversion can be found in the appendices.

Chapter 2 An Experimental Study of the Brownian Coagulation of Aerosol Agglomerates

Dust as we are, the immortal spirit grows
Like harmony in music; there is a dark
Inscrutable workmanship that reconciles
Discordant elements, makes them cling together
In one society.

William Wordsworth
The Prelude (1850) bk.1,l.340

2.1 Abstract

Experiments were carried out to determine the Brownian coagulation rate of aerosol agglomerates in the transition size regime. Two TSI 3077 differential mobility analysers (DMAs) were used to provide monomobility aerosols. The particles were then introduced into a reactor with a residence time of 360 seconds. Two cylindrical DMAs and flow controllers were used to analyze the aerosols before and after the reactor. The changes in the size distributions were analyzed to determine coagulation coefficients. The experimental method was validated by comparison of coagulation of NaCl particles to Fuchs theory (1964). Experiments were also carried out to determine particle loss rates and charging probability of the agglomerates. The experimental results for agglomerates were compared to the theory of Rogak and Flagan (1992). The coagulation of agglomerates of the same mobility diameter followed the trend of Rogak and Flagan's theory for agglomerates with a primary particle diameter of 1nm. At mobility sizes below 40nm, the experimental coagulation coefficients were significantly above the theory, and the difference is attributed to van der Waals and image force enhancement of the coagulation.

2.2 Introduction

High temperature processes often produce large numbers of fine aerosol particles by homogeneous nucleation from the vapor phase. These particles then grow by Brownian coagulation. When coagulation takes place at temperatures well below the melting point of the material, low density agglomerates result. Forrest and Witten (1979) first reported that these particles have structures that are similar over a wide range of scales and that can be characterized in terms of power laws. These power law descriptions of aggregate structures have since been termed fractals (Meakin 1990). Specifically, the masses of the aggregate particles, m, scale with the charcteristic radius as

$$m \sim r^{D_f} \tag{2.1}$$

where D_f is the so-called mass fractal dimension.

Since that initial discovery, the concept of fractal particle structures has been used to model the properties of such particles (Rogak et al., 1993) and the dynamics of their formations and growth (Wu and Friedlander, 1993; Gutsch et al., 1995; Vemury and Pratsinis, 1994). Direct experimental validation has, however, been limited.

Aerosol aggregation takes place when very large numbers of particles are produced by homogeneous nucleation. The extreme supersaturations that produce such nucleation are found in high temperature systems where refractory materials are first vaporized (or produced by chemical reaction) and then condense as the gases cool. The Brownian motion of the resulting particles leads to collisions and growth. At high temperatures the particles may coalesce completely upon coagulation, but as the gases cool, a point is reached where coalescence slows and aggregate particles begin to form. The observed fractal structures are, therefore, the end result of a complex chain of events.

Numerous investigations have developed models of the various kinetic processes that contribute to aggregate and aerosol evolution. The earliest models focused on the relationships between the stochastic nature of the growth process and the resulting particle structure. Models of diffusion limited aggregation (DLA), wherein particles were allowed to grow by accretion of the smallest subunits (primary particles) produced fundamentally different structures than did cluster-cluster aggregation (CCA), wherein an ensemble of particles evolves by coagulation with one another. Although there are differences in the detailed structures produced by either model, depending on the transport rules used in the simulation, the DLA model consistently produced aggregates of higher fractal dimension ($D_f \sim 2.5$) and density than the CCA model ($D_f \sim 1.8$). Observed particle structures are generally consistent with the cluster-cluster aggregation model with $D_f \sim 1.8$, as might be expected for a system in which particles are formed in a burst of nucleation and then evolve as an ensemble by Brownian coagulation.

The rate of Brownian coagulation is determined by the details of the diffusive motion of the particles and the geometry of collisions. Aerosol agglomeration usually begins with particles that are much smaller than the mean free path of the gas molecules, but frequently continues to sizes in the transition regime between free molecular and continuum gas dynamics. Mountain et al. (1986) derived models of Brownian coagulation in the free molecular regime, and proposed an interpolation procedure for the transition regime. Rogak and Flagan (1992), Vemury et al.(1994), among others, have proposed

refinements to that initial model.

A number of investigators have compared model predictions with experimental observations of aggregate aerosol evolution in flames and aerosol reactors (Koch and Friedlander, 1991; Matsoukas and Friedlander, 1991; Kruis et al., 1993). Efforts to validate models of the aerosol aggregation kinetics have provided qualitative support for the models, but quantitative validation of the models has not been possible due to the many processes that contribute to the aerosol evolution in such experiments.

Koch and Friedlander (1990) theoretically examined the structure of an agglomerate after coalescence and agglomeration. They found that the final primary particle size was dependent on the material properties and the process properties (cooling rate and temperature). Kruis et al. (1993) developed a model for a fractal aggregate undergoing coagulation and sintering. The model was applied to a silicon powder formed by laser heating. Small primary particle size and high temperatures were found to favor sintering. The outer boundary of the flame was cooler and more dilute and produced smaller, more aggregated particles than the center region of the flame.

We have taken a different approach to model validation. Rather than testing the predictions of comprehensive models against observations from systems of practical interest, we have designed experiments to probe individual processes, separating the coalescence process from that of aggregation. Lunden (1996) described studies of the sintering of aerosol agglomerates ranging from aggregates containing two spherical primary particles of approximately equal size to mobility classified fractal aggregates. These experiments were conducted at sufficiently low concentrations that coagulation did not occur significantly during sintering. The present experiments were conducted at temperatures low enough to preclude sintering.

So far, we have assumed that the Brownian motion of the particles is the only mechanism which causes the particles to coagulate. Attractive interparticle forces can accelerate coagulation beyond the rate predicted for purely diffusional motions. Marlow (1980) examined the enhancement of coagulation by Lifshitz-van der Waals and electrical image forces. He predicted an enhancement factor of 1.94 for two 10nm water particles coagulating at atmospheric pressure. The enhancement was largest for collisions involving particles smaller than 10nm. Huang et al. (1990) modeled the coagulation of both neutral

and charged particles. They found that the image attraction can exponentially increase coagulation in the free molecular regime as both particle sizes decrease. Kerminen (1994) using a sectional model found enhancement of coagulation, for particles below 50nm in diameter, by van der Waals forces.

The enhancement has also been seen experimentally. Okuyama et al. (1984) studied the coagulation of ultrafine particles, using a laminar pipe flow reactor. Coagulation was found to be enhanced as the particle size diminished, with silver particles, below 20nm in diameter, having enhancements factors of 5-10. Majerowicz et al. (1990) reported an enhancement factor of 6 ± 1.3 for silver particles with mobility diameters of 6nm.

In this paper we describe a system that we have developed for direct measurement of collision frequency functions for aerosol aggregation without the complications of coalescence, structural rearrangements and coagulation enhancement effects. The coagulation rate constant has been measured for titania aggregates with primary particles that are much smaller than the mean free path but for which the total length of the aggregate extends into the transition regime. Measurements have been made for evaluation of coagulations rates for particles of equal size and for particles of differing sizes.

2.2.1 Coagulation Theory

Spherical particles have a well-known Brownian coagulation theory derived by Smoluchowski (1917), which was then further developed by Fuchs (1964). An understanding of the key components of this theory will help to design experiments to determine the Brownian coagulation rate. Assuming discrete particle sizes such that the volume of a particle in size class j is $v_j = j\, v_1$, and that particles grow only by coagulation, one may derive a population balance for particles of size j (Seinfeld, 1986),

$$\frac{dN_j}{dt} = \frac{1}{2}\sum_{i=1}^{j-1} K_{i,j-1} N_i N_{j-1} - N_j \sum_{1=1}^{\infty} K_{ij} N_i. \tag{2.2}$$

The first term on the right-hand side accounts for the formation of a size j particle by coagulation of smaller particles. While, the second term describes the loss of particles

of size j by coagulation with particles of any other size. The K_{ij} factors are coagulation rate coefficients for particles of size i coagulating with particles of size j. N_i denotes the number concentration of particles of size i. The simplest example of this equation is the case of size j monodisperse spheres coagulating. In this example there are no smaller particles, so the addition term can be ignored. Similarly at small times there are no larger particles and the loss term is only from collisions of like sized spheres. The equation simplifies to;

$$\frac{dN_j}{dt} = -K_{jj}N_j^2. \tag{2.3}$$

This equation can be easily integrated and rearranged to give an expression for the coagulation coefficient in terms of the concentrations of the particles at the initial time N_1^0 and the concentration at a later time N_1^t. The relation is;

$$K_{11} = \frac{N_1^0 - N_1^t}{N_1^0 N_1^t t}. \tag{2.4}$$

Therefore, to conduct experiments to determine the Brownian coagulation coefficients, theory tells us that we should know the concentration of a monodisperse aerosol at an initial time, and at some later time. Also to ensure that only coagulation of like sized particles occurs, coagulation should not produce large concentrations of large particles. This would add an additional loss term to equation (2.3). Moreover, the size change due to coagulation in the course of the experiment should be small so that K_{jj} can be related to the initial particle size.

With an idea of the experiments needed to determine coagulation rate coefficients, another look at the theory is needed to determine the size dependence of the coagulation coefficients. Following the derivation in Seinfeld we first consider the case of a population of equal sized particles of radius R_p and at a concentration of N_0. One particle is assumed to be fixed in position at the origin of the coordinate system. The other particles are assumed to be distributed around this central particle by continuum diffusion. So the equation that the distribution follows is

$$\frac{\partial N}{\partial t} = \mathcal{D}\left(\frac{\partial^2 N}{\partial r^2} + \frac{2}{r}\frac{\partial N}{\partial r}\right), \tag{2.5}$$

where $\mathcal{D}$ is the diffusivity of the particle in the surrounding gas. With the boundary

conditions

$$N(r,0) = N_0 \tag{2.6}$$

$$N(r,t) = N_0 \;\; as \; r \to \infty \tag{2.7}$$

$$N(2R_p) = 0. \tag{2.8}$$

The solution to this, assuming that particles stick together on collision is;

$$N(r,t) = N_0 \left[1 - \frac{2R_p}{r} \text{ erfc}\left(\frac{r - 2R_p}{2\sqrt{\mathcal{D}t}}\right)\right]. \tag{2.9}$$

The spherical particles collide when their centers of mass come within $2R_p$. So the rate at which particle arrive at radius r = $2R_p$ is ;

$$J_1 = 16\pi R_p^2 \mathcal{D}\left(\frac{\partial N}{\partial r}\right)_{r=2R_p} = 8\pi R_p \mathcal{D} N_0 \left(1 + \frac{2R_p}{\sqrt{\pi \mathcal{D}t}}\right). \tag{2.10}$$

Now the assumption that the particles are of equal sizes is relaxed. The diffusion coefficient, $\mathcal{D}_{12}$ must show the contributions from both particles of different sizes. Using their mean square displacements it can be shown that

$$\mathcal{D}_{12} = \mathcal{D}_1 + \mathcal{D}_2. \tag{2.11}$$

Also the spherical particles now collide when their centres of mass are at a radius of, $r = R_{p1} + R_{p2}$. The new solution for the concentration of particles of radius R_{p2} is;

$$N_2(r,t) = N_{20}\left[1 - \frac{R_{p1} + R_{p2}}{r}\, erfc\left(\frac{r - (R_{p1} + R_{p2})}{2\sqrt{\mathcal{D}_{12}t}}\right)\right], \tag{2.12}$$

which can be seen comes directly from equation (2.9). So the rate at which particles of type 2 arrive at the surface is;

$$J_1 = 4\pi \left(R_{p1} + R_{p2}\right) \mathcal{D}_{12} N_{20} \left(1 + \frac{R_{p1} + R_{p2}}{\sqrt{\pi \mathcal{D}_{12} t}}\right). \tag{2.13}$$

The steady-state rate of collisions is;

$$J_1 = 4\pi \left(R_{p1} + R_{p2}\right) \mathcal{D}_{12} N_{20}. \tag{2.14}$$

This rate is for collisions with a single particle of type 1 at the centre of the coordinate system. Now, if there is a concentration N_{10} of these particles then the total rate of collisions becomes;

$$J = 4\pi \left(R_{p1} + R_{p2}\right) \mathcal{D}_{12} N_{10} N_{20}, \tag{2.15}$$

or,

$$J = K_{12} N_{10} N_{20} \ , \tag{2.16}$$

where K_{12} is the Brownian coagulation kernel function for particles of radius R_{p1} and R_{p2}. In this derivation we have assumed that the particles were in the continuum regime. There is a difference in the behaviour of particles depending on the diameter of the particle, d, compared to the mean free path of the surrounding gas, λ. The Knudsen number Kn,

$$Kn = \frac{2\lambda}{d_m} \ , \tag{2.17}$$

is used for this ratio, where d_m is the mobility diameter of the particle. At 298K and at atmospheric pressure, the mean free path of air is 65 nm. Particles greatly below this in size are in the free molecular regime and those above are said to be in the continuum regime. Between the two limits is the transition regime where the aerodynamics are more complicated.

When the mean free path of the diffusing aerosol particle is comparable to the radius of the absorbing particle, the boundary condition at the absorbing particle surface must be corrected to include the non continuum transport near the surface. The continuum diffusion equation for Brownian motion can only be applied over distances that are large compared to the mean free path of the particle. (See Figure (2.1)).

Following the Fuchs (1964) approach we look at a case of a condensing vapor of species A in a background gas of species B. In the continuum regime and at steady-state the total flow of A to a central particle is the Maxwell equation,

$$J_{Ac} = 4\pi R_p \mathcal{D}_{AB} \left(c_{A\infty} - c_{AS}\right), \tag{2.18}$$

where $c_{A\infty}$ is the concentration of A as $r \rightarrow \infty$ and c_{AS} is the concentration of A at the surface of the particle.

In the kinetic regime the flux of A is the number hitting a unit area in a unit time. This is called the effusion flux $\frac{1}{4}c_{A\infty}\bar{c}_A$, where $\bar{c}_A$ is the mean molecular speed of species A. The particle has a surface area of $4\pi R_r^2$ so the flux of A to the particle is:

$$J_{Ak} = \pi R_p^2 \bar{c}_A \left(c_{A\infty} - c_{AS}\right). \tag{2.19}$$

As an approximate solution to the transition transport problem, the boundary condition (2.8) is replaced by the flux matching condition;

$$4\pi R_p^2 \frac{1}{4}\bar{c}_A \left[c_A \left(R_p + \Delta\right)\right] = 4\pi \left(R_p + \Delta\right)^2 \mathcal{D}_{AB} \left(\frac{\partial c_A}{\partial r}\right)_{r=R_{p1}+\Delta}. \tag{2.20}$$

The left-hand side is the effusion flux of moles of A to the surface of the particle and the right-hand side is the continuum flow of A from the region where $r > R_p + \Delta$. Using this boundary condition the steady-state solution for the flux to the absorbing surface is;

$$J_1 = 4\pi \left(R_{p1} + R_{p2}\right) \left(\mathcal{D}_1 + \mathcal{D}_2\right) N_{20} \beta_F \ , \tag{2.21}$$

where β_F is the Fuchs correction factor for the transition regime. The distance Δ has to be chosen. It makes physical sense to make $\Delta = \lambda_{AB}$. Defining the Knudsen number as $Kn = \lambda_{AB}/R_p$ the Fuchs correction factor becomes,

$$\beta_F = \frac{1 + Kn}{1 + \left(\frac{4\mathcal{D}_{AB}}{\bar{c}_A \lambda_{AB}}\right) Kn \left(1 + Kn\right)}. \tag{2.22}$$

Fuchs interpolation formula provides a solution for the transition regime problem with our two particles. Dahneke (1983) has suggested another form of the correction factor which deviates from the Fuchs form by less than 4% .

$$\beta_D = \frac{1 + Kn_D}{1 + 2Kn_D \left(1 + Kn_D\right)} \ , \tag{2.23}$$

where Kn_D is a redefined Knudsen number. It is,

$$Kn_D = \frac{2\mathcal{D}_{12}}{\bar{c}_{12} R_p}. \tag{2.24}$$

The mean molecular speed of the two particles is $\bar{c}_{12} = \left(\bar{c}_1^2 + \bar{c}_2^2\right)$. with $\bar{c}_1$ and $\bar{c}_2$ being

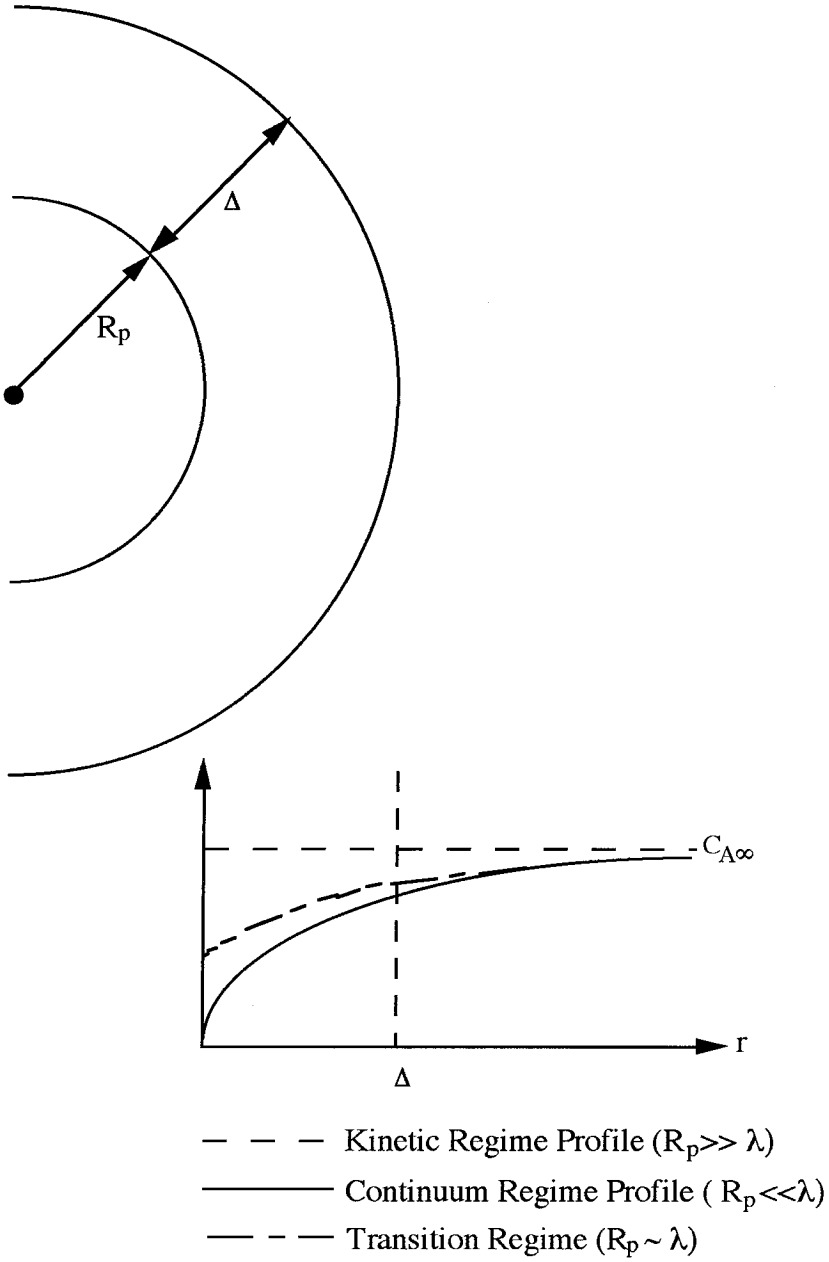

Figure 2.1: Steady-state concentration profiles around a spherical particle in different regimes. From Flagan and Seinfeld (1988) .

obtained from kinetic theory. So for a concentration of particles N_1 of type 1 the rate of collisions at the absorbing surface is;

$$J = K_{12} N_1 N_2 \ , \tag{2.25}$$

where K_{12} is the transition regime coagulation kernel for hard spheres. It is,

$$K_{12} = 4\pi \left(R_{p1} + R_{p2}\right) \left(\mathcal{D}_1 + \mathcal{D}_2\right) \beta_D. \tag{2.26}$$

For spherical particles with specific gravity of one in air at 25°C and at atmospheric pressure the coagulation coefficient for particles of the same size is a maximum for particles 50nm in diameter.

With a theory already available to describe the coagulation of spheres, the natural progression is to use a similar approach for the Brownian coagulation of agglomerates. The best way to do this is to look at each term in equation (2.26) in turn, starting with $R_{p1} + R_{p2}$. The absorbing surface for two agglomerates can be defined as the sum of two collision equivalent diameters d_{c1} and d_{c2}, following the hard sphere model.

The diffusivity of the agglomerates can be obtained from the Stokes-Einstein relation;

$$\mathcal{D}_1 = \frac{kTC_c\left(Kn\right)}{3\pi\mu D_1} \ , \tag{2.27}$$

where D_1 is the diameter of the agglomerate, μ is the gas viscosity, T is the absolute temperature, and $C_c\left(Kn\right)$ is the Cunningham slip correction factor. The slip correction factor has been found experimentally to be (Seinfeld, 1986)

$$C_c\left(Kn\right) = 1 + Kn\left(1.257 + 0.4\exp\left(\frac{-1.1}{Kn}\right)\right). \tag{2.28}$$

The transition regime β_D can be used but it is helpful to define the Knudsen number characteristic of coagulation as (Dahneke, 1983)

$$Kn_D = \frac{2\ \lambda_{12}}{d_{c1} + d_{c2}} \ , \tag{2.29}$$

where;

$$\lambda_{12} = \frac{2\left(\mathcal{D}_1 + \mathcal{D}_2\right)}{\sqrt{\left(\frac{12kT}{\pi^2\rho}\right)\left(d_{v1}^{-3} + d_{v2}^{-3}\right)}}. \tag{2.30}$$

The particles' volume equivalent diameters, d_{v1} and d_{v2} are used in equation (2.30). For a spherical particle the mass is;

$$m_1 = \frac{\pi}{6}\rho d_{v1}^3. \tag{2.31}$$

So it can be seen that K_{12} for agglomerates depends on d_v, d_c and d_m. For spherical particles these three diameters are identical but it is uncertain whether they are identical for agglomerates. Rogak and Flagan (1990) developed a theoretical approach to relate the agglomerate's mobility diameter to the primary particle diameter, and the particles fractal dimension, D_f. The experimental results in this paper will be compared to Rogak and Flagan's theory.

With characteristic dimensions defined for the agglomerates and hence being able to define a coagulation coefficient, equation (2.4) can again be used. This has the advantage that once the experiment has been set up for spherical particles, all that has to be changed is the particle source and coagulation coefficients for agglomerates can be measured.

The theory for spherical particles predicts that the coagulation rate for particles of different sizes should be greater than for the coagulation of similar particles. A look at the Smoluchowski equation for the coagulation of two differently sized particles gives two equations;

$$\frac{dN_a}{dt} = -K_{aa}N_a^2 - K_{ab}N_aN_b, \tag{2.32}$$

$$\frac{dN_b}{dt} = -K_{bb}N_b^2 - K_{ab}N_aN_b. \tag{2.33}$$

This assumes there are no addition terms, so a collision of two particles of size a do not form a particle of size b. These coupled equations do not have an analytical solution but they are very easy to model numerically. There are three unknowns K_{aa}, K_{bb}, and K_{ab}. The coagulation rates for particles of the same size can be found experimentally as described above leaving just K_{ab}. So knowing the inlet and outlet concentrations to a reactor, the residence time and the other two coagulation coefficients, K_{ab} can be obtained. This procedure is independent of the sizes and structure of the particles to be

studied.

An examination of the theory of Brownian coagulation of hard spheres has led to an understanding of the experiments necessary to obtain the coagulation coefficients. Firstly, hard sphere particles of one size will be produced and self coagulation coefficients calculated. Then coagulation coefficients for particles of differing sizes will be obtained. This can then be compared to theory and the procedure verified. Then the particle source can be changed to produce agglomerates and exactly the same procedure carried out.

2.3 Coagulation Experiment Apparatus

Previous meaurements of coagulation rates have been inferred from changes in measured size distributions of polydisperse aerosols (Okuyama et al., 1984; Szymanski et al., 1989; Kerminen 1994). The present experiments were conducted using nearly monodisperse or bidisperse aerosols. As illustrated in figure (2.4), two TSI 3077 cylindrical DMAs were used to produce aerosols of narrow size distribution from a polydisperse source. Particle sources typically produce a range of sizes and the DMA allows a monodisperse aerosol to be taken out of this range. A DMA requires the particles to be charged. This was achieved by using a TSI 3077 neutralizer in which α particle emissions by radioactive decay of Kr^{85} gas, produces positive and negative gas ions that then attach to the aerosol particles. The distribution of charges on the particles rapidly approaches a steady state. A Fuchs (1964) distribution was assumed for the charge on the spherical particles. For the coagulation of particles of the same size, the DMAs were set to the same voltage, while to produce particles of different sizes all that was necessary was to change the voltage on one of the DMAs.

The particles exiting the DMA all have a positive charge. In order to eliminate Coulombic forces that would bias the measurements of the Brownian coagulation rate, the classified aerosols were passed through a second TSI 3077 neutralizer. The particles leaving the second neutralizer again have a distribution of charges, with most of the charges being neutral for the size range examined in this study. Fuchs (1964) predicts an increase in the coagulation rate of only 2% even when the mean charge level is one-half.

After being neutralized, the aerosol flow was split two ways. One stream was transported to a cylindrical DMA that was running a scanning program to obtain size distributions every minute (Wang and Flagan, 1990). This analyzer DMA monitored the inlet concentration to the reactor. After the aerosols had passed through the agglomeration reactor a size distribution was obtained by a second Caltech cylindrical DMA. This allowed comparison of the concentrations before and after the reactor and from equation (2.4) the coagulation coefficient was calculated.

The Caltech cylindrical DMAs were constructed and calibrated at Caltech, with a design that maximised the transmission efficiency of aerosol particles. The detailed calibration of this DMA and measurements of its transmission efficiency are detailed in the appendix. The DMA flowrates were measured using the laminar flow pressure drop elements and Dwyer series 607 differential pressure transmitters. The flow controllers were calibrated with a Gillian Corporation Gilibrator. The particles from the analyzer DMAs were counted by TSI 3760 Condensation Nucleus Counters (CNCs). An IBM PC was used to record the data from the CNCs and also controlled the power supplies for the voltage ramp in the Caltech cylindrical DMAs.

The reactor used in the experiments was a 3.5 meter long tube with an internal diameter of 47.5mm. The entrance and exit regions were tapered to ensure there was no backmixing and that laminar flow was achieved. This assures that coagulation in the agglomeration reactor was only from Brownian motion of the particles, and not from laminar shear or turbulence and that the residence time in the reactor is well characterized. The reactor can be heated by flowing heated water through the PVC pipe that surrounds the inner stainless steel reactor, shown in figure. For these experiments the reactor was kept at room temperature and heating water was not used. The reactor, which is 3.5m long and has an internal diameter of 47.5 mm and is shown in figure (2.2). This gives a total volume of 6.33 x10^{-3} m^3 The neutralizer has a volume of 1.74 x 10^{-4} m^3.

The endcaps that are used to ensure a smooth transition into and out of the reactor have a volume of 1.05 x 10^{-4} m^3 and can be seen in figure (2.3). They have an internal conical shape, with an inside angle of 15 degrees. The reactor was connected to the two DMAs and the neutralizer by a length of 0.84m of $\frac{1}{4}$ inch copper tubing with a volume of 8.40 x 10^{-6} m^3 This gives a total volume of 6.3067 x10^{-3} m^3. Experiments were

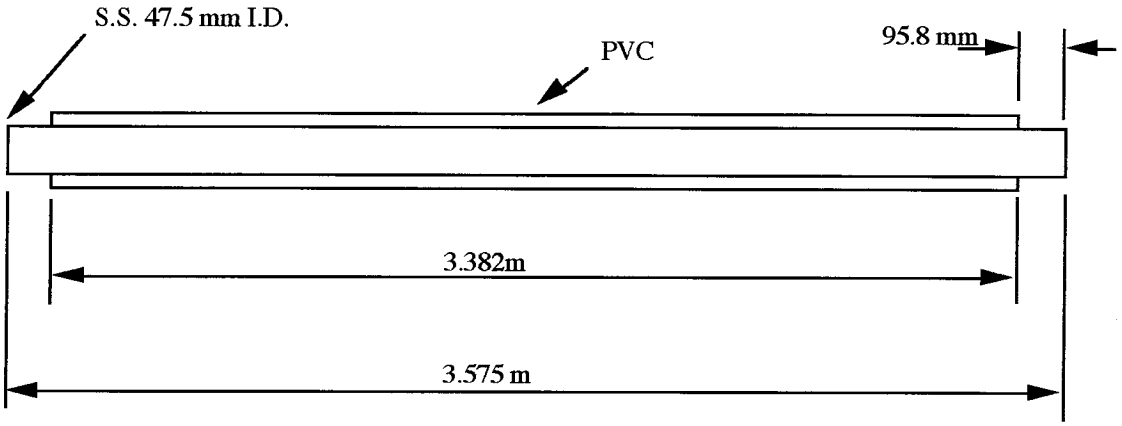

Figure 2.2: The agglomeration reactor showing the PVC waterjacket.

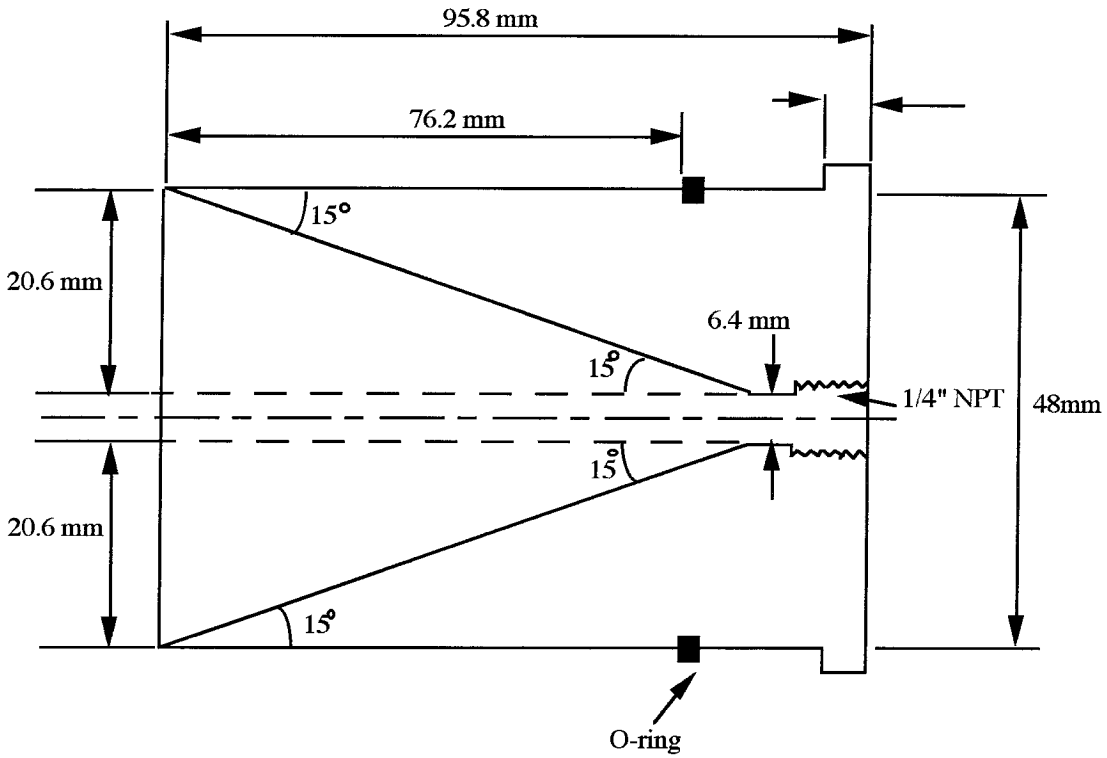

Figure 2.3: An endcap of the agglomeration reactor designed to ensure no backmixing occurred.

carried out to characterize the flow in the reactor. A step inpulse of particles was entered into the reactor and the transient outlet concentration was measured to determine the residence time distribution.

2.4 Reactor Characterization

The reactor for the coagulation experiments had to be of sufficently large volume to give the particles time to agglomerate while, at the same time , minimizing losses to the walls. The ideal reactor for the Brownian coagulation experiments would have a plug flow so that all the particles entering the reactor would have equal residence times. The long residence times required to make coagulation measurable leads to low Reynolds number operation (typically Re=30.4), making a fully developed laminar flow more attainable Laminar tube flow has a parabolic velocity distribution:

$$u = U[1 - \left(\frac{r}{R}\right)^2], \tag{2.34}$$

where U is the average velocity in the reactor. To measure the coagulation rate constants the time available for coagulation must be known. For laminar tube flow, different fluid elements have different residence times. The flow in the reactor can be described in terms of the residence time distribution $F(t)$ which is defined as the volume fraction of the input fluid that has remained in the system for a time less than t. The residence time distribution F(t) for a fully developed laminar pipe flow is (Hill 1977)

$$F(t) = 0 \quad t \leq \tau/2 F(t) = 1 - \left(\frac{\tau}{2t}\right)^2 \quad t \geq \tau/2 \tag{2.35}$$

where, $\tau = L/U$ is the average residence time. $F(t)$ varies from

$$F(t) = 0, \quad at \quad t = 0 \tag{2.36}$$

$$F(t) = 1, \quad at \quad t = \infty. \tag{2.37}$$

When a step change in the particle concentration is introduced into the reactor after steady-state flow has been established, no change will be seen until one-half of the

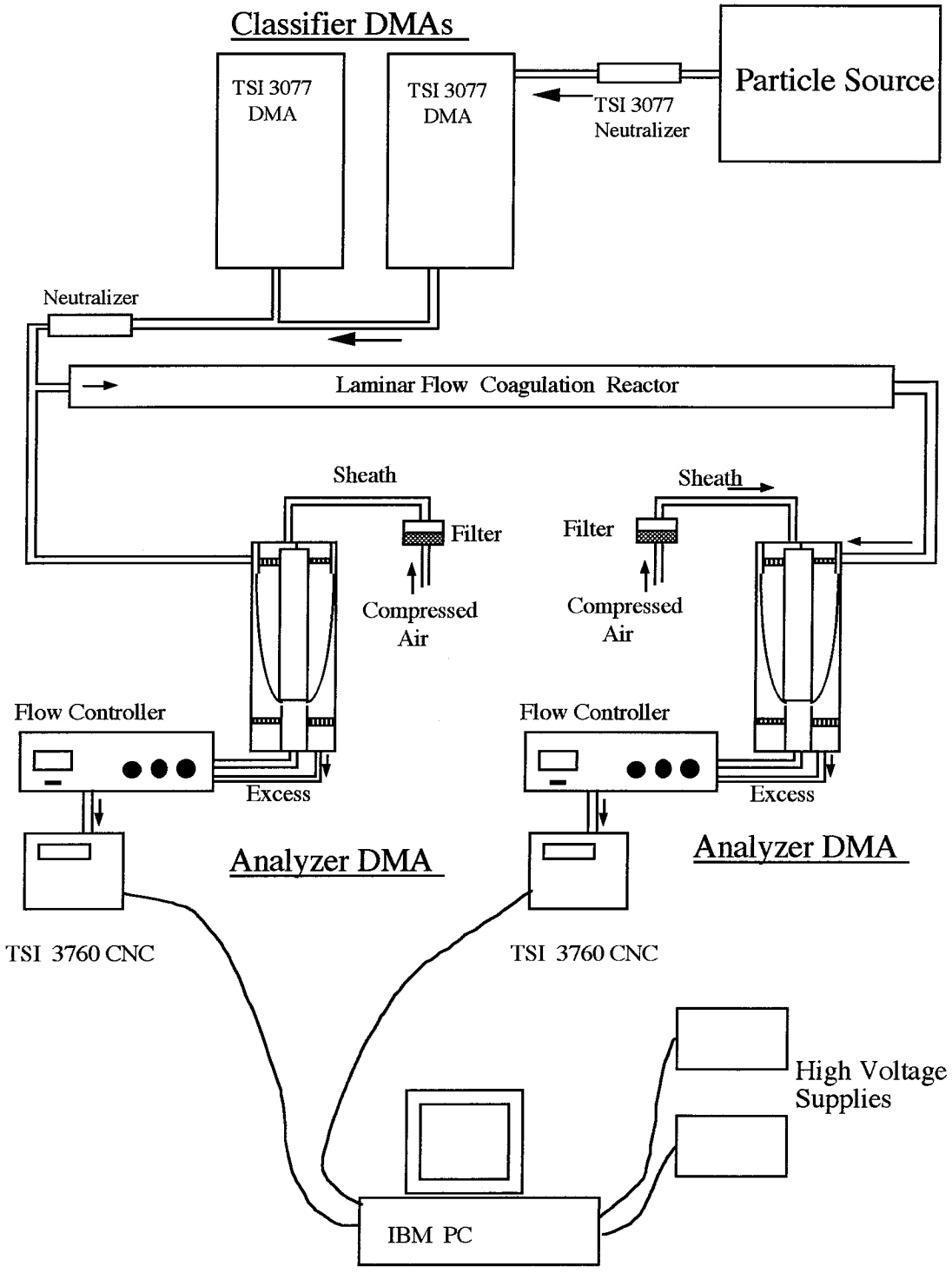

Figure 2.4: A flow diagram of the setup for the coagulation experiments.

average residence time has elapsed because the fluid flowing down the centerline at a velocity twice the average will just reach the exit of the reactor at this time. After this the outlet concentration will increase to the new value over time. If the step change used is from a known concentration to zero concentration, then F(t) can be represented simply as

$$F(t) = 1 - \frac{\text{outlet concentration}}{\text{initial steady-state concentration}}. \tag{2.38}$$

Comparison of the observed residence time distribution with that predicted for laminar pipe flow provides a check on the nature of the flow. A tandem differential mobility analyser (TDMA) system was used and is shown in Figure (2.5). One DMA was used as a classifier and the second analyzed the particles exiting the reactor (Rader and McMurry, 1986). The two DMAs used were TSI 3071s, with Caltech flow controllers used to monitor all the flows. The DMAs were operated at a 10:1 ratio of the sheath flow rate to that of the aerosol, with the sheath flow set to 10 l/min. A TSI 3077 neutralizer with a volume of 1.74 x 10^{-4} m^3 was placed after the classifier to give a distribution of charges on the particles. This was not needed for this determination but was required for the coagulation experiment. Including the neutralizer adds an additional reactor to the system but since it is much smaller in volume than the agglomeration reactor it's effect should be minimal. Particle concentrations out of the analyzer DMA were measured using a TSI 3010 condensation nuclei counter (CNC).

The source and analyzer DMAs were set to the same voltage and the system was run for 30 minutes to ensure that the reactor had reached steady-state. The voltage on the analyzing DMA was set to 320V and the voltage on the classifying DMA was changed from 320V to zero to give the step change. At the operating conditions of the source DMAs, 320V corresponds to an electrical mobility diameter of 40nm. Ideally the change in voltage should be instantaneous to ensure that no particles were introduced after the voltage was changed. This was not the case as the voltage supply inside the TSI DMAs required ten seconds to drop from 320V to 20V. Since the second DMA was also set at 320V particles going through the classifier DMA at 20V would not be transmitted. Data was obtained from the CNC using a QBASIC program and the CNC counts collected every second and stored on an IBM PC.

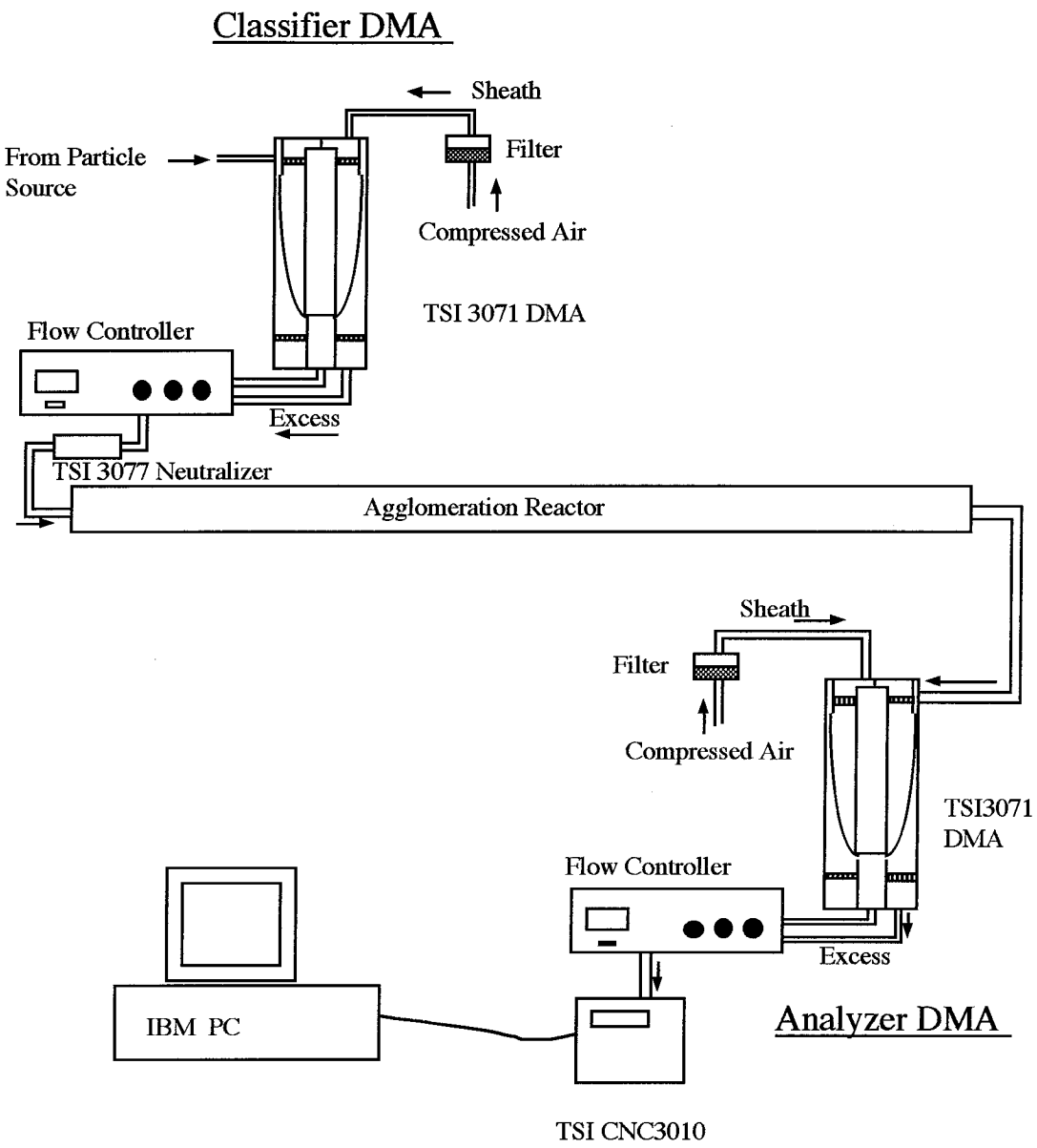

Figure 2.5: The flow diagram for the flow characterisation in the agglomeration reactor. The Tandem DMA setup is used with a $TiO_2.nH_2O$ particle source.

2.4.1 Flow Characterization Results

Figure (2.6) shows the residence time distribution that was inferred from the experiments. Two regions are apparent in F(t). The first region where F(t) = 0 corresponds to the early region before the pulse has reached the end of the reactor so the analyzer DMA does not yet see any change in the number concentration. There were small fluctuations in the steady-state particle concentration in this time from a small variation in the TTIP source temperature. After the pulse of clean air reached the end of the reactor, the particle concentration decreased from the steady-state value and F(t) increased. The reactor volume was 6.307 x 10^{-3} m^3 and the flow through the reactor was 1.028 litres per minute, which was the flow required by the 3010 CNC. Hence, the reactor's calculated residence time is 380s. The DMA and its flow controller have a residence time of 6 seconds. Particle diffusion in the reactor may broaden the response somewhat, but the effect is small. For a 40nm particle, the mean square displacement from diffusion after 360 seconds is

$$< x^2 >= 2Dt = 0.0152\text{cm}, \tag{2.39}$$

where D is the diffusivity, t is the flow time. Clearly the axial diffusion can be ignored as the effect is much smaller than the length of the reactor.

The residence time distribution calculated using equation (2.35) is compared to the experimental data in Figure (2.6). At long times the observed residence time distribution is higher than the theoretical one. Gravitational settling may contribute to the small differences between the two curves by redistributing the particles within the tube. Mixing in the neutralizer may also contribute. As expected from the Reynold number, the flow in the reactor is well defined as fully developed laminar flow. To obtain the residence time from the experimental data, E(t) = 1 - F(t), was plotted versus the inverse square of time, is shown in figure (2.7). E(t) reaches the limit of 1.0 at 190 seconds. This is half the residence time, so τ= 380 seconds. The slope of the figure (2.7) is $\tau^2/4$ and is the slope of the line of best fit corresponds to τ = 408 seconds. Given the slight non-linearity of the curve, the residence time will be taken from the intercept with E(t) = 1.0, corresponding to a time of 380 seconds.

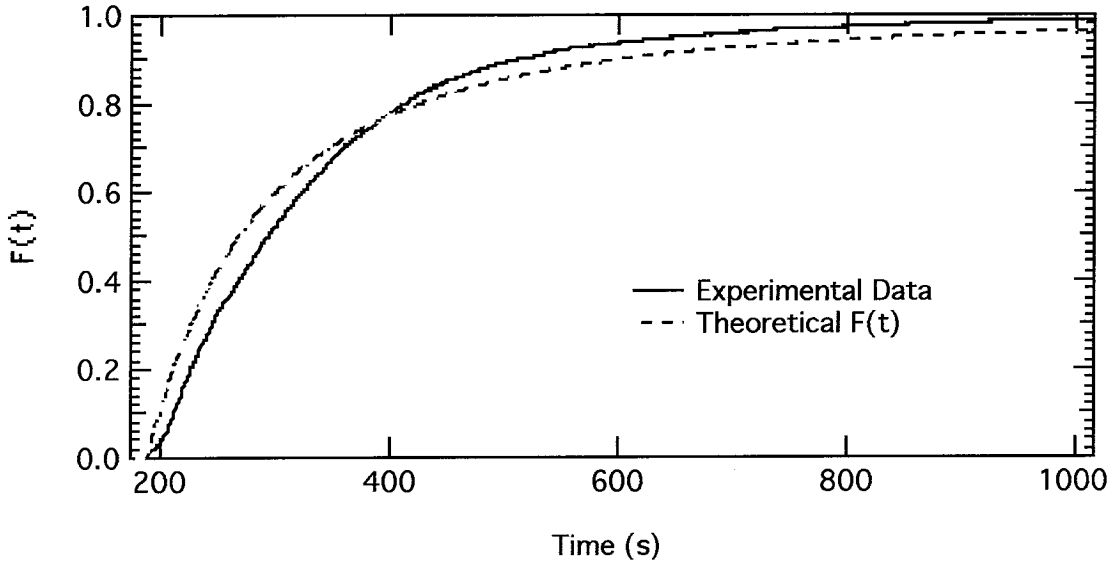

Figure 2.6: Flow characterization of the agglomeration reactor. Experimental data and theoretical values for a residence time of 380 seconds are shown.

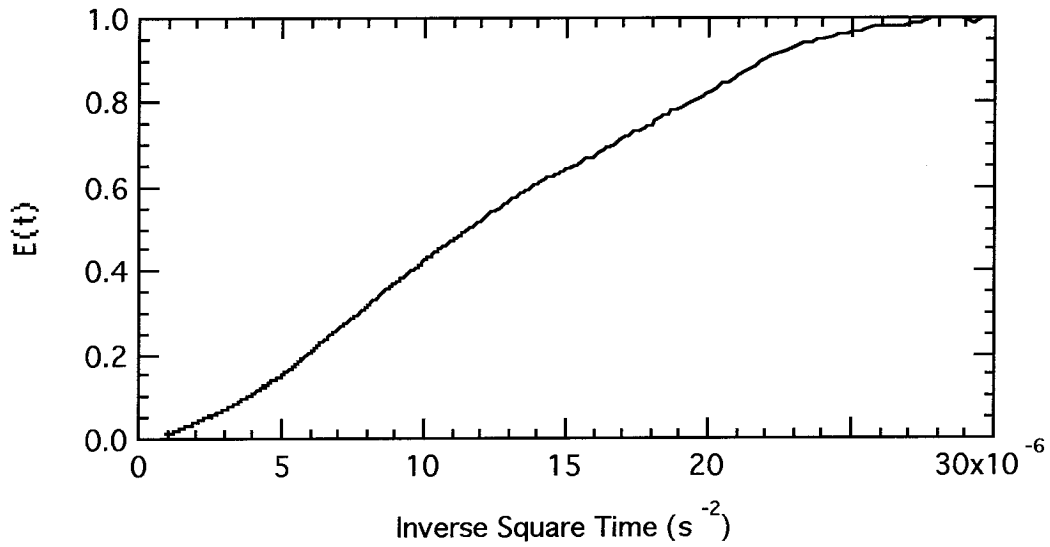

Figure 2.7: E(t) versus inverse square of time. Residence time can be derived from the slope and intercept of E(t) = 1.0

2.5 Dense Particle Coagulation

2.5.1 NaCl Aerosol Production

The first experiment performed was the coagulation of spherical particles to validate the procedure. Our choice for this was to study the coagulation of NaCl particles. There are many reasons for this choice. NaCl coagulation has been studied previously by Okuyama et al. (1984), and Fuchs theory is followed for particles above 50 nm in diameter. The other advantages are the cost, safety and ease of production of the NaCl particles.

From Smoluchowski's equation (2.3) the rate of coagulation is proportional to the square of the particle concentration. Hence, any particle source must produce large concentrations for coagulation rates to be significant. This is a particularly severe problem since the DMA only classifies a small fraction of the original aerosol. Also from equation (2.3) the coagulation coefficient is proportional to the difference between the inlet and outlet concentrations to the reactor, so any fluctuations in the inlet concentration leads to errors in the coefficient. The particle source should, therefore, be able to produce large concentrations very stably.

Our NaCl particle source was a constant output atomiser (Liu and Lee, 1975). High pressure air flows through a small aperture and results in a high velocity low pressure region on the other side of the aperture. The low pressure draws a NaCl and distilled water solution up from a reservoir. The NaCl solution is then atomised by the jet of air and the aerosol flows into a vertical chamber. Large droplets of solution fall back down to the reservoir while small drops are entrained in the airflow and carried through a heated tube. The heated aerosol then passed through a diffusion drier.

The NaCl particle source has another important feature. As the concentration of the NaCl solution is increased the particle source produces larger particles. This allows the source to produce mainly particles of the desired size. The atomiser produces a steady concentration of particles, provided the inlet flow of air is stable and the concentration of the solution to be atomised does not change. The solvent in a constant liquid fee atomizer evaporates during the course of the experiment, leading to an increase in the concentration of solute in the remaining solution. Liu and Lee (1975), report that the

change in the solution concentration with water, however, is not severe. To ensure that the concentration in the atomizer and hence particle size, was constant over the period of the coagulation experiments a 1.5 liter liquid reservoir was used. The constant liquid feed system eliminates the cyclical variations in particle concentration that are seen with commonly employed syringe pump systems.

The aerosol exiting the atomizer is wet and the particle size of this aerosol changes as it dries. The coagulation experiment relies on accurate measurement of the concentration of particles at known particle diameters. Therefore the aerosol stream was heated and passed through a diffusion drier to ensure the particles were dry. The peaks in the size distributions before and after the agglomeration reactor occur at similar diameters indicating that the aerosol was dry after the diffusion drier.

The shape of the NaCl aerosol particles are assumed to be spherical. The NaCl particles would be cubic crystals if the particles had dried completely. The particles were not imaged with Transmission Electron Microscopy, since the particles may absorb water after being collected on the TEM grid if the particles were anhydrous, or the low pressures in the TEM would cause the NaCl particles to dry. Either way, a representative picture of the NaCl particles may not be seen under TEM.

2.5.2 NaCl Coagulation Results

The NaCl source was attached to the coagulation setup and the two classifier DMAs were set to the same voltage to study coagulation of equally sized particles. After the system was allowed to reach steady-state, size distributions in the inlet and oulet flows of the reactor were measured for 20 minutes.

Figure (2.5.2) shows typical particle size distributions. The resulting size distributions showed not one, but several peaks. The extra peaks result from multiple charging effects in the DMAs. When a particle goes through the neutralizer there is a possibility that it will pick up more than one charge. As the size of the particle increases its ability to stabilize charge also increases. The DMA classifies according to electrical mobility.

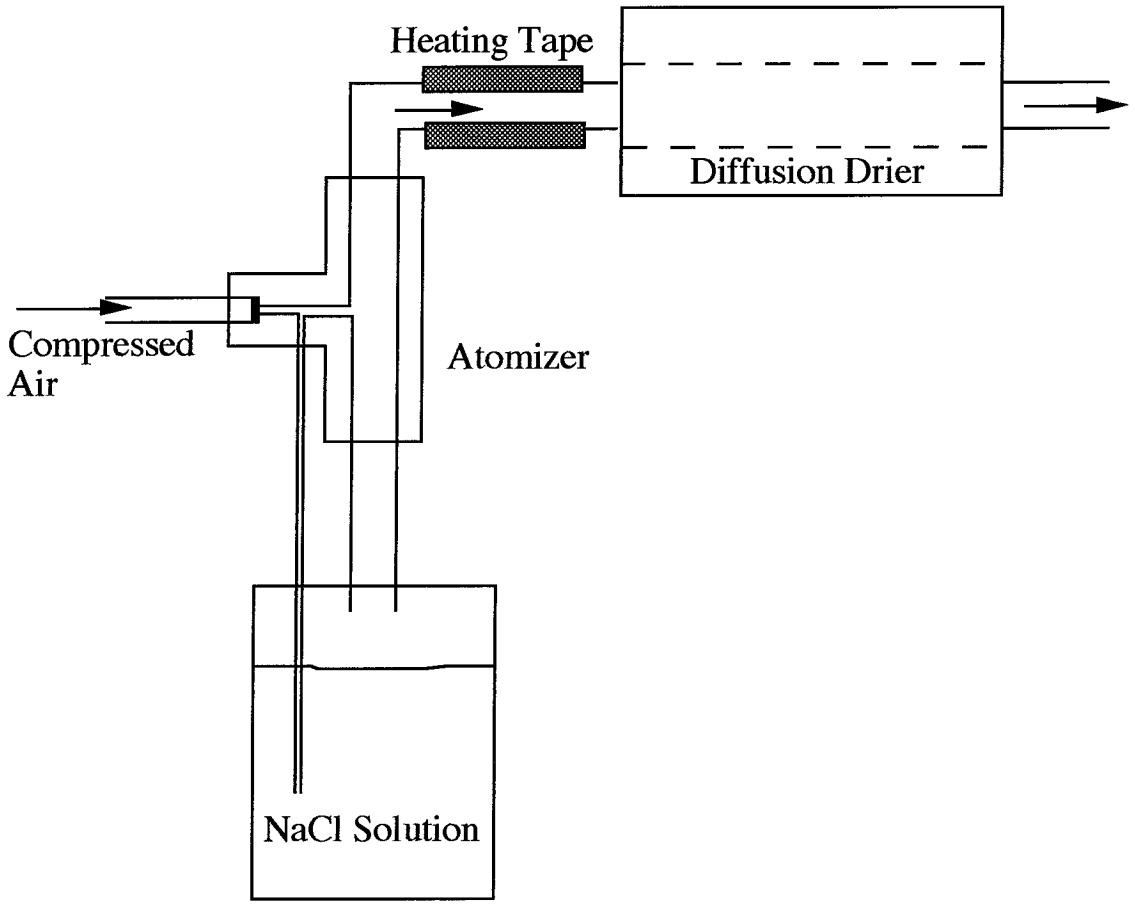

Figure 2.8: A flow diagram of the NaCl particle source.

The electrical mobility of a particle is;

$$Z_p = \frac{qeC_c}{3\pi\mu D_p}; \tag{2.40}$$

where q is the number of charges on the particle, Z_p is the particle mobility, C_c is the Cunningham correction factor, μ is the gas viscosity, and D_p is the particle diameter. The voltage is set on the DMA assuming +1 charge is carried by the particles. This gives the most probable mobility equivalent size of the classified particles, but other combinations of particle size and charge can give the same electrical mobility. When classified particles are passed through a neutralizer, they can acquire different charge levels and mobilities. This is clearly seen in TDMA measurements of size distributions of 100nm NaCl particles as shown in Figure (2.5.2). The peak at approximately 150nm results from particles that went through the first DMA with two charges and, therefore, had the same electrical mobility as 100nm particles with one charge. These 150nm particles then acquired one charge in the second neutralizer. Therefore the analyzer DMAs show the peak at 150nm. Some 150nm particles may continue to carry two charges when they pass through the second neutralizer. To separate their contribution out from the peak at 100nm, the charge distribution must be known. The distribution derived by Fuchs (1964) for the steady-state charge distribution was assumed to hold. There is another peak at 65nm. These are 100nm particles that left the second neutralizer with two charges. The analyzer DMAs classify them as smaller particles since they have twice the electrical mobility of singly charged particles.

The difference between the two distributions shown on the left side of Figure (2.5.2) is small. This is partly due to the logarithmic scale but also due to relatively low number concentrations. To count the particles accurately, the number concentrations into the counters must be below 100,000 cm^{-3}. The NaCl concentration at the 100nm peak was 30,000 cm^{-3}. With the theoretical coagulation coefficients for this size being 1.0 x 10^{-9} (cm^3/s), the number of collisions per second from the Smoluchowski equation (2.4) is 1.0. The reactor has a residence time of 360 seconds, so the theory indicates that, there should only be a small difference between the two distributions.

Similar experiments of the coagulation of equal sized particles were carried out over particle diameters from 20nm to 200nm. Multiple charging effects were taken into account as described in Chapter 3. Diffusional and gravitational settling losses were

calculated using the method of Chen and Yu (1993) which calculates each loss separately and then combines the two mechanisms to obtain an overall loss. Corrected particle size distributions were then used to estimate the coagulation rate coefficients.

Experiments to test the measurements for the coagulation rate for particles of differing sizes were also conducted. Salt particles of 20, 50, 100, and 150nm were each coagulated with 200nm salt particles. An experiment with 50nm and 100nm was also performed. The size distributions of the inlet and outlet aerosols of the latter experiment can be seen on the right side of Figure (2.5.2).

2.5.3 Comparison to Theory

The coagulation coefficients obtained from the previous experiments are shown in the following figures and compared to the hard sphere theory. The coagulation coefficients for particles of the same size were inferred from equation (2.4) with the number concentrations being the concentration under each peak after correction for losses and charging probabilities. The time for coagulation was taken to be the average residence time of 380 seconds. The comparison to the coagulation of spheres is shown in Figure (2.10). The uncertainties in the inlet and outlet concentrations were 2%. To minimise error the flowrates through the DMAs were carefully monitored but some drift in the inlet concentration is inevitable in the one hour required for each measurement of a coagulation coefficient.

The experimental and theoretical data agree well for particle radii smaller than 30nm. The spread of the data at larger sizes can be attributed to smaller concentrations from the NaCl source. As the inlet number concentration decreases then the ratio of particles lost from a size due to coagulation compared to losses from diffusion and gravitational settling becomes smaller. Therefore as the particle radius increases the experimental errors also increase.

The experimental values for the self coagulation of NaCl particles were then used to obtain values for the coagulation coefficients of unlike size coagulation. A numerical solution was used to obtain the solution to the coupled differential equations (2.32 and 2.33). These values have an experimental error in the number concentrations and also

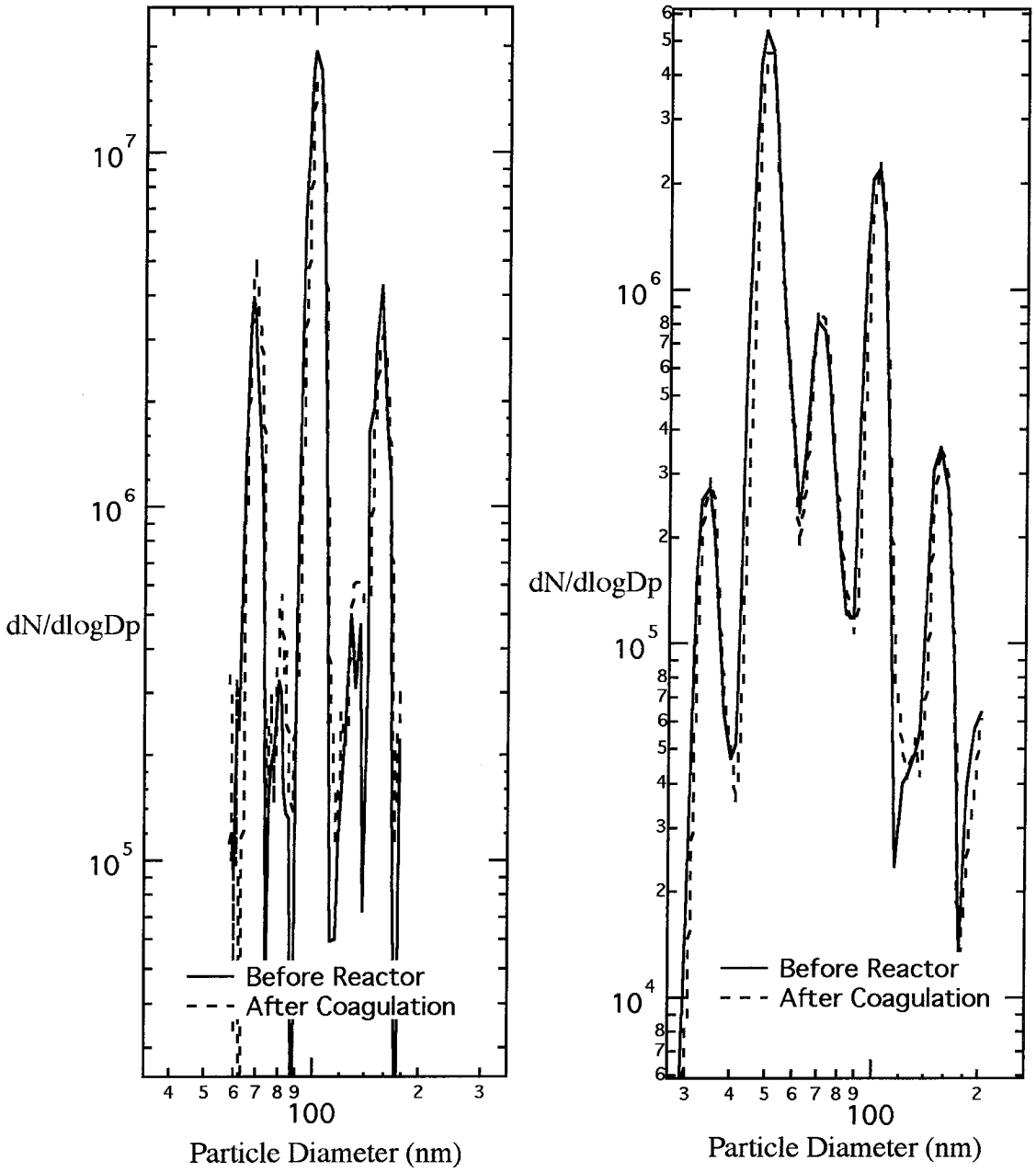

Figure 2.9: Left side of this figure shows the size distribution of 100nm NaCl particles before and after coagulation. The right side of this figure shows the size distribution of 50nm and 100nm NaCl particles before and after coagulation.

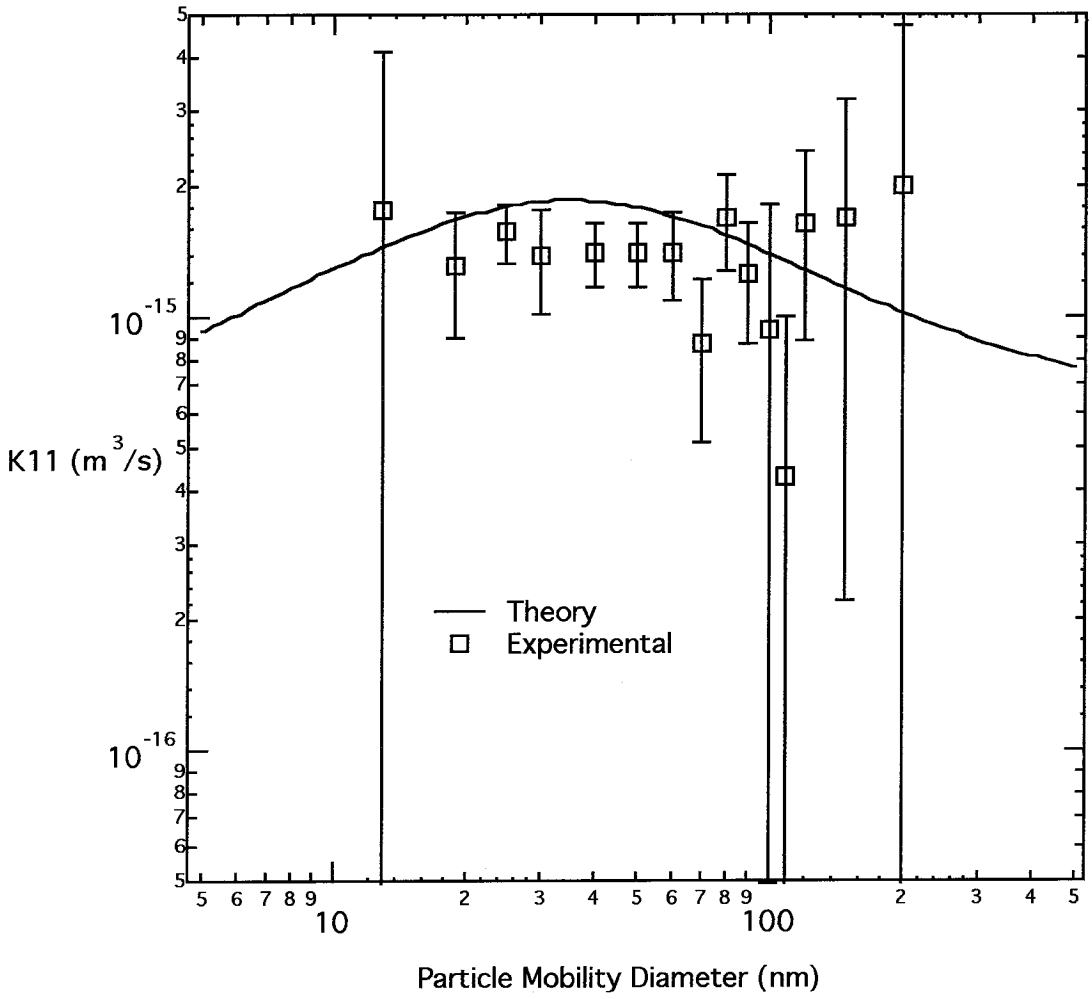

Figure 2.10: Comparison of experimental to theoretical coagulation coefficient for NaCl particles of the same size.

uncertainties from the self coagulation coefficients. The data follow the predicted trend as is shown in Figure (2.11). As the difference between the two particle sizes increases, then the coagulation coefficient rises above that for equal-sized particles.

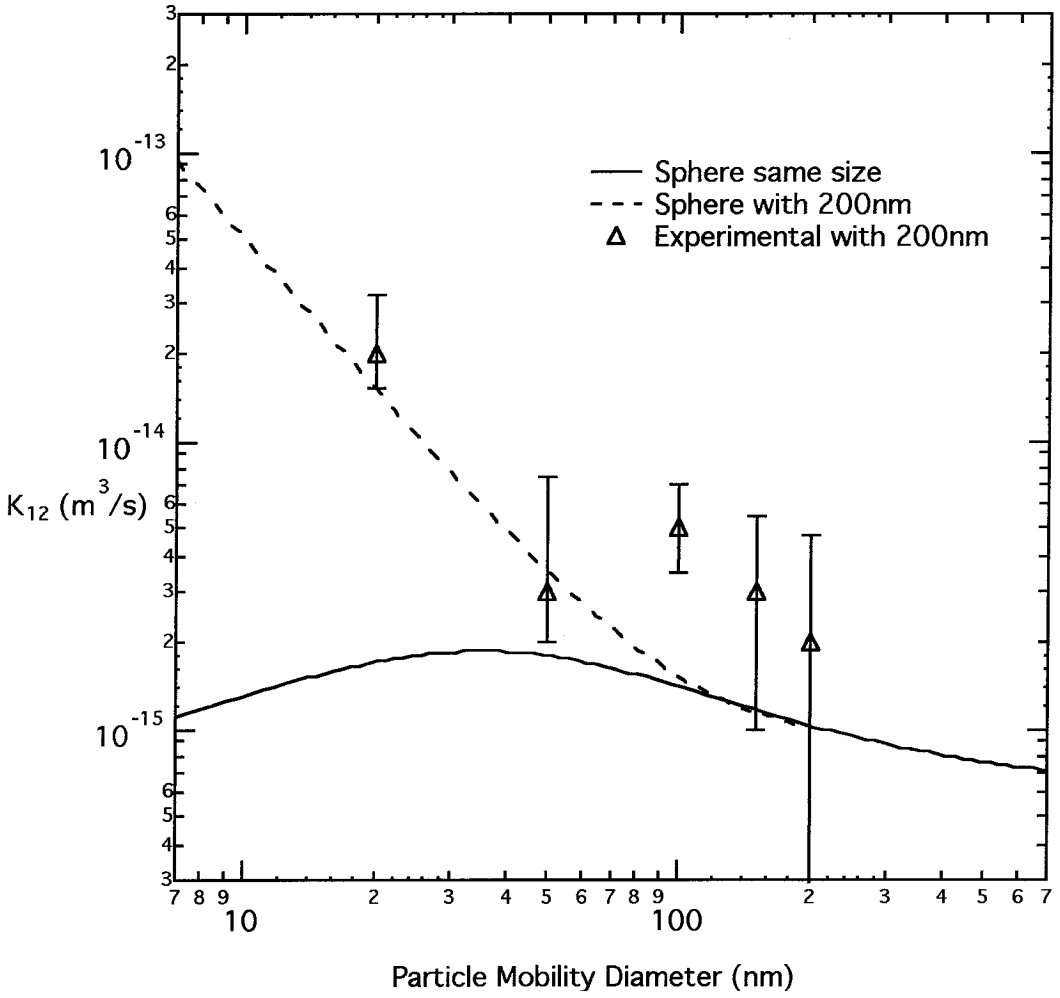

Figure 2.11: Comparison of experimental and theoretical results for coagulation of NaCl particles with a 100nm radius NaCl particle.

2.6 Agglomerate Aerosol Coagulation

2.6.1 Agglomerate Synthesis

With the NaCl particle experiments giving a basis to validate the procedure, the next step was to look at the Brownian coagulation of agglomerates. The choice of a particle source for agglomerates had the same criteria as for the sphere source. High concentrations, stable output, and an ability to shift the size distribution of the source to study a large range of sizes are required.

Our choice was to produce TiO_2 agglomerates by thermal hydrolysis of titanium tetraisopropoxide vapor (TTIP) shown in Figure (2.12). Seto et al. (1995) produced TiO_2 agglomerates with a fine structure from TTIP vapor. TiO_2 is produced in large quantities industrially as a pigment for paints and can be formed in high purity, although the usual method involves $TiCl^4$ oxidation. The use of the volatile TTIP precursor eliminates the corrosive byproducts while still producing solid particles from the gas phase at temperatures low enough to prevent sintering. TTIP is therefore, a convenient particle source. A nitrogen flow was passed over the liquid TTIP to pick up the TTIP vapor. This was carried out in a temperature controlled vaporizer to ensure the TTIP vapor flow was stable.

To retain the fine structure, the agglomerates need to be quickly formed at low temperatures and then discharged from the synthesis reactor to prevent sintering that would increase the fine structure scale of the agglomerate and the fractal dimension. To minimize sintering, the TTIP reactor was operated at 523K. At this low temperature, partially hydrated titanium oxide particles are produced, so the exact composition of the agglomerates is unknown, but the fine structure of the agglomerates is retained. TTIP undergoes a thermal decomposition described by,

$$TTIP \rightarrow TiO_2 + 4C_3H_6 + 2H_2O. \tag{2.41}$$

The pseudo-first-order rate constant for this reaction at 523K is 0.148 s^{-1} which is too slow to be viable for our system, where we require a burst of nucleation to form the small

primary particles. TTIP also reacts very readily with water,

$$TTIP + 2H_2O \rightarrow TiO_2 + 4C_3H_7OH. \tag{2.42}$$

The pseudo-first-order rate constant at 523K in the presence of a large excess of H_2, is 4.3 x$10^{14}s^{-1}$. This rapid reaction provides the necessary nucleation burst to form small primary particles. To provide the water vapor, clean compressed air was humidified in a bubbler at room temperature. This wet air was run into the reactor where it contacted the TTIP vapor carried in a nitrogen gas. The reactor was controlled to 250°C ±1°C.

2.6.2 Agglomerate Coagulation

As in the NaCl experiments, monomobility agglomerates were selected by the classifier DMAs and allowed to coagulate. Size distributions were measured at the inlet and outlet of the coagulation reactor. A typical size distribution is shown on the left side of Figure (2.6.2). Experiments were then performed in which agglomerates at two different mobilities were allowed to coagulate, yielding size distributions such as that shown on the right side of Figure (2.6.2). To gain an insight into the structure of the agglomerates, agglomerates of 50, 100 and 150nm mobility diameter were thermophoretically collected on holey carbon grids. Transmission Electron Microscopy (TEM) images were taken of the grids. Agglomerates of 50nm mobility diameter are shown in Figure (2.13), 100nm agglomerates are shown in Figure (2.14), and agglomerates of 150nm mobility diameter are shown in Figure (2.15).

The total concentrations under each peak were calculated. For agglomerates it was not clear what the distribution of charges would be on the agglomerates after they had passed through the bipolar charger. The Fuchs (1963) charging probability has been shown to provide the best agreement for spherical particles over the full range of particle sizes, whereas the Boltzmann distribution is a reasonable approximation forlarge particles but underpredicts the charging probability on spheres below about 20nm in diameter (Adachi et al., 1985). The $TiO_2.nH_2O$ agglomerates are made of many small primary particles, any of which could hold a charge. A tandem DMA experiment was used to measure the charge distribution on the $TiO_2.nH_2O$ agglomerates. The distribution of

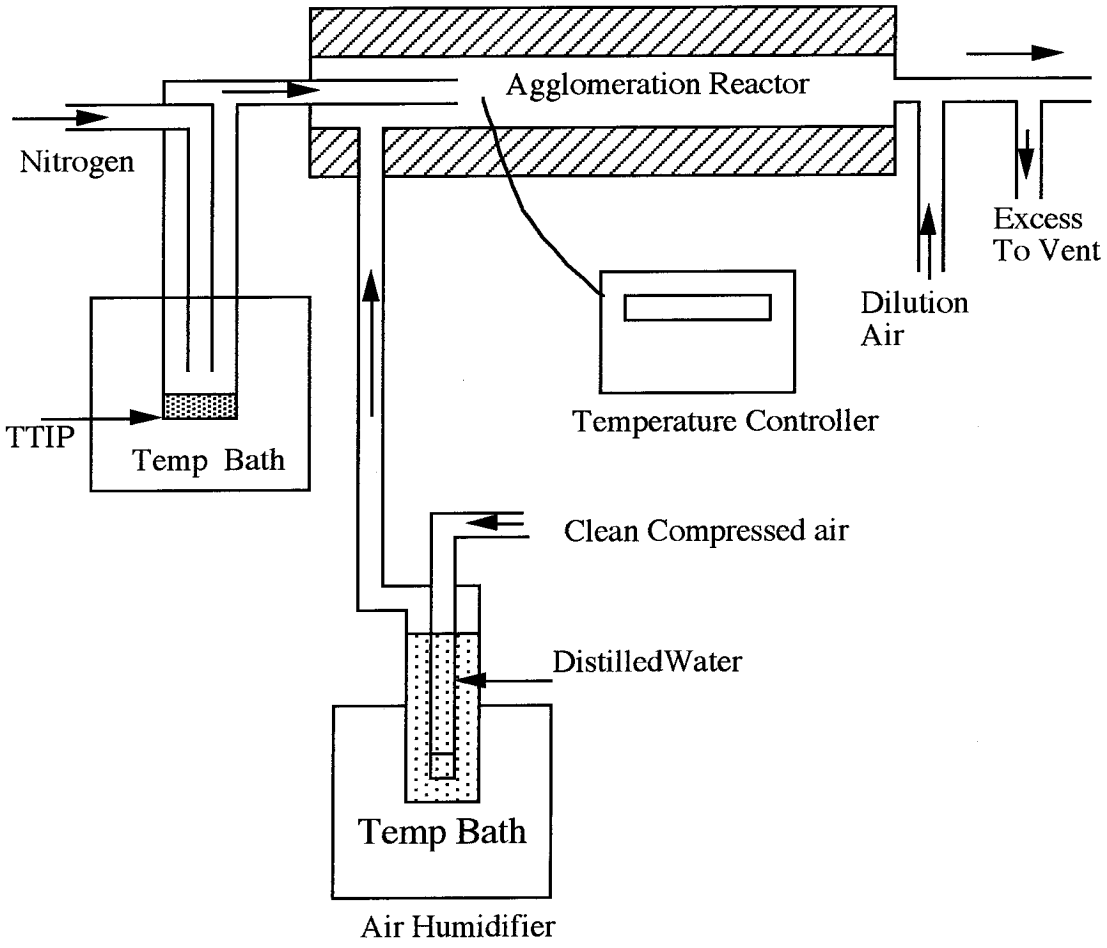

Figure 2.12: Flow diagram of the $TiO_2.nH_20$ agglomerate source.

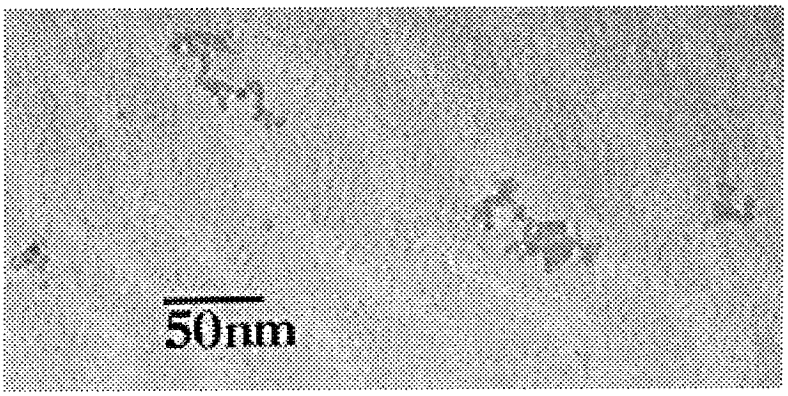

Figure 2.13: $TiO_2.nH_20$ agglomerates of 50nm mobility diameter.

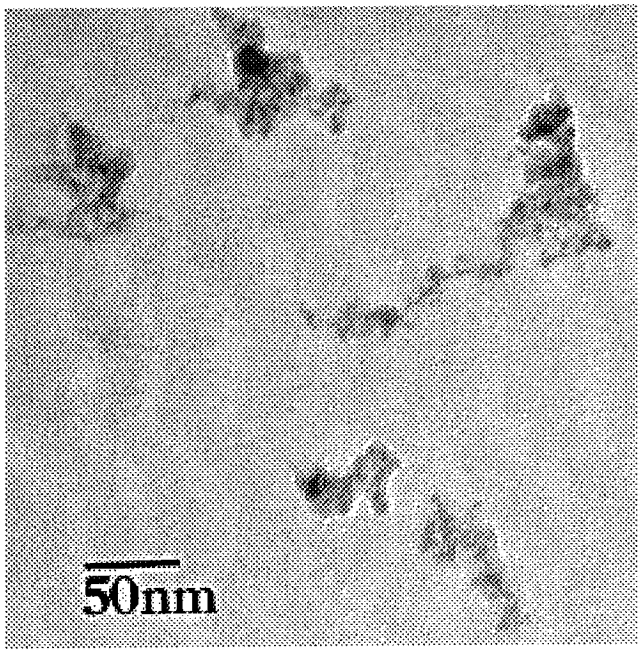

Figure 2.14: $TiO_2.nH_20$ agglomerates of 100nm mobility diameter.

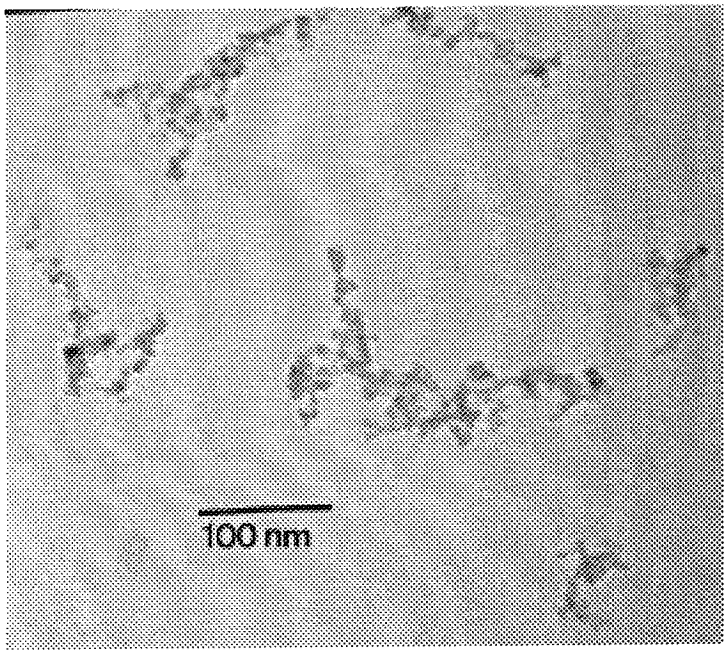

Figure 2.15: $TiO_2.nH_20$ agglomerates of 150nm mobility diameter.

charges on the agglomerate was found to be reasonably approximated by the Fuchs charge distribution on a sphere of equivalent mobility diameter. The experimentally obtained steady-state charge distribution was used in the inversion of the size distribution data.

The particle losses due to settling and diffusion also created a problem. The theory of Chen and Yu (1993) assumes that the settling velocity is known. For the agglomerate which has an irregular shape and unknown mass this is not able to be theoretically calculated. To determine the influence of particle losses on the coagulation rate measurements, particle losses due to diffusion and gravitational settling were measured directly using a single DMA. The DMA was used to classify a low concentration $TiO_2.nH_2O$ agglomerate aerosol which was then flowed into the agglomeration reactor at the same flowrate as used in the coagulation studies. The low number concentration into the reactor ensured that the difference in number concentration down the reactor was solely due to deposition by settling and diffusion to the walls, not to coagulation. The experiment was repeated for a range of mobility sizes. The experimental data corresponded well to the theoretical predictions based on the theory of Chen and Yu (1993), for a spherical particle of the same mobility diameter with a specific gravity of 1.0. With these two factors determined, the data could then be used to obtain the self coagulation coefficients.

2.6.3 Comparison to Theory

In this case the experimental values are compared to the theory of Rogak and Flagan (1992), assuming a fractal dimension of 1.8 which is typical for agglomerates formed by cluster-cluster aggregation. Figure (2.18) shows three theoretical curves each with a different primary particle radius. The two theoretical curves for primary particles of 10nm and 100nm show a maximum value at 30nm. Our experimental data, however, does not show a peak. For agglomerates of mobility radius below 20nm, the experimental points are markedly above the theoretical values. The difference may be due to van der Waals and image force enhancement of the coagulation. This enhancement has previously been reported for ultrafine spherical particles (Huang et al.,1990; Kerminen,1994).

To check the structure of our agglomerates transmission electron microscopy was used, and the primary particle radius was found to be 6nm. The particles also show

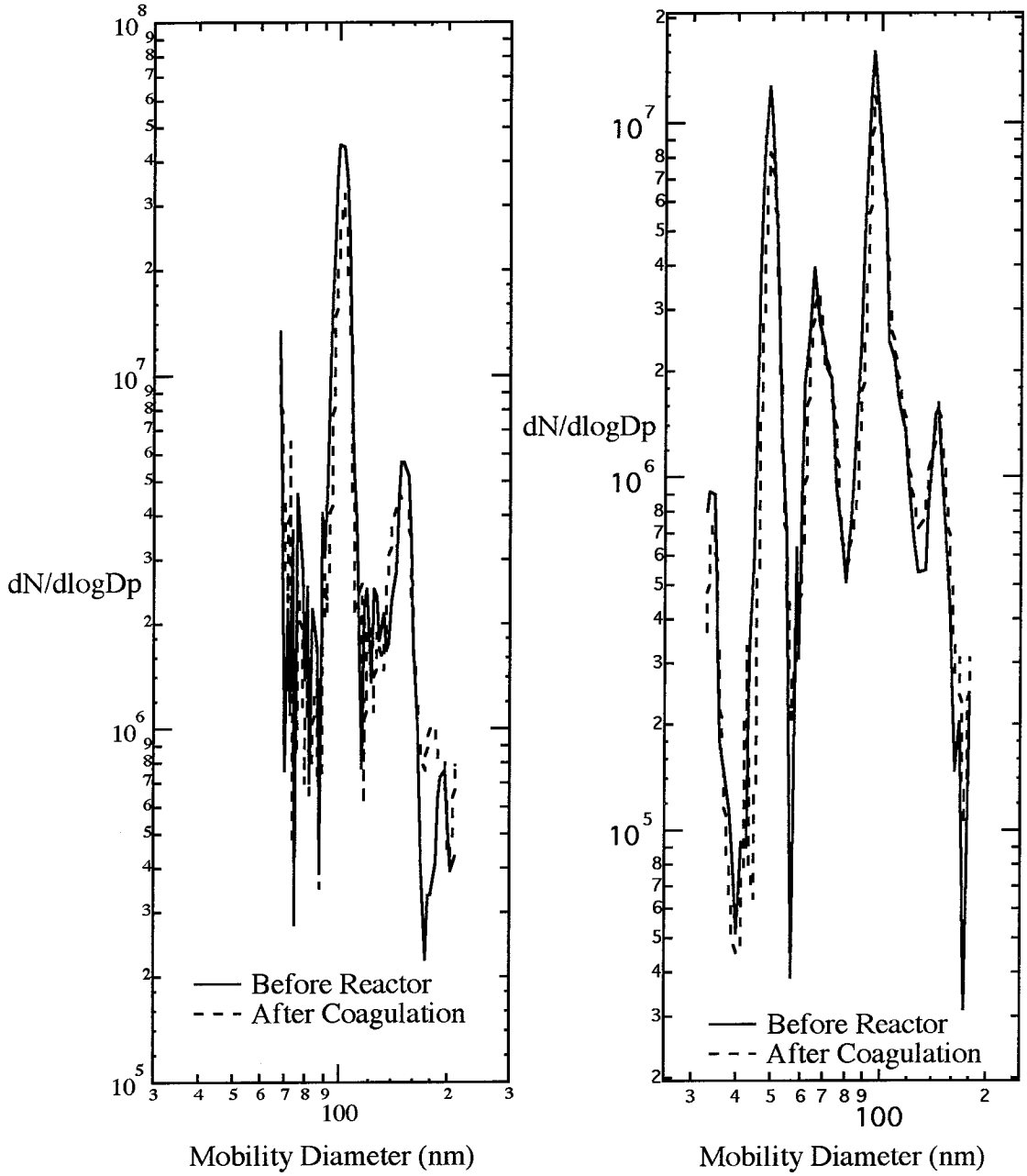

Figure 2.16: Left side of this figure shows the size distribution of 100nm $TiO_2.nH_20$ agglomerates before and after coagulation. The right side of this figure shows the size distribution of 50nm and 100nm $TiO_2.nH_20$ agglomerates before and after coagulation.

a loose structure which agrees with the choice of a low fractal dimension of 1.8 in the theoretical model.

Similar to the NaCl source, the $TiO_2.nH_2O$ agglomerate source produced fewer particles at large size. This accounts for the spread of data as the agglomerate radius increases. The uncertainty in the number concentrations in the agglomerate coagulation experiment was $\pm$ 3%,due to variations in the DMA flowrates that arose mainly from pressure changes in the inhouse compressed air supply. Care was taken to ensure the agglomerate source was stable, but the source aerosol number concentration varied over the one hour running time required for each coagulation coefficient measurement. The error in the number concentrations is smaller for the NaCl source than the agglomerates source as the latter source required controlling a larger number of flows than did the NaCl particle source.

The coagulation rate coefficients for particles of differing size, in Figure (2.18), were obtained using the experimental self coagulation coefficients. The error was estimated by using the errors in the coagulation coefficients for similar sized agglomerates, K_{ii}. The results were then compared to the theory of Rogak and Flagan for particles of fractal dimension 1.8 and primary particle size of 1nm. The data has some scatter due to a combination of uncertainties but a trend is apparent. As the difference in size between the two agglomerates coagulating increases then the coagulation coefficient also increases. The coagulation rate of agglomerates of differing size is larger than the coagulation rate of similarly sized agglomerates as predicted by the theory.

2.7 Conclusions

Two cylindrical DMAs were constructed and calibrated to serve as analyzers for the inlet and exit aerosols from the coagulation reactor. Care was taken to ensure that all flows were accurate and stable to minimize errors.

Two TSI 3077 DMAs were used to produce nearly monodisperse particles as inputs to the coagulation reactor. This setup has the advantage of being easily able to change the size of the particles into the reactor. The size of the particles studied was in the

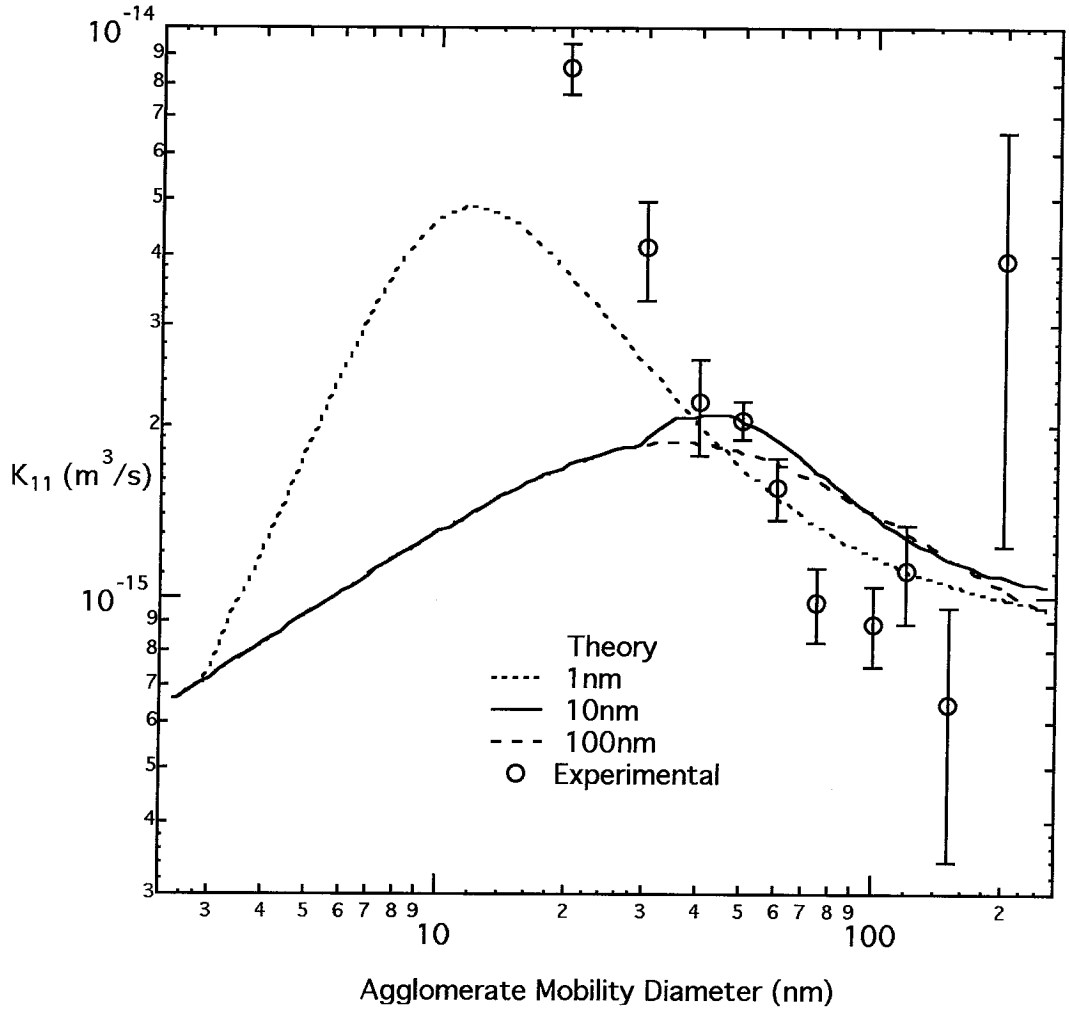

Figure 2.17: Comparison of experimental to theoretical results of the coagulation coefficients of $TiO_2.nH_20$ agglomerates of the same size.

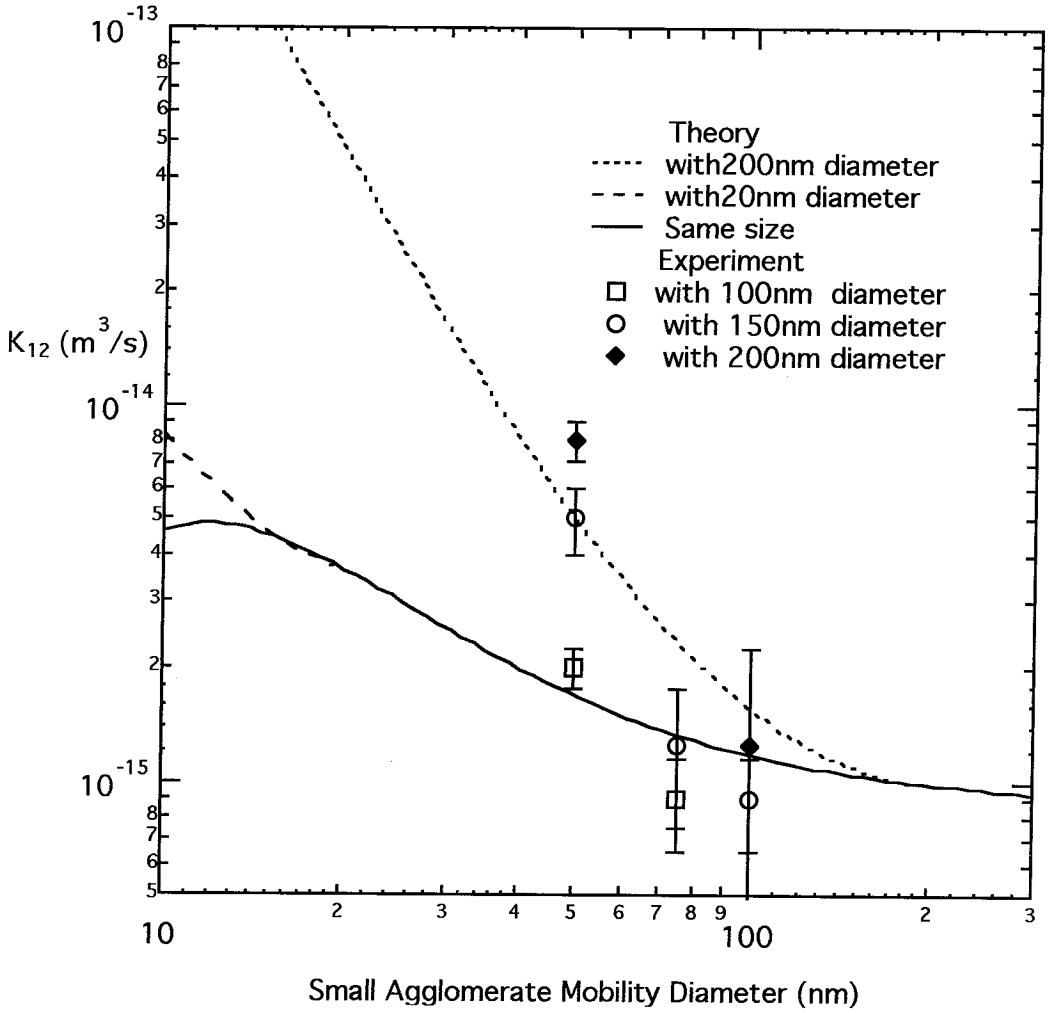

Figure 2.18: Comparison of experimental to theoretical results of the coagulation coefficients of $TiO_2.nH_20$ agglomerates of differing size.

transition regime, from 20nm to 200nm. Particle sources were constructed to provide high concentration and stable sources. An atomizer and dryer provided NaCl particles and TTIP hydrolysis gave a source of agglomerates with primary particle size of 6nm.

These two particle sources were then used as inputs to the coagulation setup and coagulation coefficients were obtained from analyzing size distributions. Multiple charging effects, transmission efficiency of the DMAs, and diffusion and gravitational losses were included in the analysis of the distributions.

The experimental data were compared to theory in both cases. The NaCl data was compared to the theory of Fuchs (1964). The monodisperse coagulation results followed the theoretical trend for the coagulation of spheres of the same size. The 2% uncertainty in the source concentration lead to large uncertainties in the coagulation coefficient for the NaCl particles below 20nm and above 100nm in mobility diameter. With the monodisperse coagulation coefficents known, further experiments were carried out to measure the coagulation rate of differently sized NaCl particles. The experimental results follow the Fuchs theory for spherical particles. The uncertainties in the coagulation coefficients arise from both source concentration drift and from the uncertainties in the monodisperse coagulation coefficients. The dense particle experiments provided good agreement with theory and verified that the coagulation setup was capable of meauring the coagulation coefficient.

The $TiO_2.nH_2O$ data was compared to a theory from Rogak and Flagan (1992) and showed similar trends to the theory. The monodisperse coagulation experiments were carried out first, as had been done for the NaCl particles. The monodisperse experimental data followed the trend shown by the theory of Rogak and Flagan for agglomerates with a fractal dimension of 1.8 and at 300K. The theory predicts that as the primary particle diameter decreases the coagulation coefficient reaches a maximum at smaller mobility diameters and that the maximum is larger as the primary particle diameter increases. The titania agglomerates had a primary particle diameter of 6nm and the coaguation coefficients should be between the theory for primary particles of 1nm and 10nm. Our data did not show a maximum but the two data points at 20nm and 30nm were larger than theoretically predicted. The difference was attributed to image and van der Waals force enhancement of the coagulation, and has been observed in the coagulation of spheres previously.

For the coagulation of differently sized particles, a numerical simulation of the reactor was used to obtain the coagulation coefficients, K_{ab}. Again the uncertainty was comprised of a combination of the source concentration drift and the error in the monodisperse coagulation coefficients. The experimental results showed that as the difference between the mobility diameter of the two agglomerates increased the coagulation rate increased. This trend was most evident for the coagulation of the 50nm agglomerates and larger agglomerates.

These experiments provided the first measurement of the coagulation of differently sized particles and agglomerates. The experimental data for NaCl particles agreed with the spherical theory. The coagulation of agglomerates below 40nm was found to be significantly larger than predicted by the theory of Rogak and Flagan.

2.8 Acknowledgements

The authors would like to thank Dr. Shou-hua Zhang for his considerable help and advice in the design and construction of the cylindrical DMAs and flow controllers. Funding support was recieved from the International Fine Particle Research Institute under grant FRR 20-07 and from the NSF under grant CTS-9113193.

Bibliography

Adachi, M., Kousaka, Y., and Okuyama, K. (1985). Unipolar and bipolar diffusion charging of ultrafine aerosol particles. *Journal of Aerosol Science*, 16(2):109–123.

Chen, Y. and Yu, C. (1993). Particle deposition from duct flows by combined mechanisms. *Aerosol Science and Technology*, 19(2):389–395.

Dahneke, B. (1983). *Simple Kinetic Theory of Brownian Diffusion in Vapors and Aerosols.* Academic Press, New York.

Flagan, R. and Lunden, M. (1995). Particle structure control in nanophase synthesis from the vapor phase. *Materials Science and Engineering A*, 204(1-2):113–124.

Flagan, R. and Seinfeld, J. H. (1988). *Fundamentals of Air Pollution Engineering.* Prentice Hall, New Jersey 07632.

Forrest, S. and Witten Jr., T. (1979). Long-range correlations in smoke-particle aggregates. *Journal of Physics A: Mathematical and General*, 12(5):L109–L117.

Fuchs, N. (1964). *The Mechanics of Aerosols.* Pergamon Press, New York.

Gutsch, A., Pratsinis, S., and Loffler, F. (1995). Agglomerate structure and growth rate by trajectory calculations of monomer-cluster collisions. *Journal of Aerosol Science*, 26(2):187–199.

Hill, C. (1977). *An Introduction to Chemical Engineering Kinetics and Reactor Design.* John Wiley and Sons, New York.

Huang, D., Seinfeld, J., and Okuyama, K. (1991). Image potential between a charged particle and an uncharged particle in aerosol coagulation - Enhancement in all size regimes and interplay with van der Waals forces. *Journal of Colloid and Interface Science*, 141(1):191–198.

Kerminen, V. (1994). Simulation of Brownian coagulation in the presence of van der Waals forces and viscous interactions. *Aerosol Science and Technology*, 20:207–214.

Koch, W. and Friedlander, S. (1991). Particle growth by coalescence and agglomeration. *Particle and Particle Systems Characterization*, 8(1):86–89.

Kruis, F., Kusters, K., Pratsinis, S., and Scarlett, B. (1993). A simple model for the evolution of the charateristics of aggregate particles undergoing coagulation and sintering. *Aerosol Science and Technology*, 19(2):514–526.

Liu, B. and Lee, K. (1975). An aerosol generator of high stability. *American Industrial Hygiene Association Journal*, 36:861–865.

Majerowicz, A., Pfalzmann, E., Smidovich, K., Reischl, G., Szymanski, W., and Wagner, P. (1990). An experimental study of Brownian coagulation for particles of different size and composition. *Journal of Aerosol Science*, 21(S1):S39–S42.

Marlow, W. (1980). Lifshitz-van der Waals forces in aerosol particle collisions. I. introduction: Water droplets. *Journal of Chemical Physics*, 73(12):6288–6295.

Matsoukas, T. and Friedlander, S. (1991). Dynamics of aerosol agglomerate formation. *Journal of Colloid and Interface Science*, 146(2):495–506.

Meakin, P. (1990). Fractal structures. *Prog. Solid St. Chem.*, 20(1):135–233.

Mountain, R., Mulholland, G., and Baum, H. (1986). Simulation of aerosol agglomeration in the free molecular and collision regimes. *Journal of Colloid and Interface Science*, 114(1):67–81.

Okuyama, K., Kousaka, Y., and Hayashi, K. (1984). Change in size distribution of ultrafine aerosol particles undergoing Brownian coagulation. *Journal of Colloid and Interface Science*, 101(1):98–109.

Okuyama, K., Kousaka, Y., and Hayashi, K. (1986). Brownian coagulation of two-component ultrafine aerosols. *Journal of Colloid and Interface Science*, 113(1):42–54.

Rader, D. and McMurry, P. (1986). Application of the tandem differential mobility analyzer to studies of droplet growth or evaporation. *Journal of Aerosol Science*, 17(5):771–787.

Rogak, S. and Flagan, R. (1992). Coagulation of aerosol agglomerates in the transition regime. *Journal of Colloid and Interface Science*, 151(1):203–223.

Rogak, S., Flagan, R., and Hung, V. (1993). The mobility and structure of aerosol agglomerates. *Aerosol Science and Technology*, 18:25–47.

Seinfeld, J. H. (1986). *Atmospheric Chemistry and Physics of Air Pollution.* John Wiley and Sons, New York.

Seto, T., Shimada, M., and Okuyama, K. (1995). Evaluation of sintering of nanometer-size titania using aerosol method. *Aerosol Science and Technology*, 23:183–200.

Smoluchowski, M. (1917). Verusch einer mathematischen theorie der koagulationkinetik kollider losungen. *Z. Phys. Chem.*, 92(1):129–168.

Szymanski, W., Majerowicz, A., and Wagner, P. (1989). Measurement of Brownian coagulation in monodispersed and bidispersed liquid aerosols. *Aerosol Science and Technology*, 11(1):1–10.

Vemury, S. and Pratsinis, S. (1994). Self-preserving size distributions of agglomerates. *Journal of Aerosol Science*, 26(2):175–185.

Wang, S. C. and Flagan, R. (1990). Scanning electrical mobility spectrometer. *Aerosol Science and Technology*, 13(2):230–240.

Wu, M. and Friedlander, S. (1993). Enhanced power law agglomerate growth in the free molecular regime. *Journal of Aerosol Science*, 24(3):273–282.

Chapter 3 Steady-State Charge Distribution on an Aerosol Agglomerate

The dust of exploded beliefs may make a fine sunset.

Geoffrey Madan
Livre sans nom:Twelve Reflections (1934) no.12

3.1 Abstract

The bipolar diffusion charging of an aerosol particle is an important step in electrical mobility particle sizing. The distribution of charges needs to be known exactly to enable precise determination of size distributions. For spherical particles, theoretical charging distributions are available. The Boltzmann distribution is accurate for particles over 30nm in diameter while the Fuch's charging theory has been shown to be accurate for particle diameters smaller than this (Hussin et al., 1983).

Less is known about the charging of aerosol agglomerates, which are fractal-like assemblies of large numbers of smaller primary particles. Interpretation of differential mobility analyzer measurements of soot and other aggregate aerosols requires an understanding of their charge distribution. To test the charging models, hydrous titanium oxide agglomerates were produced and the charging distribution measured from Tandem Differential Mobility Analyzer (TDMA) experiments. The percentages of agglomerates with one to four positive charges were measured. The resulting charge distributions agree best with the Fuchs charging theory but indicate that care needs to be taken in the inversion of electrical mobility size distributions.

3.2 Introduction

Aerosols can be charged in two ways, field or diffusion charging (Flagan and Seinfeld, 1988). Field charging results from local perturbations in the electric field in the vicinity of an aerosol particle. Gas ions migrate along electric flux lines that converge on the particle due to these perturbations, leading to charging. Diffusion charging results from the collisions of particles and ions due to their random thermal motions. Diffusion charging generally dominates the charging of particles below 1μm, and is used to charge particles in most differential mobility analyzer measurements.

The electrophoretic migration velocity, v_e, of a charged particle in an electric field

is determined by a balance between electrostatic and aerodynamic drag forces,

$$qE = \frac{v_e}{B} \tag{3.1}$$

where q is the charge on the particle, E is the external electric field, and B is the mechanical mobility which is a function of the particle size and shape. For spherical particles of diameter D_p,

$$B = \frac{3\pi\mu D_p}{C_c(Kn)} \tag{3.2}$$

where μ is the gas viscosity, and $C_c(Kn)$ is the slip correction factor, a function of the Knudsen number $Kn = 2\lambda/d_p$, accounting for non continuum effects that become important as D_p approaches or becomes smaller than the mean free path, λ. The electrical mobility

$$Z = qB = \frac{v_E}{E} \tag{3.3}$$

is proportional to the charge on the particles. In electrostatic precipitation, high charge levels, $q \gg e$, are required to acheive high collection efficiencies. In mobility measurements, optimal performance would be achieved if each particle carried only one charge since multiply charged particles lead to a distribution of mobilities for similar particles.

Diffusion charging of aerosol particles is usually accomplished by ions that are generated either by an electrical corona or by ionization of gas molecules by energetic particles produced when radioactive decay particles strike gas molecules to produce positive ions and free electrons. These ions rapidly react with other gas molecules to give a myriad of ion products. Takebe (1974) studied positive ion species and measured the ion mobilities in air. He found that there are five main ion species in dry air and four main species in air with a relative humidity of 40 to 60%. They were estimated to be $O_2^+(H_2O)$, $O_2^+(H_2O)_2$, $O_2^+(H_2O)_3$, $O_2^+(H_2O)_4$, $O_2^+(H_2O)_5$.

A radioactive decay product will generate free electrons as well as positive ions when the gas molecules are ionized. These free electrons have a much greater mobility than the positive ions and experiments have shown an enhanced charge level on aerosol particles when free electron charging is significant (Romay and Pui, 1992b). The free electrons also attach to high electronegativity gas molecules, such as O_2 leading to the O_2^- ion (Filippov and Burtscher 1994). Although the ion chemistry at low pressures is reasonably well understood, many questions remain in atmospheric pressure reactions.

If water vapor is present in the gas, charge transfer or clustering will occur, enlarging the ions and reducing their mobilities. (Davison and Gentry, 1985). In the atmosphere, the positive ions have an estimated mean molecular weight of 0.131 kg/mol and a mean mobility of 1.4 cm^2 V^{-1} s^{-1} while the negative ions have an estimated molecular weight of 0.100 kg/mol and a mean mobility of 1.9 cm^2 V^{-1} s^{-1} (Adachi et al., 1985; Wen et al., 1984a). These low mobilities suggest substantial clustering. The relatively high mobility of negative ions leads to a charge imbalance, with approximately 54being negatively charged (Adachi et al. 1985, Kousaka et al. 1983). Romay and Pui (1992a) report that the positive ion mobilities are higher when the suspending gas used is Helium. The positive ions are He_2^+ and have a mobility of 16 cm^2 V^{-1} s^{-1}.

The ions created by radioactive decay particles can collide with walls, combine with other ions, or attach to aerosol particles (Adachi et al., 1989). If both positive and negative ions are present then the charging is said to be bipolar. If only positive or the negative ions are present, the charging is unipolar (Gentry and Brock, 1967). In this study only bipolar diffusion charging will be addressed.

The collision of an ion with a particle can be treated similarly to aerosol coagulation or the mass transfer to a particle, with the addition of an electrostatic potential near the particle (Wen et al. 1983a, Flagan 1988). At equilibrium, the Boltzmann charge distribution is obtained, in which the number of spheres carrying i charges per unit volume is

$$N_i = N_o \exp\left(\frac{-\varepsilon_i}{kT}\right) \tag{3.4}$$

where N_o is the number of the neutral particles and ε_i is the the electrostatic energy contained in the Coulomb field of a sphere in a vacuum (Wen et al. 1983a). The charging probability is obtained by assuming that the separation between the energy levels of a particle with i charges and $i+1$ charges is small compared to kT. The ratio of particles with i units of charge to the number of particles with no charge is given by

$$\frac{N_v}{N_o} = \exp\left(\frac{-v^2e^2}{D_p kT}\right) \tag{3.5}$$

where e is the elementary unit of charge, D_p is the particle diameter and T is the absolute temperature. The Boltzmann charge distribution has however, been shown to be a reasonable approximation for particles larger than 20nm (Yeh and Cheng 1983), and

has been widely used. For instance, Keady et al. (1993) use the Boltzmann charging distribution in their size distribution inversion for a differential mobility particle sizer.

The outlet charge distribution from a diffusion charger may not be the Boltzmann limit depending on the product of the concentration of ions, N, and the residence time of the particles in the charger, t (Büscher et al. 1991, Liu and Pui 1974a). Liu and Pui found that in the free molecular limit the product Nt had to exceed 6 x 10^6 ions cm^{-3} s^{-3} to acheive the Boltzmann distribution. In the continuum limit the minimum Nt value is 1 x 10^6.

Charge attachment is nearly irreversible at low temperatures, so the distribution of charges on the aerosol particles is determined by the rates of ion attachment, which, in turn depend on the ion mobilities (Fuchs, 1963). The low rate of charge loss from a particle surface leads to deviations from the equilibrium charge distribution, but a steady-state charge distribution develops when there is a sufficient excess of gas ions. Following the derivation of Fuchs, diffusion of gaseous ions towards a spherical particle of radius a, when no external field is present is

$$\frac{\partial n}{\partial t} = D\frac{\partial^2 n}{\partial r^2} + \frac{2D}{r}\frac{\partial n}{\partial r} + B\frac{\partial}{\partial r}\left[r^2 n E(r)\right] \tag{3.6}$$

where r is the distance from the center of the particle, n is the concentration of the ion, D is the ion diffusivity, B is the ion mobility, and E is the electrostatic force acting on the ion. Fuchs assumes that the particle's mobility can be ignored as it is generally much smaller than the ion mobility. Each time an ion strikes a particle the electrostatic force that other ions experience changes, so equation (3.6) will be valid for only short times.

The steady-state flux of ions, $I_\pm$ towards the sphere across a spherical shell of radius r is (Wen et al. 1984a)

$$I_\pm = 4\pi r^2 \left(D_\pm \frac{\partial n}{\partial r} \mp E B_\pm n_\pm\right) = \text{constant}. \tag{3.7}$$

One boundary condition is that the concentration of ions at a large distance from the particle should be the bulk value or

$$n = n_o \quad \text{as} \quad r \rightarrow \infty. \tag{3.8}$$

With this condition the concentration of ions at a distance r from a particle with i charges, is

$$n(r) = \exp\left[-\frac{B}{D_\pm}\phi(r)\right]\left(n_o + \frac{I_\pm}{4\pi D_\pm}\int_\infty^r \frac{1}{r^2}\exp\left[\frac{B}{D_\pm}\phi(r)\right]d\phi\right) \tag{3.9}$$

where λ is the mean free path of the ion. The image force term is included in the potential, ϕ, defined as

$$\phi(r) = \int_r^\infty E(r)dr = \frac{ve^2}{4\pi\varepsilon_o r} - \frac{e^2a^3}{8\pi\varepsilon_o r^2\left(r^2-a^2\right)}, \tag{3.10}$$

where ε_o is the permittivity of vacuum, and ve is the charge on the particle. The particles of interest in mobility measurements are often comparable or smaller than the mean free path, so noncontinuum effects must be taken into account. Fuchs (1963) applied the so-called flux matching method to develop an approximate expression for the steady-state charge distribution in the transition regime. In this method, he matched the flux in an inner region of thickness δ where free molecular transport was assumed to be active to that in an outer region where a continuum transport model was applied. He defined the vacuum boundary layer thickness, δ, from geometrical considerations as

$$\frac{\delta}{a} = \frac{a^2}{\lambda^2}\left[\frac{\left(1+\frac{\lambda}{a}\right)^2}{5} - \frac{\left(1+\frac{\lambda^2}{a^2}\right)\left(1+\frac{\lambda}{a}\right)^3}{3} + \frac{2}{15}\left(1+\frac{\lambda^2}{a^2}\right)^{5/2}\right]. \tag{3.11}$$

The outer continuum flux, given by equation (3.7), must equal the effusion flux at the vaccum boundary layer surface, i.e.,

$$I(\delta) = 4\pi\delta^2 n(\delta)\frac{\overline{c}}{4} \tag{3.12}$$

where $\overline{c}$ is the mean thermal velocity of the ions and $n(\delta)$ is the concentration of the ion on the limiting sphere. Of the ions that enter the limiting sphere, a fraction α will hit the particle. In the absence of electrostatic interactions, the fraction would be

$$\alpha = \left(\frac{a}{\delta}\right)^2. \tag{3.13}$$

Coulombic forces, including the image force, will cause the path of the ion in the limiting

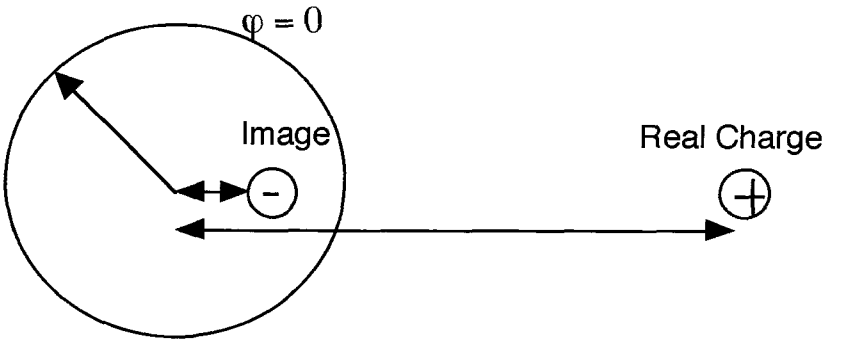

Figure 3.1: Location of an image charge for a real charge approaching a spherical particle.

sphere to curve and will change the value of α, higher for attraction and lower for repulsion. The image force is used to convert an electrostatic problem with fixed charges into a similar problem that is more easily solved and by the uniqueness theorem, has the same solution as the problem of interest. A charge approaching a neutral sphere, with $\phi = 0$ everywhere on the surface of the particle, is approximated by a charge approaching an opposite charge located at a distance x from the center of the particle, shown in figure (3.1). If the particle carries a charge, the surface of the particle will not be neutral but will have a potential of ϕ_o. To account for the surface potential, an additional image charge of $(4\pi\epsilon_o a\phi_o)$ has to be placed at the center of the sphere, this gives the surface of the sphere a potential of ϕ_o (Cheston 1964).

Fuchs (1963) solved the equations of motion for ions inside the limiting sphere to determine the ion flux,

$$I_{\pm}^{v} = \frac{4\pi a D_{\pm} n_{\pm}^{o}}{\int_{\delta}^{\infty} r^{-2} \exp\left[\phi(r)/kT\right] dr + (4D_{\pm}a/\overline{c_{\pm}}\alpha_{\pm}\delta_{\pm}^{2}) \exp\left[\phi(\delta)/kT\right]} \tag{3.14}$$

where (B/D) has been replaced by $(kT)^{-1}$ by applying the Einstein relation between mobility and diffusivity. Defining the combination coefficient for a particle carrying i charges

$$\beta_{ij} = \frac{I^{i}}{n_{\pm}}, \tag{3.15}$$

where $j = i \pm 1$ is the charge after charge attachment. A population balance on the

number of particles carrying p elementary charges can be written

$$\frac{dN_p}{dt} = n_+\beta_{p-1,p}N_{p-1} + n_-\beta_{p+1,p}N_{p+1} - n_+\beta_{p,p+1}N_p - n_-\beta_{p,p-1}N_p \tag{3.16}$$

where $n_\pm$ is the concentration of ions of appropriate polarity.

Fuchs (1963) examined charging in the special case of equal mobilities and concentrations of positive and negative ions. Hussin et al. (1983) and Adachi (1984) et al. extended the model to include different mobilities of positive and negative ions. At steady-state, $dN_p/dt = 0$ and the ratio of particles with successive charge levels can be expressed as

$$\frac{N_p}{N_{p\mp1}} = \frac{n_\pm}{n_\mp}\frac{\beta_{p\mp1,p}}{\beta_{p,p\mp1} + \frac{n_\pm}{n_\mp}\beta_{p,p\pm1} - \beta_{p\pm1,p}N_{p\pm1}/N_p} = A_p. \tag{3.17}$$

This recursive relationship can be used to find the number concentration of particles carrying p charges relative to the number of neutral particles

$$\frac{N_{\pm p}}{N_o} = \prod_{j=1}^{p}\left[A_{\pm j}\right]. \tag{3.18}$$

The total number of particles is

$$N_{TOT} = N_o + \sum_{p=1}^{\infty}\left(N_{+p} + N_{-p}\right). \tag{3.19}$$

Hence, the charge distribution is

$$\frac{N_{\pm p}}{N_{TOT}} = \frac{\prod_{j=1}^{p}\left(A_{\pm j}\right)}{1 + \sum_{j=1}^{\infty}\left(\prod_{k=1}^{p}\left(A_{\pm k}\right) + \prod_{k=1}^{p}\left(A_{\mp k}\right)\right)}. \tag{3.20}$$

The charge distribution can be evaluated beginning from sufficiently large p that $N_{\pm p\pm1}$ is negligbly small and determining succesive concentrations to $p = 0$ from both the positive and negative sides.

Romay and Pui (1992) measured the combination coefficient of ions with ultrafine silver particles in the 5-50nm range. They conclude that the Fuchs limiting sphere theory agrees well with the experimental results. Wiedensohler and Fissan (1991) measured

the steady-state charge distribution produced by bipolar charging of sodium chloride and silver particles in air, argon and nitrogen. The bipolar distributions in argon and nitrogen were more asymmetric than in air due to the increased free electron charging that takes place in electropositive gases. The charging was again found to be able to match the experimental curves with adjustment of the ion mobilities and ion molecular weights. The Fuchs model was found to be independent of the particle's material and of the purity of the gas.

An empirical approximation to the Fuchs charge distribution was developed by Wiedensohler (1987). Wiedensohler took into account the different ion mobilities and masses of the negative and positive ions, and used an α correction factor to take image forces into account. This solution allows the charge distribution to be calculated easily for particle sizes from 1 to 1000nm with a maximum error of 3% from the exact solution. The approximation formula to Fuchs model is

$$f(N) = 10^{\left(\sum_{i=0}^{5} a_i(N)\left(\log \frac{D_p}{nm}\right)^i\right)}, \tag{3.21}$$

where $f(N)$ is the percentage of particles carrying N charges, $a_i(N)$ are the approximation coefficients. All the Fuchs charging curves in the figures in this paper were generated from Wiedensohler's approximation.

Filippov (1994) examined why the Boltzmann charge distribution matches the charge distribution for some particles when the charge transfer to a particle is clearly not an equilibrium process. He showed that the steady-state diffusion flux approach can be written in a similar manner to the modified version of the Boltzmann charge distribution for large particles that are not too highly charged.

3.2.1 Diffusion Charging of Non-Spherical Particles

Diffusion charging of spherical particles has been extensively studied, both theoretically (Takahashi and Kudo 1973) and experimentally (Vijayakumar and Whitby, 1984; Romay and Pui, 1992). Models of the charging of non-spherical particles have been derived as extensions of the spherical model and flux matching method. LaFramboise and Chang

(1977) extended the Fuchs charging theory to particles of any shape in the continuum limit. In the transition regime they obtained approximate charging current solutions for at oblate and prolate shaped particles. Han and Gentry (1991a) developed a computational model for the diffusional charging of platelets. According to their model the charge distribution on flakes is the same as that on spheres with the same surface area. The charge distribution on spheres of equal volume as the flakes was, however, significantly narrower. Also as the diameter of the flake increased from 0.3μm to 10μm the percentage of flakes that carried multiple charges increased. In both cases the thickness of the flake was kept to 0.03μm.

Unipolar charging of 1000 μm long carbon fibers in an electrostatic precipitator was measured by Han et al. (1991b). Ions were generated using a corona discharge. Given the size of the fibers and the strength of the electric field, field charging would be expected to dominate charging. The collection efficiency for these fibers in an electrical precipitator increased from less than 4% with no applied electric field to 55% with an electric field of 2.5 kV/cm. The charging of asbestos fibres by contact and friction charging was studied by Vincent et al. (1981). In their experiments, the average charge on a 4μm long asbestos fiber with a diameter of 0.4μm had an average 60 charges. The charged asbestos fibers were found to enhance deposition by 40% in the lungs of rats, primarily due to image forces.

Wen et al. (1984a) derived an expression for a charging equivalent diameter for a prolate spheroid of minor axis diameter, d_1, and of aspect ratio, β,

$$D_{QE} = \frac{d_1 \beta}{\ln(2\beta)}. \tag{3.22}$$

For spheroids with aspect ratios between 10 and 100, the charging equivalent diameter was 0.25 times the length of the spheroid.

Many aerosol particles are aggregates containing many small primary particles, either in the form of chains or as more compact structures. Dua et al. (1980) used a parallel plate mobility spectrometer to measure the equilibrium charge distribution on doublets and triplets of 500nm diameter polystyrene spheres. They observed that more doublets and triplets carried multiple charges than was predicted using the Boltzmann distribution for volume equivalent spheres.

The next level of complexity in non-spherical particles is a linear chain of uniform particles. Cheng and Yeh (1981) developed a model based on the assumption that each primary particle in the chain acquired a charge according to Boltzmann's law. The resulting charge on the chain was the sum of individual charges. According to this model, the charge distribution on the chains was the same as the Boltzmann distribution on a sphere with a diameter equal to the product of the primary particle diameter and number of primary particles. Good agreement was reported with the small aggregate data of Dua et al.(1980). Yeh and Cheng (1983) later applied their model to straight chains with nonuniform primary particle size. Few experimental measurements of the charge distribution on chain agglomerates have been reported. Vomela and Whitby (1967) carried out experiments on chains of 10 to 300 primary particles of 50nm diameter. The charge carried by the chains after bipolar diffusion charging was found to be 70% higher than that of volume equivalent spheres.

Wen et al. (1984b) applied their charging equivalent diameter to linear chain aggregates. The chains used had mean primary particle diameters, $\overline{d_1}$, of 41 nm to 81 nm. The charging equivalent diameters of chains with n primary particles was estimated using the prolate spheroid model, to be

$$D_{QE} = \frac{\overline{d_1} n}{\ln(2n)}. \tag{3.23}$$

The experimentally observed charge on the chains was 20% to 30% greater than the Boltzmann distribution for spheres with the same charging equivalent diameters, i.e., the charging equivalent diameter was overestimated. Coagulation of the chains was thought to reduce the number of charges on the chains with large primary particle diameters.

Agglomerate particles generally are more complex than the linear chains treated by Wen et al. (1984b). They are often described as possessing fractal-like structures, wherein the number of primary particles scales with the radius of the gyrations as

$$N = K\left(\frac{r}{a}\right)^{D_f}, \tag{3.24}$$

where D_f is the mass-fractal dimension and K is an empirically derived constant of order unity. Agglomerate aerosol particles generally result from coagulation of fine particles produced by a burst of homogeneous nucleation. Agglomeration of an ensemble of par-

ticles is called cluster-cluster aggregation and results in ramified particles with a fractal dimension of about $D_f = 1.8$.

Han et al. (1990) applied the model of Cheng and Yeh (1981) to the charging of aerosol agglomerates, in which it is assumed that the primary particles acquire the Boltzmann equilibrium charge and then agglomerate with no subsequent charge exchange. Although Cheng and Yeh (1981) obtained good agreement with the observed charging of linear chains, the charge distribution predicted by their model was much broader than observed for agglomerate particles.

The charging of agglomerates was investigated experimentally by Rogak and Flagan (1992). The bipolar diffusion charge distribution was measured for PSL spheres, ammonium sulfate spheres and, TiO_2 agglomerates with an average primary particle diameter of 20 nm. Rogak and Flagan measured the charged and neutral fractions of the agglomerates and found that the fraction of neutral agglomerates was 5% lower than for spheres of comparable mobility. The difference was attributed to the agglomerate shape. The charge equivalent sphere for the agglomerates was best matched by 1.1 times the mobility diameter of the agglomerate. The neutral fraction was underpredicted by the Fuch's theory with the Boltzmann charging distribution being a much closer match.

None of the theories for bipolar diffusion charging of an aerosol agglomerates are fundamentally based. The charged fraction of agglomerate particles has been measured, but the distribution of charge levels has not been determined. Although, Fuchs flux-matching model accurately predicts the charging of spherical particles, even with diameters under 20nm, measurements of charge distributions on agglomerates. The present study seeks to fill this gap through tandem differential analyzer (TDMA) measurements of the distribution of positively charged aerosol agglomerates with nanometer-sized primary particles.

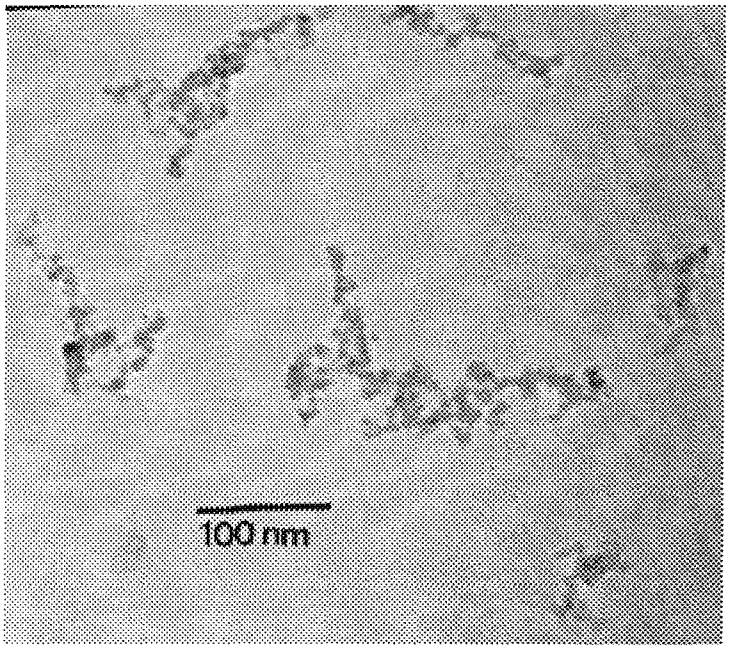

Figure 3.2: $TiO_2.nH_2O$ agglomerate particles with the same electrical mobility as a 150nm diameter sphere.

3.3 Experimental Procedure

3.3.1 Particle Generation

TiO_2 agglomerates were produced by thermal hydrolysis of titanium tetraisopropoxide vapor (TTIP). A nitrogen carrier gas partially saturated with vapor by flowing over a 50°C bath of TTIP as illustrated in Figure (3.4). The vapor-laden gas mixed with humid air in a 250°C agglomerate synthesis reactor where the TTIP and H_2O react to form $TiO_2.nH_2O$ particles and propanol. The $TiO_2.nH_2O$ particles are formed in such large concentrations that Brownian coagulation occurs rapidly forming agglomerates, but temperatures are low enough to prevent significant sintering of the primary particles. The resulting titania agglomerates, some of which are shown in Figures (3.2) and (3.3), have a fractal dimension of about 1.9. The average primary particle diameter is 6.5 nm ±3nm and is independent of the overall agglomerate size.

This system has previously been shown to produce agglomerates with small pri-

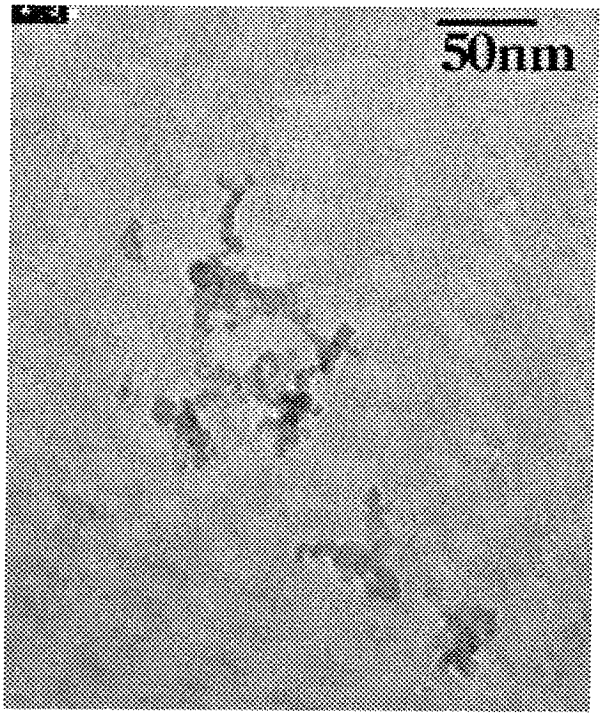

Figure 3.3: $TiO_2.nH_2O$ agglomerate particles with the same electrical mobility as a 50nm diameter sphere.

mary particles and a fine structure (Seto et al. 1995). In order to ensure that sintering of the primary particles did not occur to a large extent the particle source was kept to 523K. At the low reactor temperature, the agglomerates consist of partially hydrated titanium dioxide.

The particle source temperature was carefully controlled to ensure stability. The temperature of the agglomeration reactor was controlled by an Omega 2100 time-proportioning temperature controller driving a solid-state relay. Temperature baths around the TTIP vaporizer and the humidifier ensured that any variation in the ambient temperature did not affect the particle source.

In this study two TSI 3077 neutralizers were used. The neutralizers use the decay of Kr^{85} gas to produce α particles. The low energy β particles that are also produced in the radioactive decay are unable to penetrate the aluminum container. The activity at the time of the experiment was 1 mCi which, according to Liu and Pui (1974b), should be suitable for neutralizing an aerosol flow rate up to 17 l/min even if charge level on

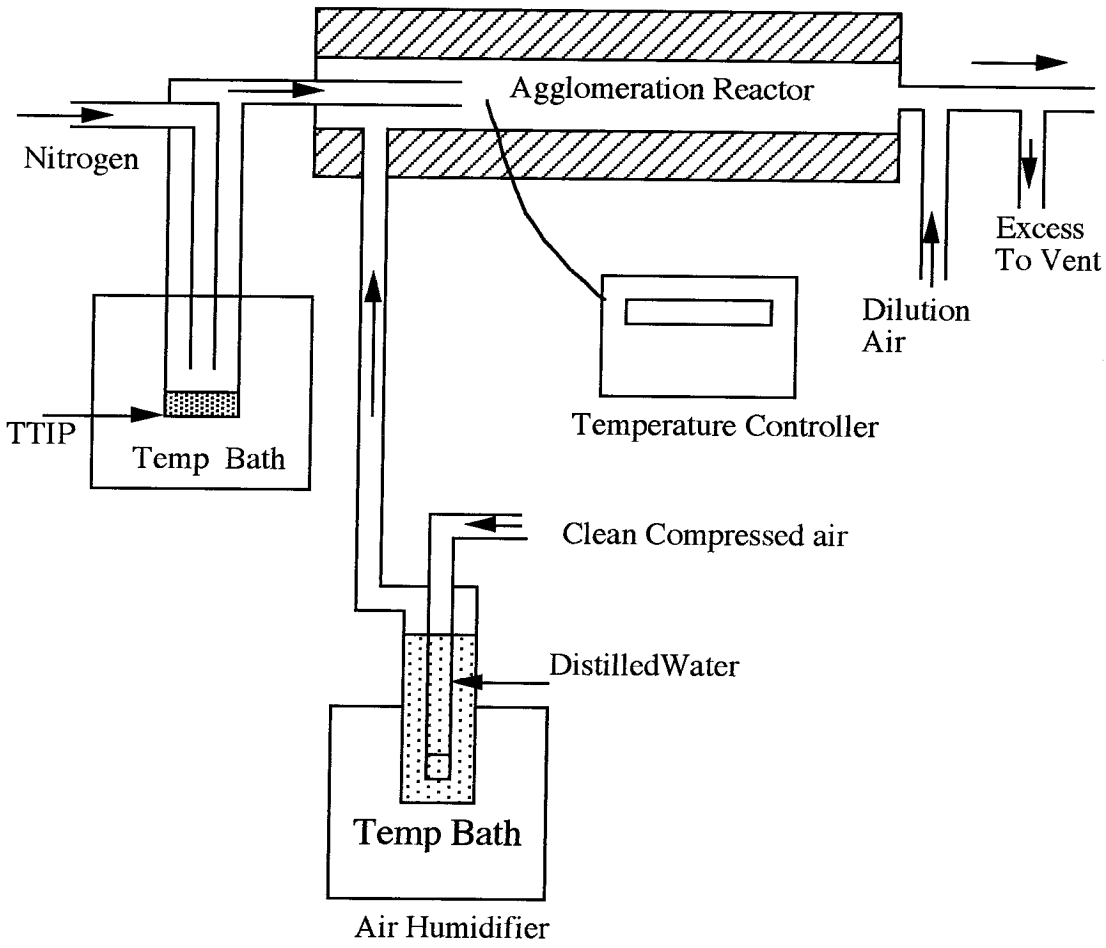

Figure 3.4: The hydrous titanium dioxide particle source.

the incoming aerosol approached the Rayleigh limit. In all the charging experiments, the flowrate through the chargers were kept at 1 l/min, allowing ample time for the aerosol agglomerates to reach the steady-state charge distribution.

3.3.2 Particle Characterization

To determine the charge distribution of the agglomerates we chose to use a TDMA setup. Wiedensohler et al.(1986) and Wiedensohler and Fissan (1991) used a similar system to measure the bipolar charge distribution for spherical aerosol particles in the 5-100nm diameter range. The electrometer used by Wiedensohler and Fissan was replaced in our experiment by a Condensation Nucleus Counter (CNC). While, Wiedensohler et al. (1986) measured NaCl particles with ± 1 and ± 2 charges, we measured agglomerates with up to $+4$ charges. Wiedensohler et al. (1986) found that the Fuchs theory with negative ions having a molecular weight of 130g mol^{-1} and positive ions of 148g mol^{-1}, matched the charge distribution of spherical NaCl particles in air over a range of temperatures from 298K to 373K.

A DMA classifies particles according to their electrical mobilities,

$$Z_p = \frac{ieD}{kT} \tag{3.25}$$

where i is the number of charges on the particle, e is the elementary unit of charge, D is the particle diffusivity, k is the Boltzmann constant and T is the absolute temperature. For spherical particles, this can be expressed explicitly in terms of the particle diameter, D_p, i.e.,

$$Z_p = \frac{ie}{3\pi\mu D_p} Cc\,(2\lambda/D_p)\,, \tag{3.26}$$

where μ is the gas viscosity, and the slip correction factor Cc is a nonlinear function of the particle Knudsen number which is the ratio of the mean-free path of the gas molecules to the particle diameter. For agglomerate particles, no such simple relationship exists. Agglomerate particles that are sized using a DMA are often characterized in terms of their mobility equivalent diameter, ie., the diameter of a spherical particle of the same mobility.

A version of the Knutson and Whitby (1975) cylindrical differential mobility analyser (DMA) which has similar dimensions similar to the original instrument but was modified to reduce diffusional losses was used to classify the $TiO_2.nH_2O$ particles. The ratio of the sheath flow to the aerosol flow was kept at 10:1 to ensure adequate resolution to discern the subtle variations in the charging distribution of the agglomerate. All tubing in the experiment was either copper or stainless steel and was grounded. The DMAs were operated with a negative voltage on the center electrode and the grounded outer cylinder so only agglomerates with positive charges were transmitted through the DMA.

After being classified by the first DMA, the particles were passed through a TSI 3077 neutralizer to a three-way valve with which the particles could then be passed either through another DMA, or directly to a TSI 3010 CNC as shown in Figure (3.5). The lengths of tubing and the numbers of angles of bends were identical in both paths to ensure that diffusional losses of fine particles would be identical in each case.

The size distribution was measured using a slow exponential scan of the voltage applied to the second DMA, typically of 300 second duration, to minimise mixing induced broadening of the measured size distributions (Russell et al.,1995). The data was recorded on an IBM PC. The size distributions were corrected for the transmission efficiency of the DMA (See Appendix II).

3.4 Results

Measured size distributions are shown in Figures (3.4) and (3.4) for mobility equivalent diameters of 50, 100, 150 and 200 nm. The size distributions contain many peaks. The largest peak occurs at the same mobility diameter at which the classifier (first) DMA was operated. These particles acquired one positive charge in the first diffusion charger and maintained that charge after the second diffusion charger. The main peak may also contain large agglomerates that went through both diffusion chargers with more than one charge. The peaks at higher mobility diameters than the main peak correspond to large agglomerates that left the first diffusion charger multiply charged but exited the second charger with only one positive charge. The peaks at smaller mobility diameters than the main peak correspond to agglomerates that had one positive charge after the

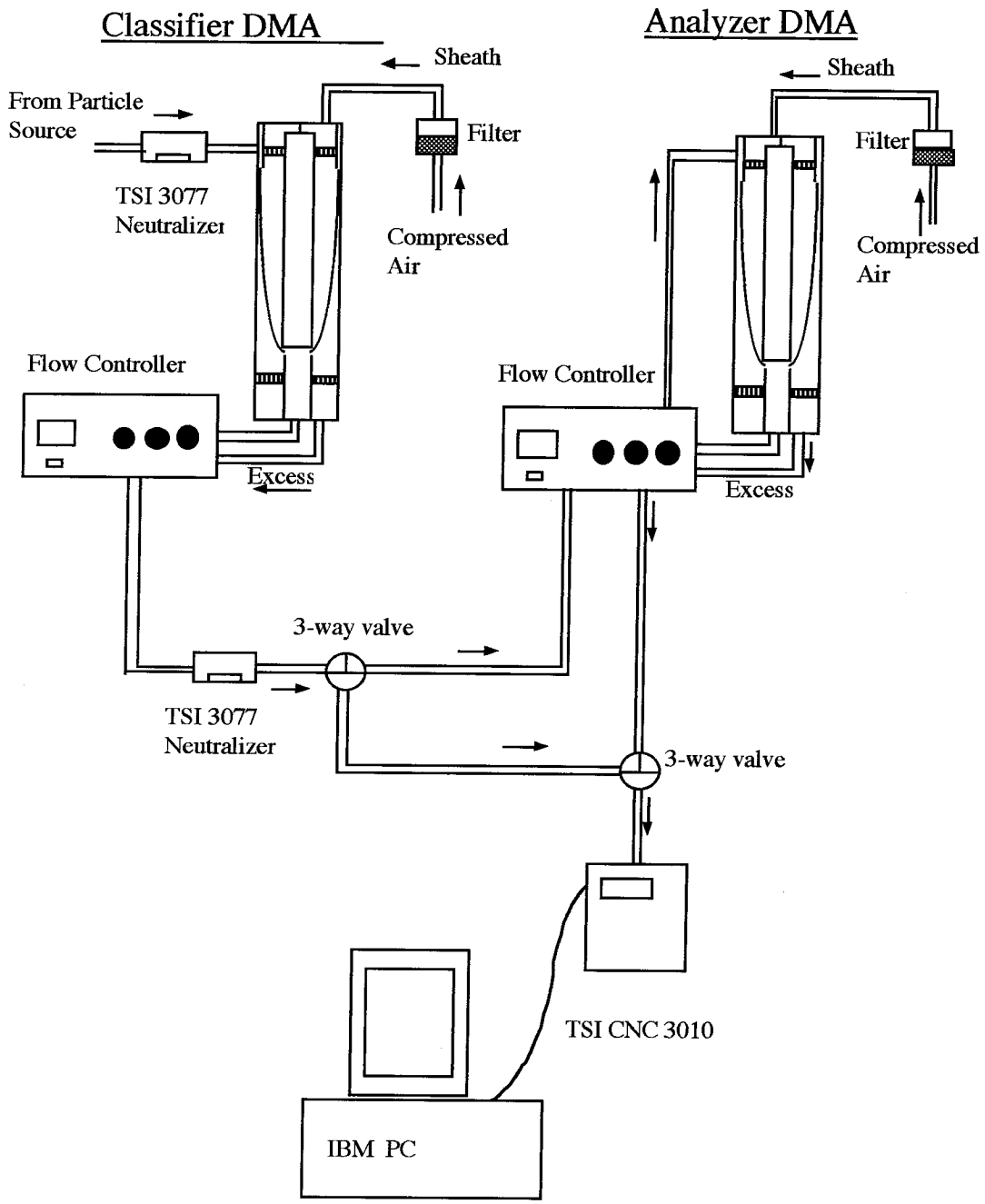

Figure 3.5: Flow diagram for the charge probability experiment. The length of tubing in each path was the same to avoid differences in wall losses.

first charger but were multiply charged in the second charger. This gives them a higher electrical mobility than singly charged particles so they are sized by the second DMA as agglomerates with smaller mobility diameters.

As the mobility diameter from the first agglomerate increases the number of peaks below the main peak increases. A triple charged peak can be seen in the 50nm distribution and a quadruply charged peak is discernible in the 100nm, 150nm, and 200nm distributions. The mobility diameters that correspond to the muliply charged agglomerates are given in Table (3.1). Triply charged particles are not measurable for agglomerates with mobility sizes below 45nm while quadruply charged particles are not measurable below an agglomerate mobility size of about 80nm. The lower limit on the particle concentrations was taken to be 1 particle/cm^3. Below this concentration, it was impossible to distinguish a peak from background noise.

The fraction of particles with a given charge was calculated by dividing the peak count by the total count measured by the CNC with the second DMA bypassed after correcting for particle losses in the DMA. Some of the particles that occur in a given mobility peak may belong to larger particles with higher charge. Following the approach of Rogak and Flagan (1992), a second iteration was carried out, using the first iteration results to account for multiple charging effects. The charge distribution was found only for agglomerates with mobility diameters from 20 to 215nm. Below 20nm the transmission efficiency of the cylindrical DMA declines while above 215nm the number concentration from the source declined. The charge distribution for the $TiO_2.nH_2O$ agglomerates is given in Figure (3.8). The fraction of singly charged particles initially increases as the agglomerate size increases from 20 to 50 nm. At larger particle sizes, it is more likely that two or more primary particles will carry a charge and the fraction of singly charged aggomerates decreases.

3.4.1 Comparison To Theory

Two theoretical bipolar charging theories for spherical particles have been developed. The Boltzmann theory has been shown to be inaccurate for particles diameters smaller than 30nm (Wen et al. 1984). The extended Fuchs model has been shown to be more accurate

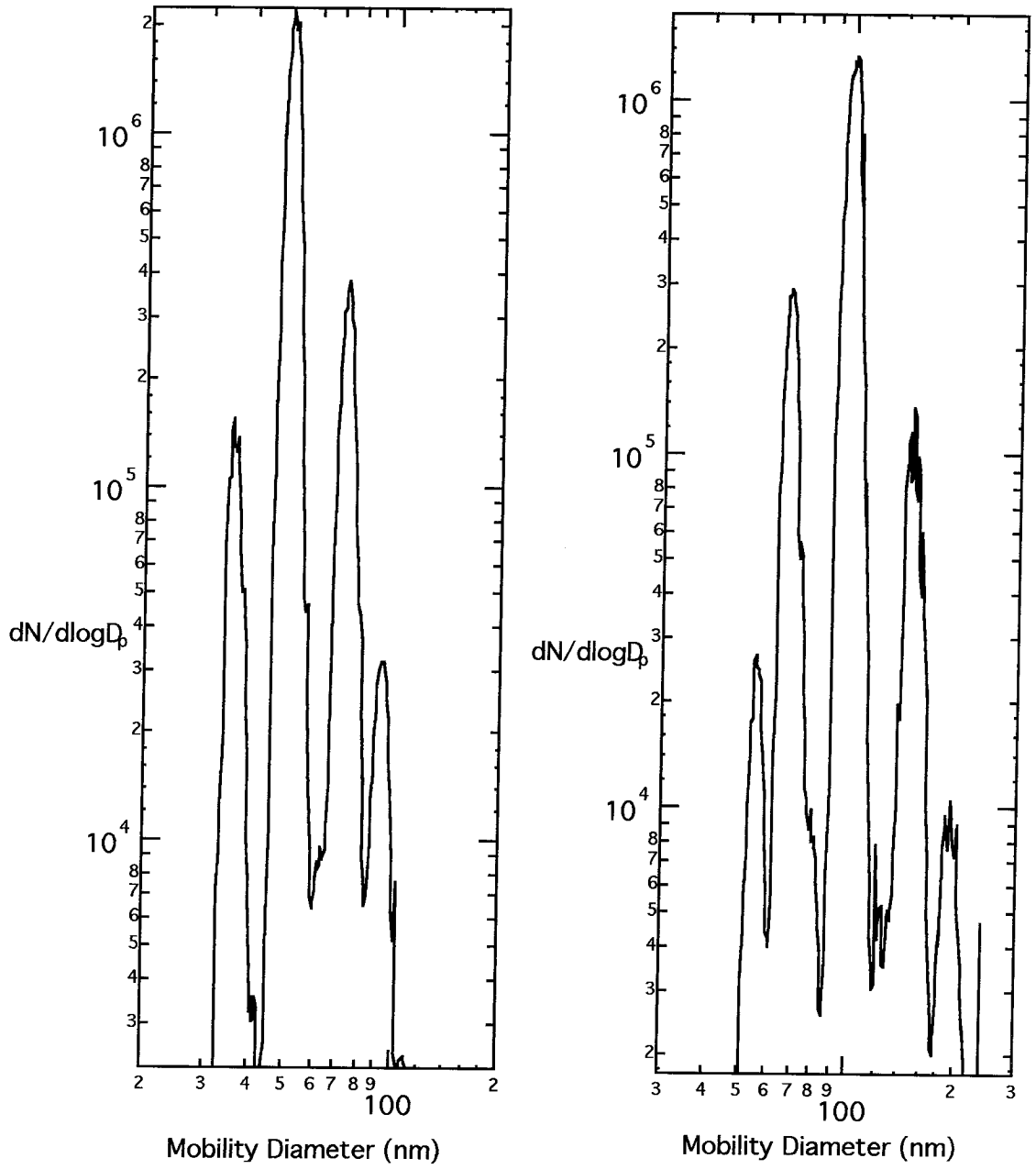

Figure 3.6: Left side of this figure shows the size distribution (cm^{-3}), of the $TiO_2.nH_2O$ agglomerates with the classifier DMA set to 50nm. The right side of this figure shows the size distribution (cm^{-3}), of the $TiO_2.nH_2O$ agglomerates with the classifier DMA set to 100nm.

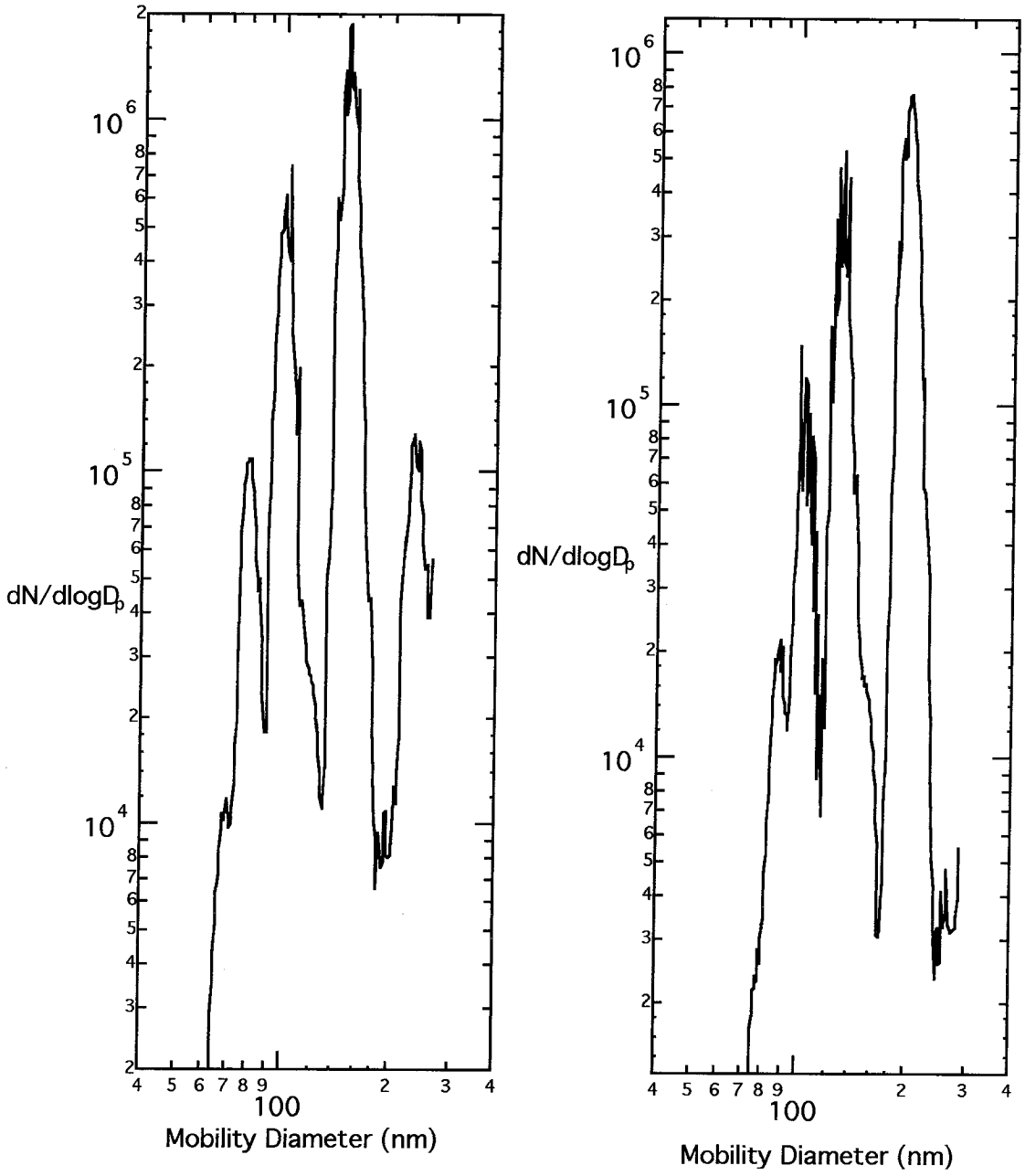

Figure 3.7: Left side of this figure shows the size distribution (cm^{-3}), of the $TiO_2.nH_2O$ agglomerates with the classifier DMA set to 150nm. The right side of this figure shows the size distribution (cm^{-3}), of the $TiO_2.nH_2O$ agglomerates with the classifier DMA set to 200nm.

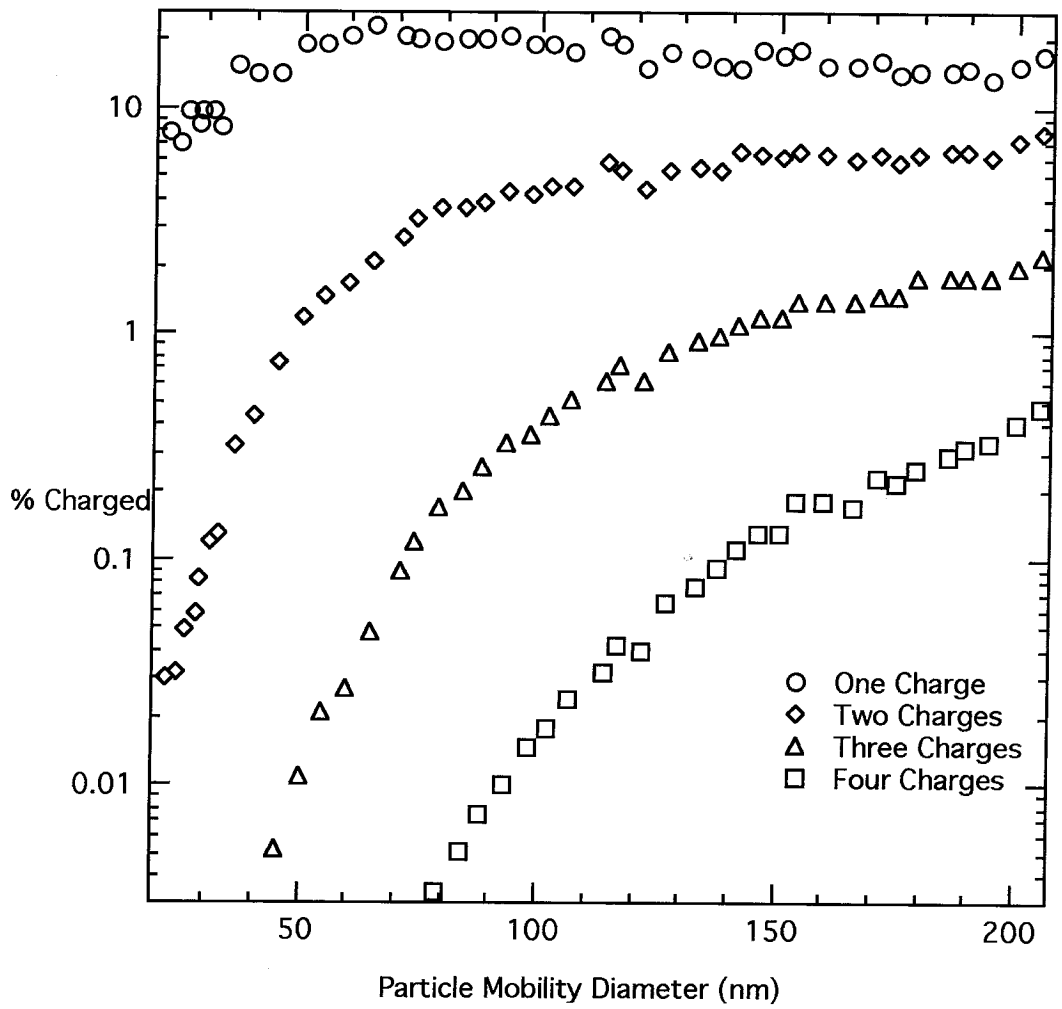

Figure 3.8: Percentage probability that a $TiO_2.nH_2O$ agglomerate particle has a given positive charge.

for small diameter dense particles (Hussin et al., 1983). Therefore, the experimental data for our agglomerates with primary particle diameters of 6nm are compared to Fuchs theory. Wiedensohler (1987) developed an empirical approximation to Fuchs theory for singly and doubly positively charged particles. To compare the experimental data of agglomerates that carry three and four positive charges, it was necessary to calculate the extended Fuchs theory for particles carrying up to five charges. It was assumed that no agglomerate carried six or more charges. Also, as the particle diameter increases, the percentage of particles carrying multiple charges increases. For our calculations the ion properties were taken from Hussin et al. (1983), with the positive and neagtive ion mobilities being 2.5×10^2 m/s and 2.1×10^2 m/s respectively. The collision probabilities of the ions with the particle were obtained following Fuchs (1963). Since we are concerned with bipolar charging the number of negative and positive ions were assumed to be equal and the percentage of particles with a given charge was obtained following Hussin et al. (1983) and Adachi et al.(1984).

The DMA classifies particles according to their electrical mobility. Therefore, the experimental steady-state charge distribution was compared to the extended Fuchs model for spheres of an equal mobility diameter. Agglomerates carrying one positive charge are compared to the theory in Fig. (3.9). Three regions are evident in this figure.

At particle diameters below 40nm, the extended Fuchs theory is in good agreement with the experimental data. At this size, the number of particles carrying more than two positive charges is negligible and the agglomerates consist of only a few primary particles. All particles undergo Brownian rotation which increases as the temperature increases. The volume that a spherical particle sweeps as it rotates is equal to the volume of the sphere. An agglomerate particle with a low fractal dimension will sweep a much larger volume on rotation than the volume of a sphere of equivalent mobility. This leads to an increase in the collision probability of an ion with an agglomerate, especially for the positive ion which has a lower diffusivity than the negative ion. However, for an agglomerate comprised of only a few primary particles, the enhancement of the collision probability is small leading to the close agreement of the theoretical and experimental data.

Above 120nm, the Wiedensohler approximation overpredicts the experimental data, as it neglects higher charges than two whose numbers increase as the particle

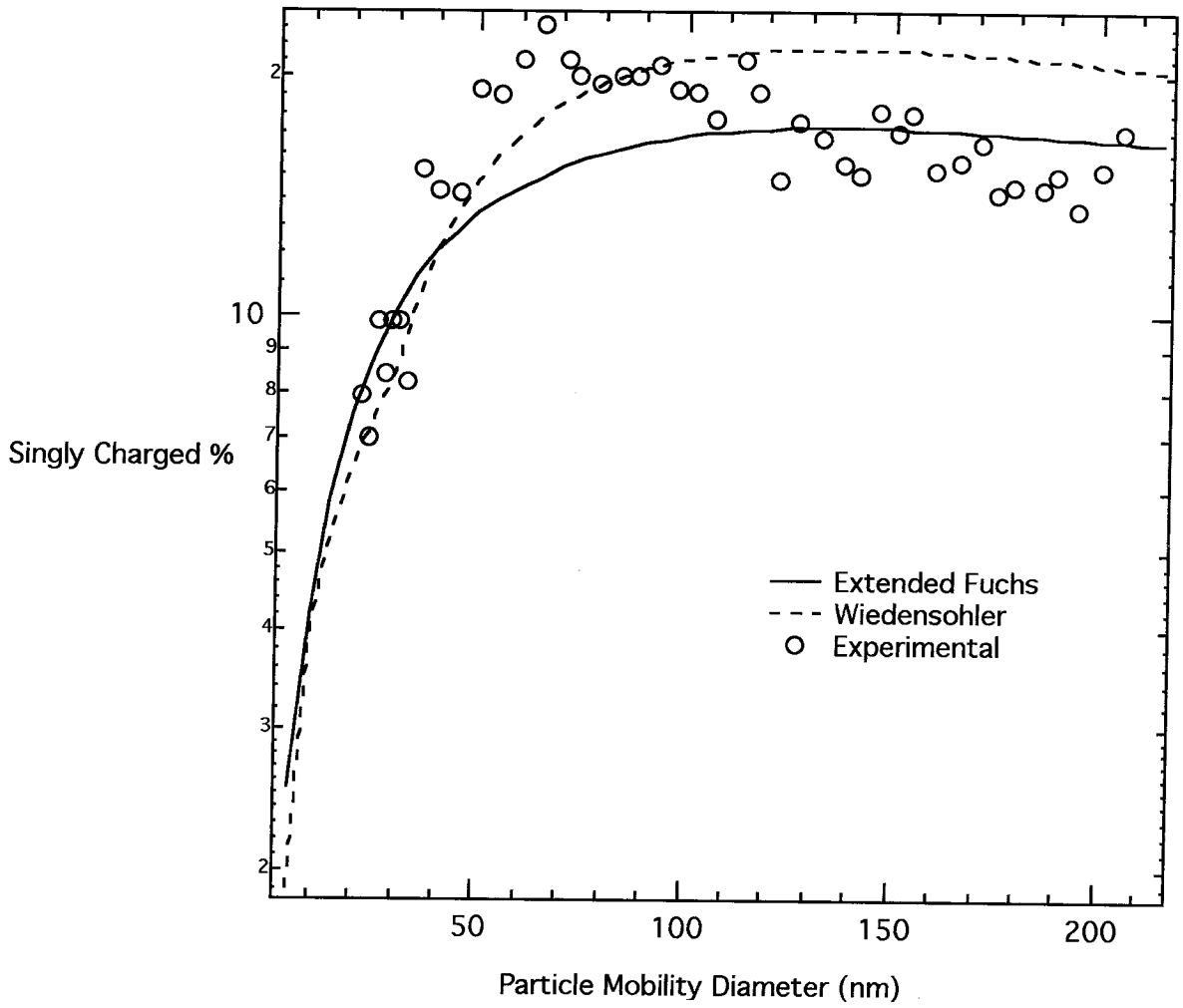

Figure 3.9: Comparison of the experimental data with the theories for single charge.

diameter increases. The region between 40nm and 120nm shows the experimental data above the Wiedensholer and the extended Fuchs model. The agglomerate particles between these sizes have a larger collision probability with the positive ions and are more likely to carry a charge. The collision probability of spherical particles carrying up to 5 positive ions with a positive ion is 1.0 at particle diameters above 120nm. As the particle diameter increases, the speed at which the agglomerates rotate decreases. Therefore as the agglomerate diameter increases, the enhancement of the agglomerate's collision probability with the ions decreases, until at 120nm both the agglomerate and the spheres have a collision probability of 1.0 for all charge levels.

A comparison of the experimental data for doubly charged particles to the ex-

tended Fuchs theory and the Wiedensohler approximation is shown in Fig. (3.10). Three regions are also evident in this figure. At particle diameters below 40nm both the extended Fuchs and Wiedensohler theory are a good match for the experimental data. At particle diameters larger than 120nm, the percentage of agglomerates carrying two positive charges is matched by the extended Fuchs model. The overprediction of the Wiedensohler approximation is due to the omission of particles carrying more than two charges. The region between 40nm and 120nm has both theories underpredicting the experimental data. The explanation for the increase in agglomerate charging compared to spherical particles is largely structural. A sphere cannot separate charges on it by more than its diameter, which for a sphere is identical to its mobility diameter. An agglomerate of the same mobility diameter as a sphere can be considerably longer on its main axis than the sphere's diameter. The force between two charges is inversely proportional to the distance between them, so two charges at opposite ends of the main axis of the agglomerate will be a more stable situation than two charges on a sphere of the same mobility diameter.

The percentage of particles carrying three and four charges is compared to the extended Fuchs model in Fig. (3.11). The experimental data for the agglomerates is larger than the theory for all the mobility diameters measured. The agglomerate can locate multiple charges further apart than a sphere, and the rotation of the agglomerate increases the collision probability with the ions.

To invert a size distribution, the steady-state charge distribution needs to be known exactly. For a sphere, the extended Fuchs model has been shown to be accurate (Wiedensoler et al., 1986). It would be convenient if the steady-state charge distribution of an agglomerate could be related to the extended Fuchs distribution of an equivalent sphere. Rogak and Flagan (1992) suggest that the charging equivalent sphere diameter of an agglomerate is approximately 1.1 times larger than the mobility equivalent sphere diameter.

To calculate the charge equivalent diameter, the percentage charged for each data point was compared to the extended Fuchs theory. The charge equivalent diameter is defined as the diameter at which the extended Fuchs theory gives the same percentage charged as the experimental point. The ratio of the charge equivalent diameter to the agglomerate mobility diameter was calculated. The resulting points can be seen in Fig.

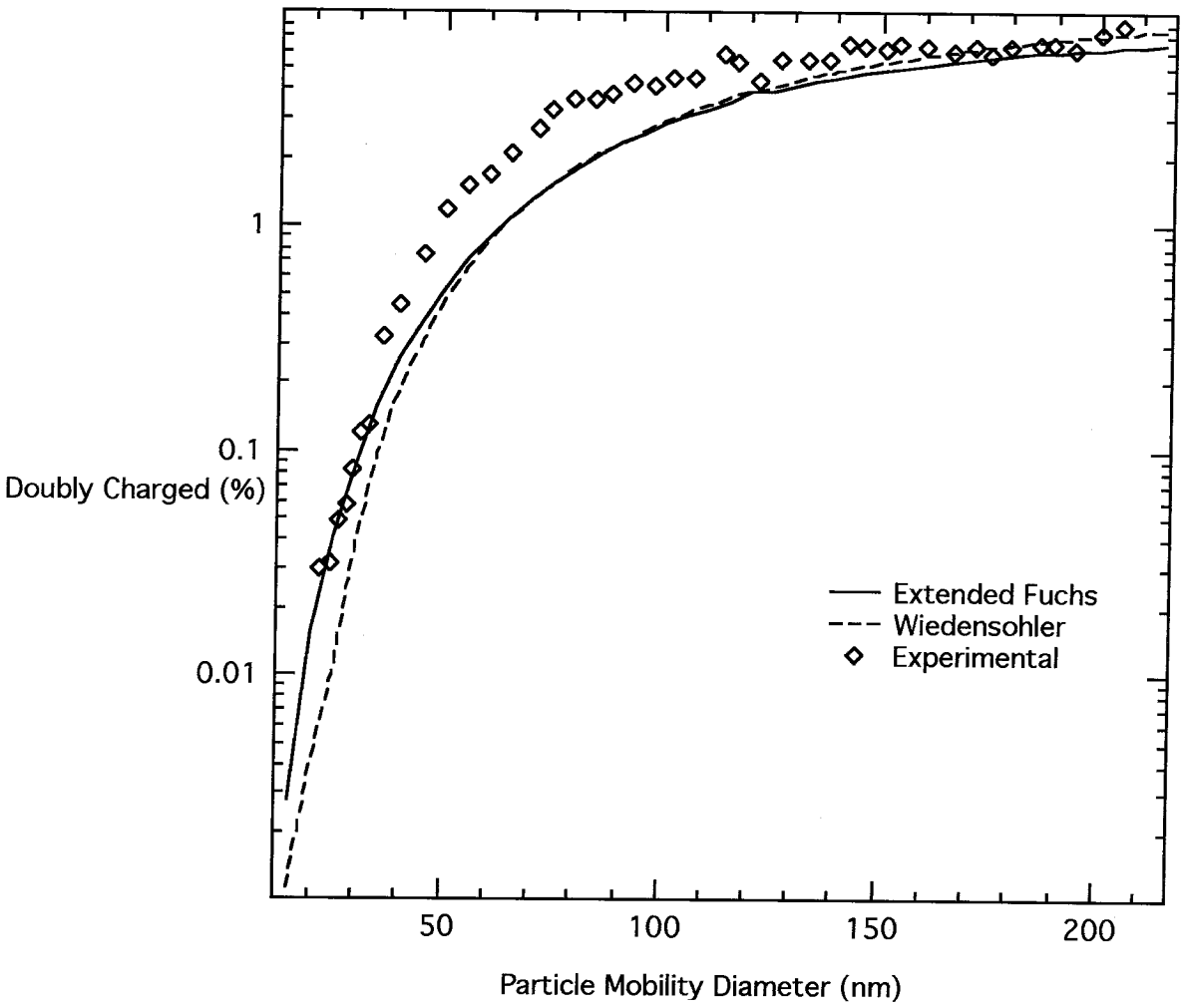

Figure 3.10: Comparison of the experimental data with the theories for double charge.

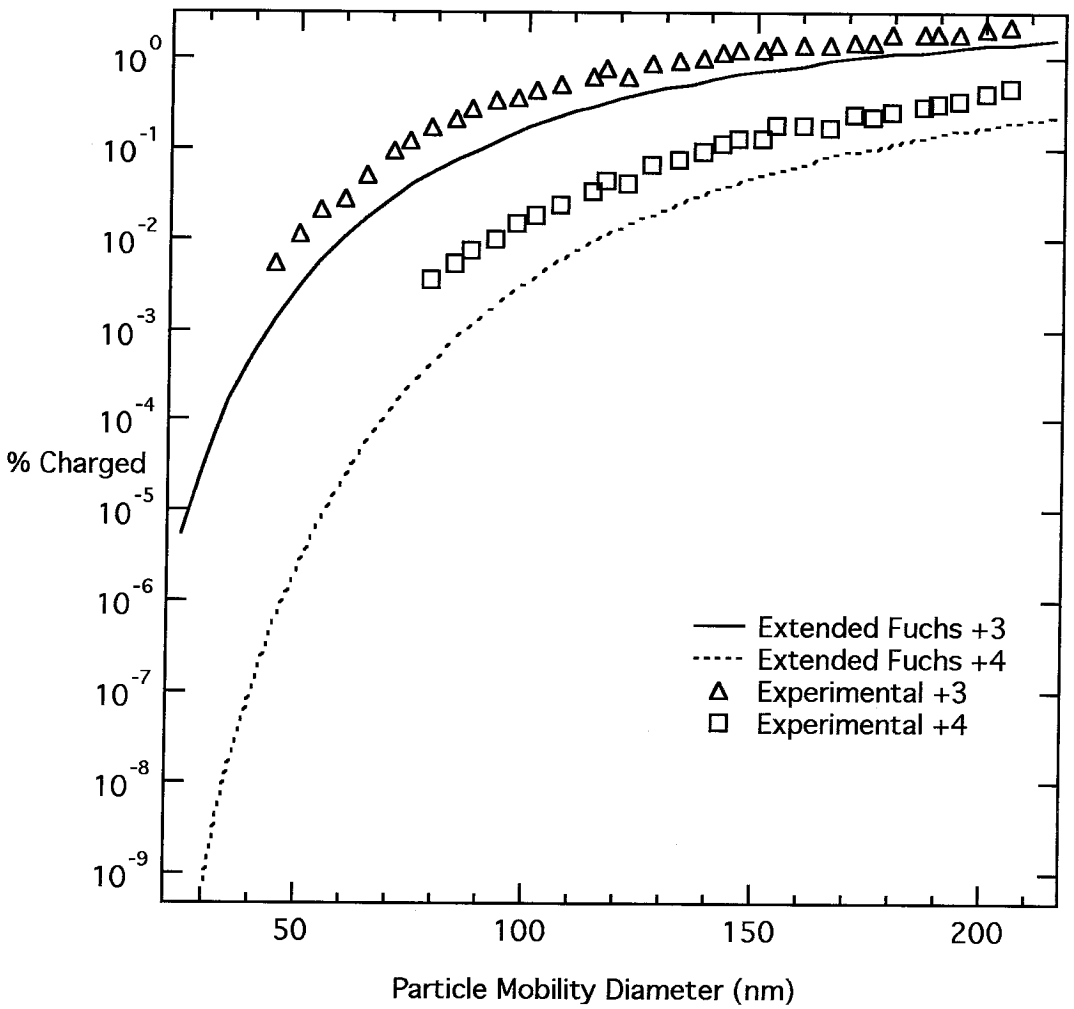

Figure 3.11: Comparison of the experimental data with the theories for three and four charges.

(3.12). For the singly charged particles this process was only possible for agglomerates with mobility diameters below 45nm. Agglomerates larger than 45nm have a larger percentage charged than the maximum of the extended Fuchs theory. The multiply charged curves do not reach a maximum in our range of interest, and so the equivalent diameter ratio can be calculated for the entire range of agglomerate diameters.

The singly charged points in Fig. (3.12) are widely scattered. However, the multiply charged points are arranged around an equivalent diameter ratio of approximately 1.25. This result is for an agglomerates of fractal dimension of 1.8 and comprised of primary particles that are 6nm in diameter. The equivalent diameter ratio of 1.25 is specifically for this geometry and will differ with fractal dimension.

3.5 Summary

The steady-state bipolar charge distribution of aerosol agglomerates with primary particles smaller than 20nm in diameter was investigated experimentally using a tandem DMA apparatus. The percentage of agglomerates carrying one to four positive charges was then calculated. The experimental data was compared to the extended Fuchs theory and to Wiedensohlers approximation, which does not take into account particles carrying more than two charges. The extended Fuchs theory was calculated with the assumption that no particles carried more than five charges. The ion properties were taken from Hussin et al.(1983), and the concentration of negative and positive ions were assumed to be equal.

Three distinct regions were seen in the percentage of agglomerates carrying one charge. Agglomerates with mobility diameters smaller than 40nm agree with both the Wiedensohler and the extended Fuchs theory. As the mobility diameter of the agglomerate increases past this value the experimental values were underestimated by the theories. This difference was attributed to the rotation of the agglomerates increasing the collision probability with the ions. As the mobility diameter of the agglomerates increases the Brownian rotation decreases. For agglomerates with mobility diameters larger than 120nm, the extended Fuchs theory matched the experimental steady-state charge distribution.

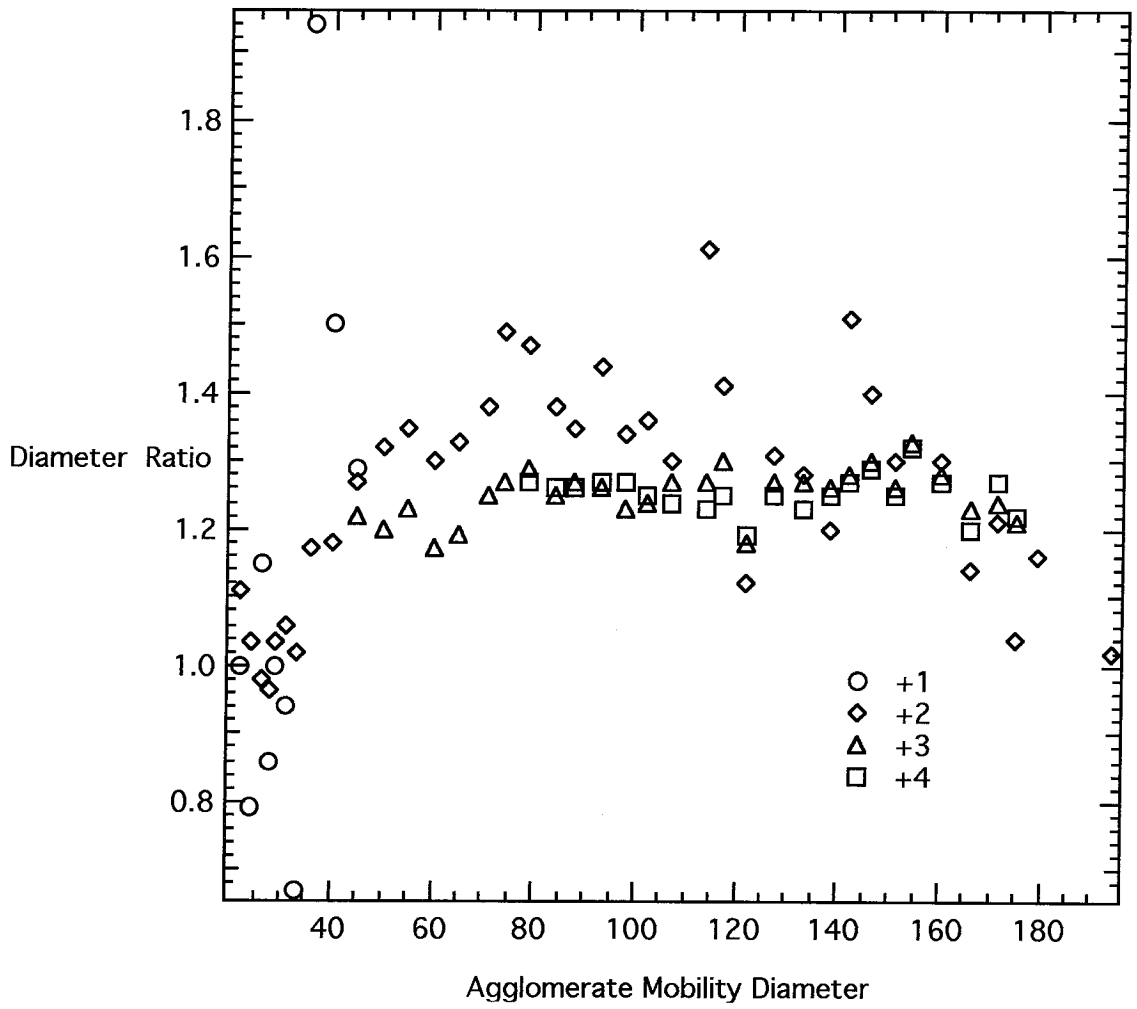

Figure 3.12: Ratio of the charge equivalent diameter to the mobility diameter for agglomerate particles carrying one or more positive charges.

The experiments showed that there were more multiply charged agglomerates than either theory predicts. The difference was attributed to the agglomerate being able to position charges further apart than a mobility equivalent sphere. Some of the difference between the two theories comes from the different ion properties used. It would have been helpful to know the positive and negative ion mobilities, but no experiemnts were carried out to determine this. Relative humidity may have an effect on the ion properties but the relative humidity inside the apparatus was not measured.

To enable size distribution inversion the steady-state charge distribution must be known. For agglomerates, one approach has been to define a charge equivalent diameter of the agglomerate. To probe the relationship between the agglomerate mobility diameter and the equivalent charge diameter, the experimental data was used to find the equivalent diameter ratio. For a sphere this ratio is one. The equivalent diameter ratio for agglomerate was found to be approximately 1.25. This value is structure specific and will change with fractal dimension. The bipolar steady-state charge distribution of the agglomerates was found to exceed the theoretical predictions and use of these theories when analyzing agglomerates will lead to systematic errors.

3.6 Acknowledgements

The author wishes to thank Dr. Shou-hua Zhang for his assistance in the calibration of the DMAs used in the study. Funding support was received from the NSF under grant CTS-9113193 and the International Fine Particle Research Institute, grant number FRR 20-07.

One charge	Two Charges	Three Charges	Four Charges
22	17	-	-
24	19	-	-
25	19	-	-
29	21	-	-
30	22	-	-
32	24	-	-
35	25	-	-
40	29	-	-
45	32	26	-
50	35	29	-
55	39	31	-
60	42	34	-
65	45	37	-
70	49	40	-
75	51	41	-
80	54	44	38
85	57	46	40
90	61	49	42
95	63	51	44
100	66	53	47
105	69	56	48
110	72	59	50
115	76	61	52
120	79	63	55
125	84	67	58
130	85	68	58
135	89	71	61
140	92	74	63
145	98	75	65
150	98	78	67
155	100	80	69
160	102	81	70
165	107	84	73
170	110	87	75
175	113	90	76
180	115	91	78
185	118	91	78

Table 3.1: Experimental Mobility diameters of $TiO_2.nH_2O$ agglomerates with multiple charges

Bibliography

Adachi, M., Kousaka, Y., and Okuyama, K. (1985). Unipolar and bipolar diffusion charging of ultrafine aerosol particles. *Journal of Aerosol Science*, 16(2):109–123.

Adachi, M., Okuyama, K., Kousaka, Y., Kozuru, H., and Pui, D. (1989). Bipolar diffusion charging of aerosol particles under high particle /ion concentration ratios. *Aerosol Science and Technology*, 11(2):144–156.

Büscher, P., Schmidt-Ott, A., and Fissan, H. (1991). Efficiency of unipolar diffusion charging of ultrafine aerosol as function of the nt-product. *Journal of Aerosol Science*, 22(Supplement 1):S235.

Cheng, Y. and Yeh, H. (1981). Equilibrium bipolar charge distribution of aerosols consisting of chains of uniform spheres. *Journal of Colloid and Interface Science*, 84(2):444–450.

Cheston, W. (1964). *Elementary Theory of Electric and Magnetic fields.* John Wiley and Sons, Inc., New York.

Davison, S. and Gentry, J. (1984). Modeling of ion mass effects on the diffusion charging process. *Journal of Aerosol Science*, 15(3):262–263.

Dua, S., Mayya, Y., and Kotrappa, P. (1979). Equilibrium charge distribution on doublets and triplets of uniform 0.500 μ m diameter polystyrene spheres - an experimental study. *Journal of Aerosol Science*, 11(4):415–419.

Filippov, A. (1994). Charge distribution among non-spherical particles in a bipolar environment. *Journal of Aerosol Science*, 25(4):611–615.

Filippov, A. and Burtscher, H. (1994). Bipolar charging of aerosol particles in electropositive gas of high purity. *Aerosol Science and Technology*, 21(1):37–45.

Flagan, R. and Seinfeld, J. H. (1988). *Fundamentals of Air Pollution Engineering.* Prentice Hall, New Jersey 07632.

Gentry, J. and Brock, J. (1967). Unipolar diffusion charging of small aerosol particles. *The Journal of Chemical Physics*, 47(1):64–69.

Han, R. and Gentry, J. (1991). Unipolar and bipolar charging of platelets. *Journal of Aerosol Science*, 22(Supplement 1):S227–S230.

Han, R., Pao, J., Wang, C., and Gentry, J. (1990). Electrical charging of aggregates: simulations,data,analysis and experiments. *Journal of Aerosol Science*, 21(Supplement 1):S115–S118.

Han, R., Ranade, M., and Gentry, J. (1991). Experimental measurement of unipolar charging of carbon fibers. *Journal of Aerosol Science*, 22(Supplement 1):S231–S234.

Hussin, A., Scheibel, H., Becker, K., and Porstendörfer, J. (1983). Bipolar diffusion charging of aerosol particles - I: Experimental results within the diameter range 4-30nm. *Journal of Aerosol Science*, 14(5):671–677.

Keady, P., Quant, F., and Sem, G. (1993). *Model 3934 SMPS : Differential Mobility Particle Sizer: A New Instrument for High Resolution Aerosol Size Distribution Measurement Below 1μm.* TSI Incorporated, St. Paul, Minnesota.

Kousaka, Y., Adachi, M., Okuyama, K., Kitada, N., and Motouchi, T. (1983). Bipolar charging of ultrafine aerosol particles. *Aerosol Science and Technology*, 2(4):421–427.

LaFramboise, J. and Chang, J. (1977). Theory of charge deposition on charged aerosol particles of arbitrary shape. *Journal of Aerosol Science*, 8(4):331–338.

Liu, B. and Pui, D. (1974). Electrical neutralization of aerosols. *Journal of Aerosol Science*, 5(4):465–472.

Rogak, S. and Flagan, R. (1992). Bipolar diffusion charging of spheres and agglomerate aerosol particles. *Journal of Aerosol Science*, 23(7):693–710.

Romay, J. and Pui, D. (1992a). Free electron charging of ultrafine aerosol particles. *Journal of Aerosol Science*, 23(7):679–692.

Romay, J. and Pui, D. (1992b). On the combination coefficient of positive ions with ultrafine neutral particles in the transition and free molecule regimes. *Aerosol Science and Technology*, 17(2):134–147.

Russell, L., Flagan, R., and Seinfeld, J. (1995). Asymmetric instrument response resulting from mixing effects in accelerated DMA-CPC measurements. *Aerosol Science and Technology*, 23(4):491–509.

Seto, T., Shimada, M., and Okuyama, K. (1995). Evaluation of sintering of nanometer-sized titania using aerosol method. *Aerosol Science and Technology*, 23(2):183–200.

Takahashi, K. and Kudo, A. (1973). Electrical charging of aerosol particles by bipolar ions in flow type charging vessels. *Journal of Aerosol Science*, 4(3):209–216.

Vijayakumar, R. and Whitby, K. (1984). Bipolar steady state charge fraction of ultrafine aerosols. *Aerosol Science and Technology*, 3(1):25–30.

Vincent, J., Johnston, W., Jones, A., and Johnston, A. (1981). Static electrification of airborne asbestos: A study of its causes, assessment and effects on deposition in the lungs of rats. *American Industrial Hygiene Association Journal*, 42:711–720.

Vomela, R. and Whitby, K. (1967). The charging and mobility of chain aggregate smoke particles. *Journal of Colloid and Interface Science*, 25(1):568–576.

Wen, H., Reischl, G., and Kasper, G. (1984a). Bipolar diffusion charging of fibrous aerosol particles - II. charge and electrical mobility measurements on linear chain aggregates. *Journal of Aerosol Science*, 15(2):103–122.

Wen, H., Reischl, G., and Kasper, G. (1984b). Bipolar diffusion charging of fibrous aerosol particles - I. charging theory. *Journal of Aerosol Science*, 15(2):89–101.

Wiedensohler, A. (1988). An approximation of the bipolar charge distribution for particles in the submicron size range. *Journal of Aerosol Science*, 19(3):387–389.

Wiedensohler, A. and Fissan, H. (1991). Bipolar charge distributions of aerosol particles in high purity argon and nitrogen. *Aerosol Science and Technology*, 14(3):358–364.

Wiedensohler, A., Lutkemeier, E., Feldpausch, M., and Helsper, C. (1986). Investigation of the bipolar charge distribution at various gas conditions. *Journal of Aerosol Science*, 17(3):413–416.

Yeh, H. and Cheng, Y. (1983). Theoretical study of equilibrium bipolar charge distribution on nonuniform primary straight chain aggregate aerosols. *Aerosol Science and Technology*, 2(1):383–388.

Chapter 4 Aerosol Agglomerate Orientation in an Electric Field

Il faut n'appeler Science que l'ensemble des recettes qui réussissent toujours. - Tout le reste est littérature.

Science is simply the aggregate of all the recipes that are always successful. The rest is literature.

Paul Valéry Moralités.(1932) p41.

4.1 Abstract

Aerosol agglomerates are fractal-like structures that are not, in general, spherically symmetric. When they are classified using a differential mobility analyzer, any alignment of the particles in the electric field will bias the measurements. This paper examines the rotational convection-diffusion of an aerosol particle in an electric field. The extent of orientation is shown to be a function of a dimensionless ratio between the electrostatic potential energy of rotation and the thermal energy. The orientation distribution function for linear agglomerates is calculated numerically as a function of this parameter, Γ. The numerical solutions and an orientation dependent drag force are used to probe the influence of orientation for a linear chain agglomerate and a fractal agglomerate as a function of the primary particle size and the number of primary particles. Comparisons are made to experimental data and the numerical solutions are used to explain the mobility increases seen in some sintering studies.

4.2 Introduction

A charged aerosol particle can be classified using a differential mobility analyzer (DMA) according to its electric mobility, Z_e, defined as the ratio of the terminal migration velocity, v_E, of the charged particle to the strength of the electric field, E. This mobility is related to the charge on the particle and the aerodynamic resistance to motion, (Flagan and Seinfeld, 1988)

$$Z_e = \frac{v_E}{E} = \frac{ne}{f}, \tag{4.1}$$

where f is the ratio of the force acting on the particle to the migration velocity. For spheres

$$f = \frac{3\pi\mu D_p}{C_c}. \tag{4.2}$$

The electrical mobility is then

$$Z_e = \frac{neC_c}{3\pi\mu D_p}, \tag{4.3}$$

where C_c is so-called the Cunningham slip correction factor, μ is the viscosity of the fluid, and D_p is the diameter of the particle. In differential mobility analysis, the particles

typically only carry one positive charge, $n = +1$. The Cunningham slip correction factor accounts for the decrease in the drag force when the particle diameter becomes comparable to or smaller than the mean free path, λ, of the suspending gas, i.e., when the Knudsen number,

$$Kn = \frac{2\lambda}{D_p}, \tag{4.4}$$

approaches or exceeds unity. If the Knudsen number is large, (Kn $\gg$ 1), the particle is said to be in the free molecular regime. Conversely, particles with Knudsen numbers much smaller than unity are in the continuum regime. The size range between these two extremes, where the Knudsen number is close to unity, is called the transition regime. The slip correction factor is a function of the Knudsen number,

$$C_c\,(\mathrm{Kn}) = 1 + \mathrm{Kn}\left(A + B\exp\left(\frac{-C}{\mathrm{Kn}}\right)\right), \tag{4.5}$$

where A = 1.257, B= 0.4 and C=1.1 for spheres. (Seinfeld 1986).

For non-spherical particles the drag factor, f, is less well understood. Indeed, for agglomerates, no exact result exists. Typically, the aerodynamic response of a non-spherical particle is compared to a sphere of similar mobility (Rogak et al. 1993). This comparison assumes that all orientations are equally probable and the particle does not align with the imposed field. However, under the attraction of the applied electric field, an irregularly shaped agglomerate may align in a preferred direction (depending on the location of the charge on the surface, the shape of the particle, and the strength of the applied field). If the charge is localized near the end of the particle, this alignment can reduce the particle's projected area, decreasing the drag force and thereby increasing the apparent electrical mobility.

The orientation of non-spherical particles in shear flow has been a subject of research in the colloidal field for many years (Alexander and Johnson, 1949; Doi and Edwards, 1986; Van de Ven, 1989). The equivalent problem in aerosols has also been examined theoretically (Fuchs 1964), and extended more recently to particles in laminar shear flow (Krushkal and Gallily 1984). Krushkal and Gallily developed an orientation distribution function to describe the alignment of particles in spherical co-ordinates. They found that the orientation was dependent on a rotational Peclet number which they defined as the velocity gradient divided by the rotational diffusion coefficient.

The orientation of charged aerosols in an electric field has been investigated experimentally by Kasper and Shaw (1983) and by Wen and Kasper (1984). Kasper and Shaw, (1983) studied Fe_2O_3 chain aggregates using an aerosol centrifuge, a cascade impactor, and an electrical aerosol analyzer. Fibrous aerosol particles were observed to align perpendicular to the direction of flow during sedimentation in an aerosol centrifuge. In the cascade impactor the fibrous particles had an orientation that was mostly parallel to the direction of flow. Using measurements of differences in apparent size as determined with these instruments, Kasper and Shaw found a maximum difference of 1.25 between the aerodynamic diameter of chain aggregates that were oriented parallel versus normal to the direction of motion. In the electrical aerosol analyser, the chains showed much lower mobility equivalent diameters than was theoretically predicted. This difference was attributed to multiple charging on the chains.

This paper seeks to extend the theoretical approach found in the colloid literature to obtain a solution for the orientation of non-spherical agglomerates in an electric field. This solution will then be used to determine the necessary conditions for orientation effects to be included in electrical sizing of particles.

4.3 Rotational Convective - Diffusive Theory

Non-spherical particles may preferentially align with a laminar shear flow (Fuchs 1964). Non-spherical charged particles also orient themselves when in an electric field (Wen and Kasper 1984). A charged, non-spherical particle in a DMA will be subject to both effects. The resulting orientation will be a sum of the drag and electrical effects and can be decoupled by noting that the Stokes equation is linear. The rotation of charged particles due to the electric field can therefore be analyzed separately. This rotation is described by the rotational convective-diffusive equation (Van de Ven, 1989)

$$\frac{\partial P}{\partial t} = \nabla \cdot (D_r \cdot \nabla P) - \nabla \cdot (\omega P), \tag{4.6}$$

where D_r is the rotational diffusion tensor, ω is the angular velocity of the particle and $\mathrm{P}(r, \theta, \phi)$ is the particle orientation distribution function. $\mathrm{P}(r, \theta, \phi)$ is the probability that a particle will be in the interval $(\theta, \theta + \delta\theta)$ and $(\phi, \phi + \delta\phi)$.

Particles are typically exposed to the electric field in a mobility analyzer significantly longer than the rotational relaxation time, τ_{Rot}, so, only the steady-state solution to the convective-diffusive equation is required. The validity of this assumption will later be examined later. For the rotation of a non-spherical particle, only the angular part of the convective-diffusive equation need be considered (McQuarrie 1976). Furthermore, in the absence of strong shear, i.e., plug flow, the azimuthal dependence of the particle orientation distribution function can be neglected, simplifying equation (4.6) to

$$\frac{D_r}{\sin\theta}\frac{\partial}{\partial\theta}\left(\sin\theta\frac{\partial P}{\partial\theta}\right) = \nabla\cdot(\omega P). \tag{4.7}$$

The rotational diffusivity can be related to the rotational drag through a derivation that is analagous to the Stokes-Einstein relation (Doi and Edwards, 1986)

$$D_r = \frac{kT}{f_r}, \tag{4.8}$$

where k is the Boltzmann constant, T is the absolute temperature, and f_r is a rotational friction tensor. For an agglomerate particle the angular velocity, ω, is evaluated using a balance of the electrostatic and drag torques acting on the agglomerate.

The electrical torque is simply

$$T_e = eER_c\sin\theta, \tag{4.9}$$

where e is the electron charge, E is the elctric field, R_c is the distance from the center of the particle to the charge, and θ is the angle that the line from the charge to the center of the particle makes with the electric field as illustrated in Figure (4.1). If the torque equation had no θ dependence, then the probability distribution function could be expressed as a Boltzmann distribution. Since this is not the case, the torque due to drag forces requires a more detailed description of the particle structure.

Agglomerate aerosols are frequently modeled as ensembles of mass-fractal particles. Assuming that the agglomerates are assemblies of spherical primary particles of radius, a, the number of primary particles in a radius, r, from the center of mass is

$$N = K\left(\frac{r}{a}\right)^{D_f}, \tag{4.10}$$

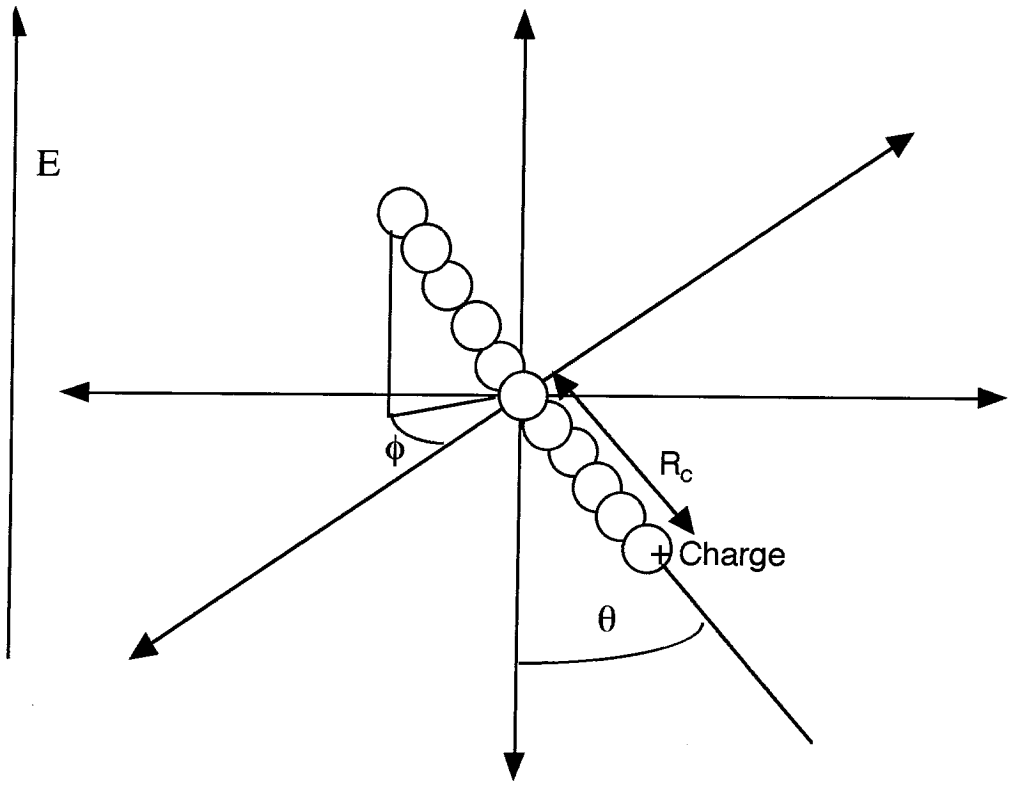

Figure 4.1: Schematic of a chain agglomerate showing charge radius R_c for the torque balance.

where a is the primary particle radius, D_f is the fractal dimension and K is a constant. The number of primary particles contained in a given radius, r, can therefore be written as

$$dN = D_f K \left(\frac{r}{a}\right)^{D_f-1} d\left(\frac{r}{a}\right). \tag{4.11}$$

The viscous resistance of a straight chain agglomerate in the free molecular regime was found to be dependent on the number and size of primary particles in the chain (Dahneke, 1982). Extending Dahneke's reasoning to a fractal agglomerate, the sum of the drag on the individual primary particles gives the drag on the agglomerate. The tangential velocity at a radius, r, from the center of an agglomerate particle is

$$u = r\omega = a\omega \left(\frac{r}{a}\right). \tag{4.12}$$

Using Equations (4.11) and (4.12), the incremental drag force due to the rotational motion of primary particles within a spherical shell of the agglomerate can be written as

$$f_d d(\frac{r}{a}) = f_1 \alpha a \omega D_f K \left(\frac{r}{a}\right)^{D_f} d\left(\frac{r}{a}\right), \tag{4.13}$$

where f_1 is the friction factor for a single primary particle, and α accounts for the shielding of one particle on another. The total torque associated with the drag forces is obtained by integrating from the center of rotation to the outermost primary particle at a radius, R_{max},

$$T_d = \int_0^{R_{max}} frdr \tag{4.14}$$

Substituting Eq.(4.13) for the drag force on the spherical shell, the aerodynamic torque that resists the particle rotation becomes

$$T_d = \frac{f_1 \alpha a^2 \omega D_f K}{(D_f+2)} \left(\frac{R_{max}}{a}\right)^{D_f+2} = f_r \omega. \tag{4.15}$$

Equating the torques due to drag, Eq.(4.15), and electrical forces, Eq.(4.9) and using Eq.(4.8) yields the rotational frequency as a function of θ, the applied electric field, and through the diffusivity, the particle characteristics

$$\omega = \frac{eER_c D_R \sin\theta}{kT}. \tag{4.16}$$

By substitution of Eq.(4.16) into Eq.(4.7), the rotational convective-diffusive equation now becomes

$$\frac{1}{\sin\theta}\frac{\partial}{\partial\theta}\left(\sin\theta\frac{\partial P}{\partial\theta}\right) = \Gamma\sin\theta\frac{\partial}{\partial\theta}\left(P\sin\theta\right). \tag{4.17}$$

The tendency of the particles to orient in the applied electric field depends on the dimensionless parameter,

$$\Gamma = \frac{eER_c}{kT} \tag{4.18}$$

This constant is the ratio of the coulombic and thermal energies of the particle, with respect to rotation in the DMA. Γ is an electrical analogue of the rotational Peclet number described by Krushkal and Gallily (1984). For small values of Γ, the thermal forces dominate, leading to a random distribution of agglomerate orientations. Conversely, for large values of Γ, the particle has a strong interaction with the electrical field, leading to alignment nearly parallel to the electric field. Thus, as Γ tends to infinity, the orientation distribution function approaches a delta function at $\theta = \pi$.

The rotational convective-diffusive equation can now be rewritten as a function of Γ

$$\frac{\partial^2 P}{\partial\theta} + \frac{\partial P}{\partial\theta}\left(\cot\theta - \Gamma\right) - P\left(\Gamma\cos\theta\right) = 0. \tag{4.19}$$

Equation (4.19) describes the orientation distribution function as a function of the angle that the agglomerate makes with the applied electric field, θ. Two boundary conditions are needed. For any agglomerate, the integral of the orientation distribution function over all possible orientations must equal unity,

$$\int_{-\pi}^{\pi} P(\theta)d\theta = 1.0. \tag{4.20}$$

We further assume that the orientation distribution function is symmetric about $\theta = 0.0$. The probability of the agglomerate rotating in either direction should be identical, leading to the symmetric boundary condition

$$\frac{\partial P}{\partial\theta} = 0.0, \text{ at } \theta = 0. \tag{4.21}$$

The solution to Eq.(4.19) should give the limiting behavior discussed previously, namely a flat orientation distribution function for small Γ, and an asymptotic approach to a delta function as Γ tends to infinity.

4.4 The Solution of the Rotational Convective - Diffusive Equation

The rotational convective-diffusion Equation, (4.19), was solved numerically by the shooting method using the symbolic mathematics package, Mathematica. Numerical evaluation was not possible at $\theta = 0$ or $\theta = \pi$ since the cotangent in Eq.(4.19) tends to infinity at both these points. To perform the numerical solutions, points close to zero and to π were taken as the endpoints. The first derivative of the orientation distribution was set to zero at a value of θ close to zero, and the orientation distribution function value at this value was estimated. The solution was then integrated over the range from $\theta \simeq 0$ to $\theta \simeq \pi$ and the integrand compared to the expected value of 0.5. If the integral was not equal to 0.5 ± 0.005 then the estimation of orientation distribution function at θ close to zero was adjusted and the process repeated.

The value of the orientation distribution function near $\theta = 0$ was evaluated using an asymptotic expansion of the orientation distribution function. The solution to Eq.(4.19) for small values of Γ can be approximated by an expansion in Γ and functions that depend only on θ, i.e.,

$$P(\theta) = P_0(\theta) + \Gamma P_1(\theta) + \Gamma^2 P_2(\theta) + \cdots \Gamma P_n(\theta) + \cdots . \tag{4.22}$$

Applying the two boundary conditions, Eqs.(4.20) and (4.21) to the first term in the expansion leads to

$$\frac{\partial P_0(\theta = 0.0)}{\partial \theta} = 0.0, \text{and} \tag{4.23}$$

$$\int_{\theta=0.0}^{\theta=\pi} P_0 d\theta = 0.5. \tag{4.24}$$

The boundary conditions for the higher order terms become

$$\frac{\partial P_n(\theta = 0)}{\partial \theta} = 0, \text{ and} \tag{4.25}$$

$$\int_{\theta=0}^{\theta=\pi} P_n d\theta = 0. \tag{4.26}$$

Substituting the expansion (4.22) into Eq.(4.19) gives

$$\frac{\partial^2 P_0}{\partial\theta^2} + \cot\theta\frac{\partial P_0}{\partial\theta} + \sum_{n=1}^{\infty}\Gamma^n\left[\left(\frac{\partial^2 P_n}{\partial\theta^2} + \cot\theta\frac{\partial P_n}{\partial\theta}\right) - \left(\frac{\partial P_{n-1}}{\partial\theta} + P_{n-1}\cos\theta\right)\right] = 0. \quad (4.27)$$

The equations for each term of the expansion were solved sequentially beginning with the first term, $n = 0$, yielding

$$P(\theta) = \frac{1}{2\pi}\left(1 - \frac{\Gamma}{2}\cos\theta + \cdots\right) \quad (4.28)$$

for the first two terms. For small θ, the expansion yields,

$$\lim_{\theta\to 0} P(\theta) = \frac{1}{2\pi}\left(1 - \frac{\Gamma}{2}\right). \quad (4.29)$$

Using Eq.(4.29) as an initial estimate for P, the procedure described above produced numerical solutions to the rotational convective-diffusive equation. Figure (4.2) shows the calculated orientation distribution function, P(θ), as a function of θ.

$P(\theta)$ obtained behaves as expected at both limits of Γ. At small values of Γ, P(θ) $\sim$ $\frac{1}{2\pi}$ and is independent of θ, which indicates the agglomerate has no preferred orientation. Physically, the thermal energy dominates particle motion leading to a random orientation distribution. In the limit of large Γ, a delta function is obtained. As Γ increases the thermal forces become less significant, allowing the electric forces to dominate. This tends to align charged agglomerates with the electric field and skews the orientation distribution function. For $\Gamma \simeq 5.0$, the orientation distribution function is very close to zero for the entire range of $\theta = 0$ to $\theta = \pi/2$. Thus for $\Gamma > 5$ the agglomerates are highly aligned with the electric field.

4.5 Prediction of Orientation Effects

Using the orientation distribution function we now examine the influence of orientation on the measured electrical mobility. The electrical mobility of a particle is the ratio of the terminal migration velocity of the charged particle to the strength of the electric field,

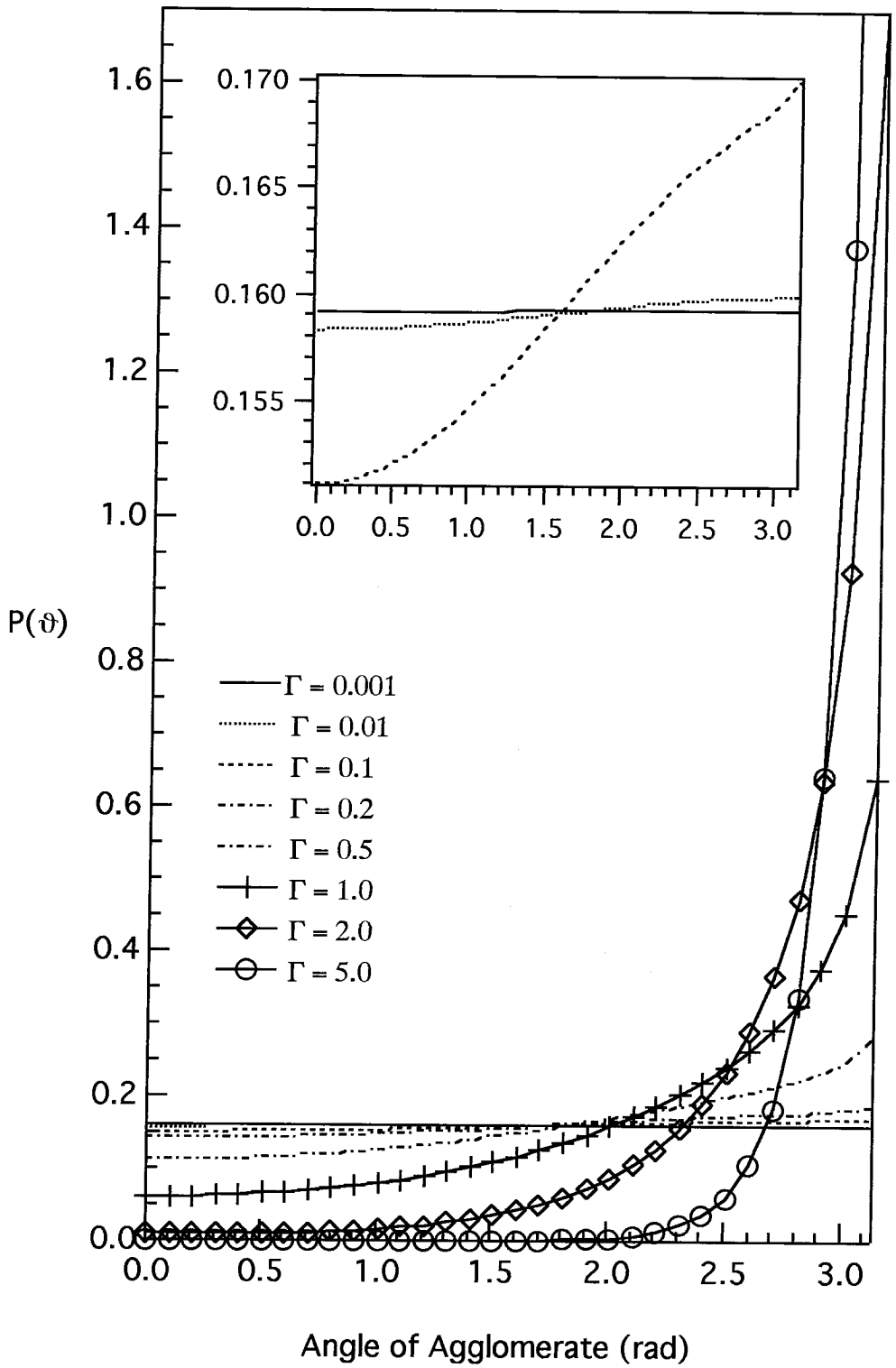

Figure 4.2: The orientation distribution function for an aerosol agglomerate with Γ varying from 0.001 to 2.0. The inset graph shows the behavior at small Γ in more detail.

which depends on the charge on the particle and the aerodynamic resistance to motion. The variation of the drag must be known to determine the orientation dependence of the mobility. Ellipsoids are the only non-spherically shaped particles that have an analytical solution for the drag force. To obtain an expression for the drag force on a linear chain aggregate, for which no analytical solution exists, Dahneke (1973a) extended the ellipsoid expression.

4.5.1 The Continuum Regime

The continuum regime resistance of a fluid on an ellipsoid of revolution with an equatorial semi axis of length a in purely viscous flow at low Reynolds numbers can be expressed as the product of the Stokes drag on a sphere of radius a and a so-called dynamic shape factor, χ', i.e.,

$$F = -6\pi\mu V a\chi', \tag{4.30}$$

where μ is the fluid viscosity, V is the relative velocity, and χ' is the so-called dynamic shape factor (Fuchs 1964). Since the viscous drag is a linear function of the velocity, the fluid resistance on the ellipsoid at any angle can be written as a sum of the components parallel and perpendicular to the polar axis, where the parallel component is

$$F_{\|} = -6\pi\mu V a\chi'_{\|}\cos\theta, \tag{4.31}$$

and the perpendicular component is

$$F_{\perp} = -6\pi\mu V a\chi'_{\perp}\sin\theta, \tag{4.32}$$

where θ is the angle that the primary axis of the particle makes to the direction of flow. Thus, the projection of the fluid resistance on the direction of motion of the particle is given by

$$F = -6\pi\mu V a(\chi'_{\|}\cos^2\theta + \chi'_{\perp}\sin^2\theta). \tag{4.33}$$

Averaging over all directions of the polar axis to give the resistance of the medium yields the drag force acting on randomly oriented particles undergoing rotational diffusion, i.e.,

$$\overline{F} = -6\pi\mu V a \left(\frac{1}{3}\chi'_{\parallel} + \frac{2}{3}\chi'_{\perp}\right) = -6\pi\mu V a \chi'. \tag{4.34}$$

Fuchs (1964) reported such shape factors for prolate and oblate ellipsoids, cylinders and other regular shaped particles.

Dynamic shape factors have been empirically determined for a variety of non-spherical particle (Fuchs 1964, Dahneke 1973a). Dahneke (1982) used the gravitational settling experimental data from Horvath (1974) to obtain continuum regime resistances for linear chains of up to 1000 spheres. The forces acting on aggregate particles are conveniently described in terms of a resistance coefficient that is based on the primary particle size, i.e., for continuum regime primary particles of radius, a_p

$$F^o = c^o \mu a_p V, \tag{4.35}$$

where V is the relative velocity, μ is the fluid viscosity.The orientation averaged dimensionless resistance coefficient can be expressed in terms of the resistance coefficents in the three primary directions,

$$\overline{c^o} = \frac{3}{c_x^{o-1} + c_y^{o-1} + c_z^{o-1}}. \tag{4.36}$$

The resistance to motion of particles with complex or unknown shapes is frequently described in terms of the size of a spherical particle that would experience the same drag force when moving at the same velocity,

$$F = 6\pi\mu V R_H, \tag{4.37}$$

where R_H is the so-called equivalent hydraulic radius of the particle. Rogak and Flagan (1990) showed that the hydraulic radius for fractal agglomerates of continuum regime spheres is related to the radius of gyration, R_g, and the fractal dimension through a

function of the number of primary particles that comprise the aggregate, i.e.,

$$\beta(N) = \frac{R_g}{R_H} \tag{4.38}$$

The radius of the smallest sphere that can contain the entire aggregate is

$$R_f = \sqrt{\frac{(D_f + 2)}{D_f}} R_g. \tag{4.39}$$

For a linear chain ($D_f = 1$), R_f is one-half of the chain length. For a flat aggregate with $D_f = 2$, R_f is the radius of the disk with the same projected area of the aggregate. For a three dimensional aggregate ($D_f = 3$), R_f is the radius of a sphere with the same volume.

4.5.2 Free Molecular and Transition Regimes

The dynamics of collisions of gas molecules are important for particles that are small compared to the mean-free path of the gas molecules. The collisions are often charcterized in terms of the fraction of diffuse reflections, α, in which the gas molecules leave the particle surface in random directions with a Maxwell-Boltzmann distribution of velocities corresponding to the particle surface temperature, and the fraction, $1 - \alpha$, that are reflected specularly. From the kinetic theory of gases, the free molecular resistances for a single sphere is

$$c_1^* = (\pi/3)(8 + \pi\alpha). \tag{4.40}$$

The oil drop experiment of Millikan suggested that $\alpha = 0/93$.

Dahneke and co-workers (Dahneke 1973b, 1973c, Chan and Dahneke 1981) have estimated the drag forces on free molecular and transition regime particles of a variety of shapes. Monte Carlo calculations were used to estimate the contribution to the drag of a linear chain agglomerate by two hemispheres touching at their poles. Combining this "basic chain unit" (bcu) with the two hemispherical end-caps of a chain provides an estimate of the free molecular drag on a linear chain agglomerate (Chan and Dahneke,

1981), i.e.,

$$c_N^* = (N-1)c_{bcu}^* + c_1^*, \tag{4.41}$$

where c_1^* is the resistance of a single primary particle, and is used to account for the two end hemispheres of the chain. The free molecular resistance is

$$c^* = c(Kn)Kn = \frac{2F(Kn)Kn}{\mu dV} \tag{4.42}$$

Dahneke (1973c) proposed an adjusted sphere model to account for non-continuum effects in linear agglomerate particles. The slip correction factor which is the ratio of the actual drag force on the linear chain divided by the continuum drag force, and can also be expressed as the ratio of the resistances,

$$C_s(Kn) = \frac{F(Kn)}{F^o} = \frac{c^o}{c(Kn)}. \tag{4.43}$$

In the free molecular limit, where $Kn \to \infty$, substitution of Eq.(4.42) leads to

$$KnC_s(Kn) = \frac{c^o}{c^*} = \text{constant}. \tag{4.44}$$

The continuum and free molecular resistances are known and therefore allow evaluation of the constant. To obtain resistances in the transition regime, Dahneke proposed equating the slip correction factor of the linear chain with that of an adjusted sphere

$$C_{sa}(Kn_a) = C_s(Kn). \tag{4.45}$$

Substitution of a slip correction factor for a sphere, such as Eq.(4.5), in the free molecular limit allows an adjusted sphere radius to be evaluated. The two correction factors will also be equal in the continuum limit, since as $Kn \to 0$ the correction factors are unity. The adjusted sphere radius is then used in the slip correction factor for the sphere to obtain the resistance on the linear chain in the transition regime.

Rogak et al. (1993) used the ratio between the minimum and maximum mobility diameters, $\psi = d_{max}/d_{min}$, to characterize the influence of orientation. In the free molecular regime, $\psi = 1.56$ for prolate spheroids and $\psi = 1.31$ for long chains.

These approaches use an average resistance, but for values of Γ greater than 0.1,

the agglomerate will not sample all of the orientations equally. Assuming that the charge is localized near the end of the long axis of the particle, this will lead to a larger electrical mobility for these particles. The orientation dependent electrical mobility is defined from equations(4.3)and (4.5) as

$$Z(\theta) = \frac{v_e(\theta)}{E}. \tag{4.46}$$

The mean electrical mobility, $\overline{Z_e}$, is determined by integrating the product of the orientation distribution function, P(θ), and an orientation-dependent mobility, i.e.,

$$\overline{Z_e} = \int Z(\theta)P(\theta)d\theta. \tag{4.47}$$

To probe alignment effects, the orientation dependent mobility can be normalized by the electrical mobility for the same particle in the limit of $\Gamma \rightarrow 0$, i.e.,

$$\Phi = \frac{\overline{Z_e}}{\overline{Z_{random}}} \tag{4.48}$$

where

$$\overline{Z}_{random} = \int_{\theta=0}^{\theta=\pi} Z(\theta)P_{\Gamma=0}(\theta)d\theta. \tag{4.49}$$

4.6 Example: Orientation of a Linear Chain Agglomerate

The linear chain agglomerate can be approximated as a finite cylinder (Eisner and Gallily,1980) or by considering the individual primary particles as spheres (Dahneke, 1982). We consider a linear chain that is composed of equal sized primary particles. The problem of non-linear chains has been dealt with by Kasper (1982) who used a coefficient to calculate the aerodynamic diameter of a linear chain with shape irregularities. Kasper found that nonlinear aggregate shapes tend to increase the drag force and reduce the mobility.

To obtain the orientation dependent drag force we use the adjusted sphere approach of Dahneke (1973c). The correction factor is the ratio of continuum drag force to

the free molecular drag force. From Eq.s (4.33) and (4.35), the continuum drag force is

$$F^o = \frac{c^o \mu d V}{2} = \frac{\mu d V}{2}\left(c_{\parallel}^o \cos^2\theta + c_{\perp}^o \sin^2\theta\right). \tag{4.50}$$

Continuum regime perpendicular and parallel resistances for linear chains consisting of N primary particles were obtained from Dahneke (1982) and are given in Table (4.1)

N	$c_{\parallel}^o$	$c_{\perp}^o$
3	28.9	34.4
5	37.4	47.5
10	56.1	76.8
20	89.0	129
50	174	264
100	299	466
200	523	834

Table 4.1: Values of the continuum perpendicular and parallel resistances for chains of varying N

The free molecular drag force can be expressed by Eq.s (4.33) and (4.42) as

$$F^* = \frac{c^* \mu d V}{2Kn} = \frac{\mu d V}{2Kn}\left(c_{\parallel}^* \cos^2\theta + c_{\perp}^* \sin^2\theta\right), \tag{4.51}$$

where $Kn = \frac{2\lambda}{d}$, and d is the diameter of the primary particles in the linear chain. The free molecular resistances were obtained using Eq.(4.42) and can be found in Table(4.2).

N	$c_{\parallel}^*$	$c_{\perp}^*$
3	24.68	34.14
5	37.91	56.84
10	71.02	113.6
20	137.2	227.1
50	335.8	567.6
100	666.8	1135
200	1329	2270

Table 4.2: Values of the free molecular perpendicular and parallel resistances for chains of varying N

The orientation correction factor then becomes

$$C(\theta) = \frac{F^o}{F^*} = Kn\frac{\left(c_{\parallel}^o \cos^2\theta + c_{\perp}^o \sin^2\theta\right)}{\left(c_{\parallel}^* \cos^2\theta + c_{\perp}^* \sin^2\theta\right)}. \tag{4.52}$$

The correction factor, $C(\theta)$, is then equated to the Cunningham slip correction factor, following the adjusted sphere model of Dahneke (1973c).

$$C(\theta) = 1 + Kn_a\left(1.257 + 0.4\exp\left(\frac{-1.1}{Kn_a}\right)\right), \tag{4.53}$$

where Kn_a is the Knudsen number based on the adjusted sphere diameter (Eq.4.43). For the sphere to approximate the behavior of the linear chain, the sphere must have the same drag in the continuum and free molecular regimes as the linear chain.

In the continuum regime ($\mathrm{Kn} \to 0$), the Cunningham slip correction tends to one, leading to the trivial solution for the correction factor of the linear chain. In the free molecular regime, as the Knudsen number tends to infinity, Eq.(4.53) can be simplified to

$$C(\theta) = \frac{\mathrm{Kn}\ c^o(\theta)}{c^*(\theta)} = Cc(\mathrm{Kn}_a) = 1.657\mathrm{Kn}_a. \tag{4.54}$$

The adjusted sphere diameter can now be expressed as

$$D_a = \frac{2\lambda}{\mathrm{Kn}_a} = \frac{2\lambda\,(1.257 + 0.4)\,c^*(\theta)}{\mathrm{Kn}c^0(\theta)}. \tag{4.55}$$

The orientation dependent electrical mobility of a linear chain agglomerate at any angle, can be written as

$$B_e(\theta) = \frac{qC(\theta)}{3\pi\mu D_a}. \tag{4.56}$$

The electrical mobility at orientations parallel and perpendicular to the electric field are presented in Figure (4.3). Increasing the size of the primary particle or increasing the number of particles in the chain lowers the electrical mobility. As the number of primary particles or the primary particle diameter increases the difference between the parallel and perpendicular electrical mobilities decreases. For instance for a chain of five particles of 5nm diameter has a parallel mobility 38% higher than the perpendicular mobility while for a chain of 1000 particle of 200nm diameter the difference is only 4%.

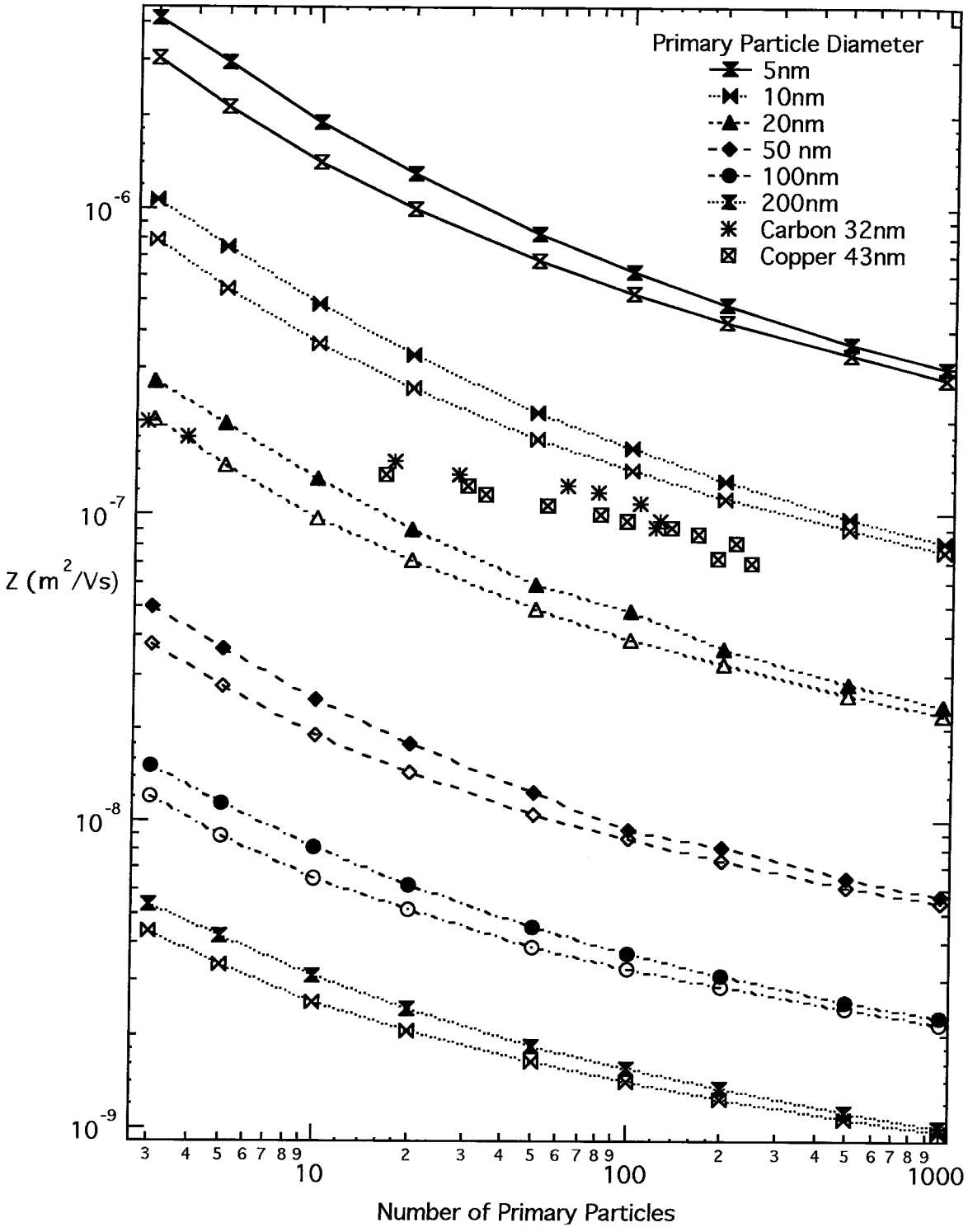

Figure 4.3: The parallel (open symbols) and perpendicular (closed symbols) electrical mobilities of linear chains of uniform primary particles.

The orientationally dependent electrical mobility is symmetric about $\theta = \pi/2$. The electrical mobility at $\theta = \pi/2$ corresponds to the perpendicular alignment and the parallel alignment is seen at $\theta = 0.0$ and $\theta = \pi$. As the particle rotates from $\theta = 0$ towards $\theta = \pi/2$ the particle's drag force increases, lowering it's electrical mobility. As the particle rotates from $\theta = \pi/2$ towards $\theta = \pi$ the drag force decreases with a corresponding increase in the electrical mobility. This leads to a flattening of the electrical mobility profile as the number of particles in the chain increases, as shown in Figure(4.4).

The electrical mobility of carbon aggregates from a benzene-kerosene flame and of copper oxide aggregates from an exploding wire were measured by Vomela and Whitby (1967). The copper oxide aggregates had a primary particle diameter of 43nm with a geometric standard deviation of 1.3 while the carbon aggregates had primary particle diameters of 32nm with a geometric standard deviation of 1.44. The experimental electrical mobilities are considerably higher than predicted. The micrographs in the Vomela and Whitby paper show the carbon and copper aggregates to be more densely packed than a chain, thus lowering the projected area that the agglomerates present to fluid flow and increasing the electrical mobility. The observations for carbon chains with 3 and 4 primary particles agree well with the theory. At small numbers of primary particles the aggregates must be chain-like and the effect of primary particles shadowing one another is small.

In order to determine the orientation averaged electrical mobility from Eq.(4.47), the orientation distribution function, P(θ), is required at an appropriate value of Γ. To facilitate comparison with experimental observations, the electrical mobility analyzer and the flow conditions in the analyzer are chosen to be as standard and commonplace as possible. The electrical mobility analyser used is a TSI 3077 cylindrical DMA (TSI, 1990; Knutson and Whitby,1975a, 1975b). A 10:1 ratio of the sheath flowrate, Q_{sh}, to the excess flowrate is assumed. Two sheath flowrates will be examined, 10.0 and 3.0 liters per minute. The low sheath flowrate allows large particle sizes to be measured, up to 890 nm. The 10 liters per minute flowrate allows smaller sizes to be measured, with a maximum size of 335nm.

The voltage required to classify particles with an orientation-averaged adjusted

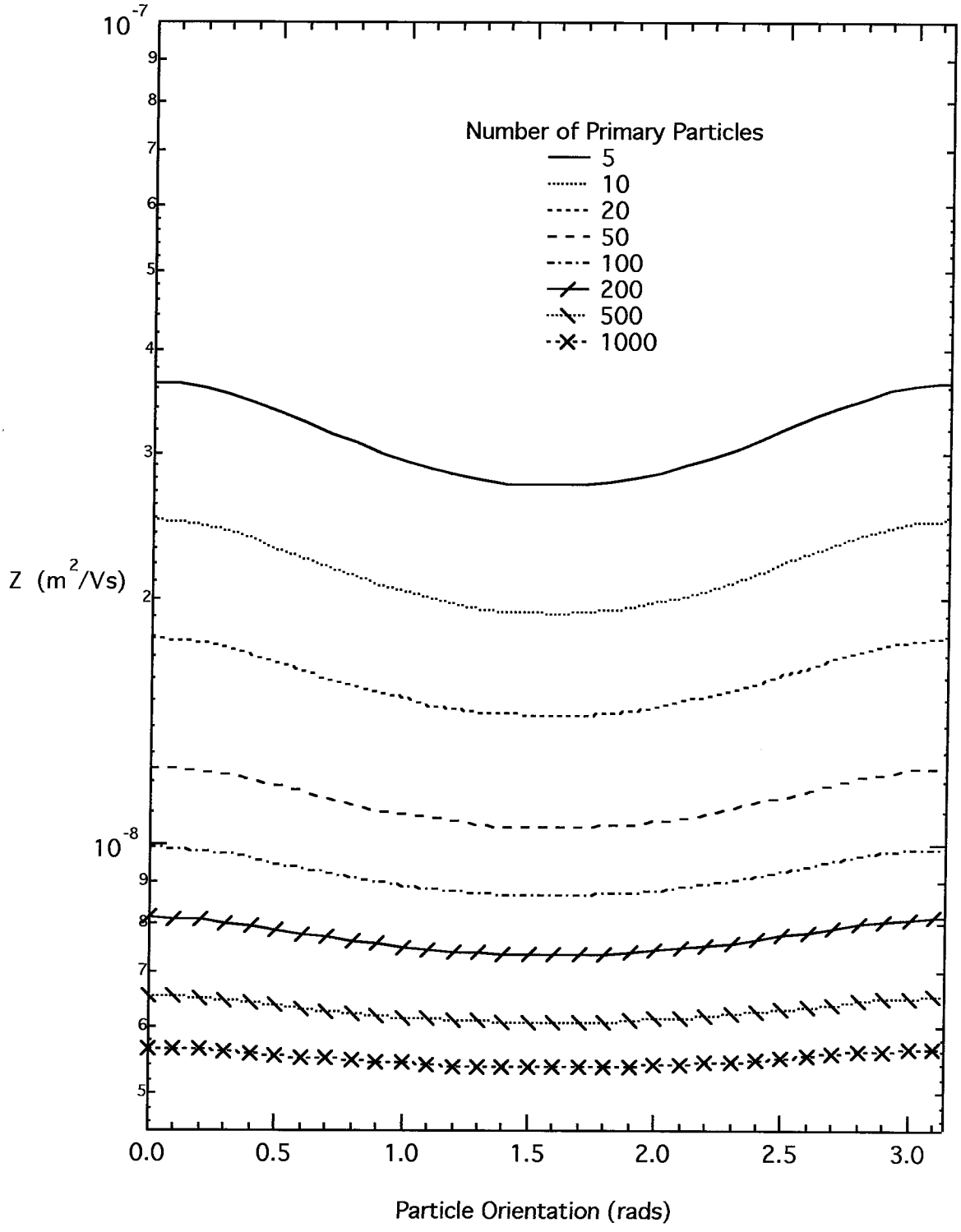

Figure 4.4: The orientational dependent electrical mobility for linear chains of 50nm primary particles with number varying from 3 to 1000.

sphere diameter of D_a, is

$$V = \frac{3\mu D_a Q_{sh} \ln\left(\frac{r_2}{r_1}\right)}{C_c\left(Kn_a\right) 2q}, \tag{4.57}$$

where $r_1 = 0.937$cm and $r_2 = 1.958$cm are the radii of the inner and outer cylinders of the DMA, respectively. The radial electric field in the DMA is (Knutson and Whitby, 1975a).

$$E(r) = \frac{V}{r \ln\left(\frac{r_1}{r_2}\right)}. \tag{4.58}$$

The electric field at the midpoint between the two electrodes was used to calculate the Γ factor. With the Γ factor, the orientation distribution function was calculated in the manner described previously and the electrical mobility ratio, Φ evaluated for linear chains of varying length and primary particle diameter for both the low and high sheath flowrate cases. The results are presented in Figures (4.5) and (4.6). As the number of primary particles increases Φ increases to a peak and then declines. From this point onward any increase in the number of primary particles, or chain length, does not increase the mobility ratio. The chain length at which this peak occurs decreases and the peak value of Φ increases as the primary particle diameter increases. In the high flowrate case only one mobility ratio is reported for chains with primary particles of 200nm diameter. Chains with more than 3 primary particles would require more than 10000 volts to be applied across the DMA. This is not possible in the TSI 3071 DMA.

To understand the trends, the orientational electrical mobility needs to be taken into account. As the chain length increases, the difference between the drag force at perpendicular and parallel orientations decreases. In the continuum regime limit, the drag force is just proportional to the longest dimension of the particle.

The alignment parameter, Γ, is directly proportional to the voltage applied across the DMA. The numerical solutions to the convective-diffusive equation predict that strong alignment requires a value of Γ of order 5 or larger. At the high sheath flowrate the peaks occur at Γ values varying from 4.6 to 10.3, and at the low flowrate the peak occurs at Γ varying from 4.8 to 15.7. While Γ is difficult to evaluate precisely due to uncertainties of charge distribution and morphology, it is clear that the highest mobility ratio of each chain occurs at a position where the alignment force is strong but the chain is not yet long enough to be in the continuum regime.

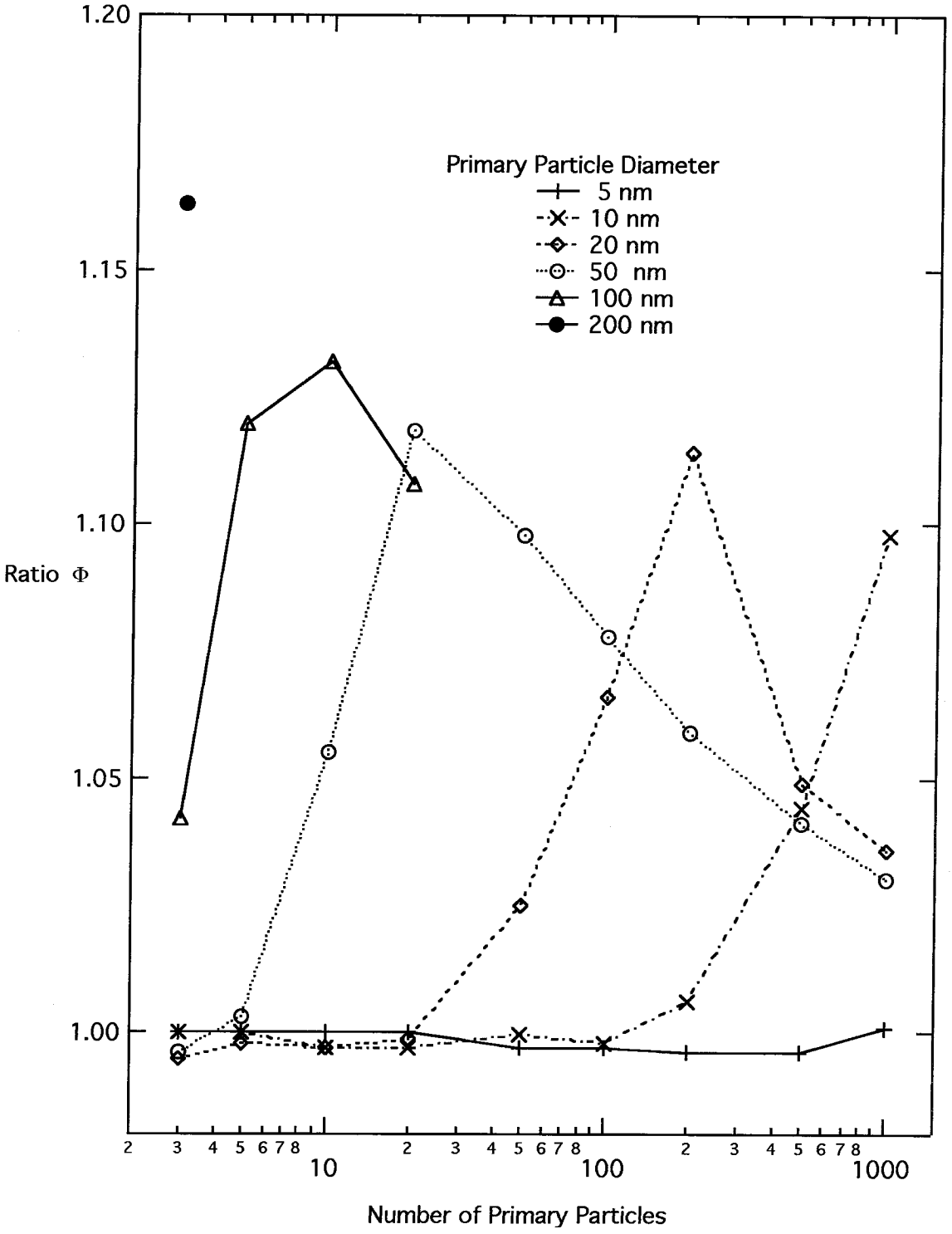

Figure 4.5: The Mobility Ratio of linear chain agglomerates with varying chain length and primary particle diameters for a sheath flow of 10 litres per minute.

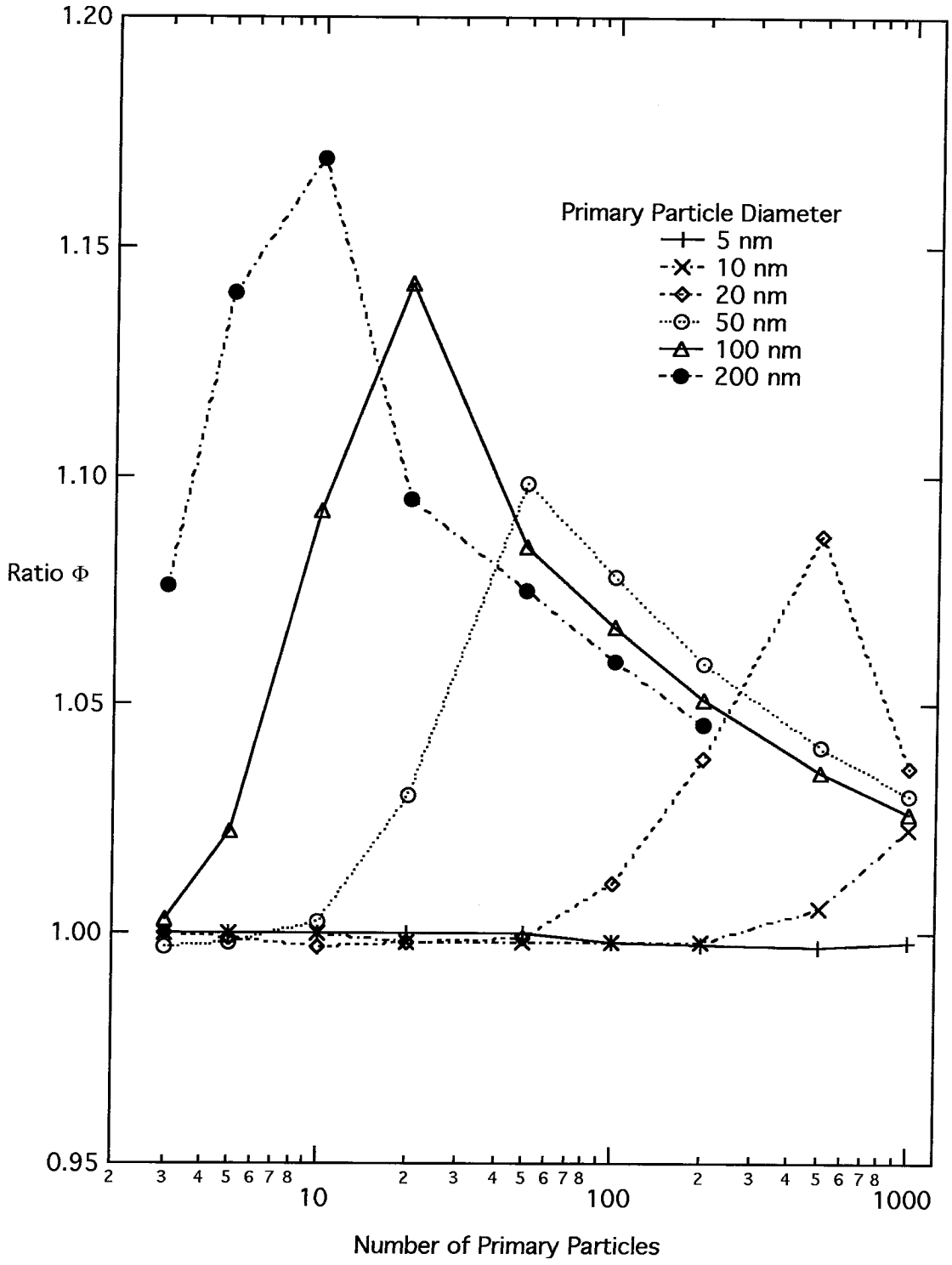

Figure 4.6: The Mobility Ratio of linear chain agglomerates with varying chain length and primary particle diameters for a sheath flow of 3 litres per minute.

The present analysis has assumed that the rotational relaxation time of the chains is much smaller than the time the chains are exposed to the electric field in the DMA. The rotational relaxation time is the inverse of the rotational diffusivity. Doi and Edwards (1986) give the rotational diffusivity, D_r of a chain of N beads of diameter b as

$$D_r = \frac{3kT \ln(L/2b)}{\pi \mu L^3} \tag{4.59}$$

where $L = Nb$ is the length of the chain. This expression is only valid for chains in the continuum regime, so only chains with $L > 1\mu$m will be considered. The shorter the chain, the larger the rotational diffusivity so if the rotational relaxation time is neglible compared to the exposure time for the 1 μm case it will be neglible for all shorter chains. As in the mobility ratio calculations, chains of varying primary particle diameter will be considered for the high and low flow rates. The rotational relaxation time is defined to be small if it is less than one tenth the exposure time. This corresponds to the rotational diffusivities having to be greater than 4.5 s^{-1} and 1.34 s^{-1} for the high and low flow rate cases respectively.

The theoretical curves for primary particle diameters of 5nm to 500nm can be seen in Figure (4.7). As the primary particle diameter and number of primary particles in the chain increase, the rotational diffusivity decreases. For the low flowrate case, all chains with a length of 5 μm or less can be considered to satisfy the constraint that the rotational relaxation time is much smaller than the exposure time to the flow in the DMA. However, in Figure (4.6), some chains are longer than 5 μm. In these cases the orientation distribution of the chains exiting the DMA will not be independent of the entrance orientation distribution. The reported mobility ratios are therefore theoretical maximums which may not be observed experimentally.

4.7 Comparison to Experimental Results

The theory described in this paper does not specify the type of electrical mobility analyzer that has to be used. The Γ factor is proportional to the electric field applied in the analyzer, but not dependent on any other geometrical parameter. The convective-diffusive

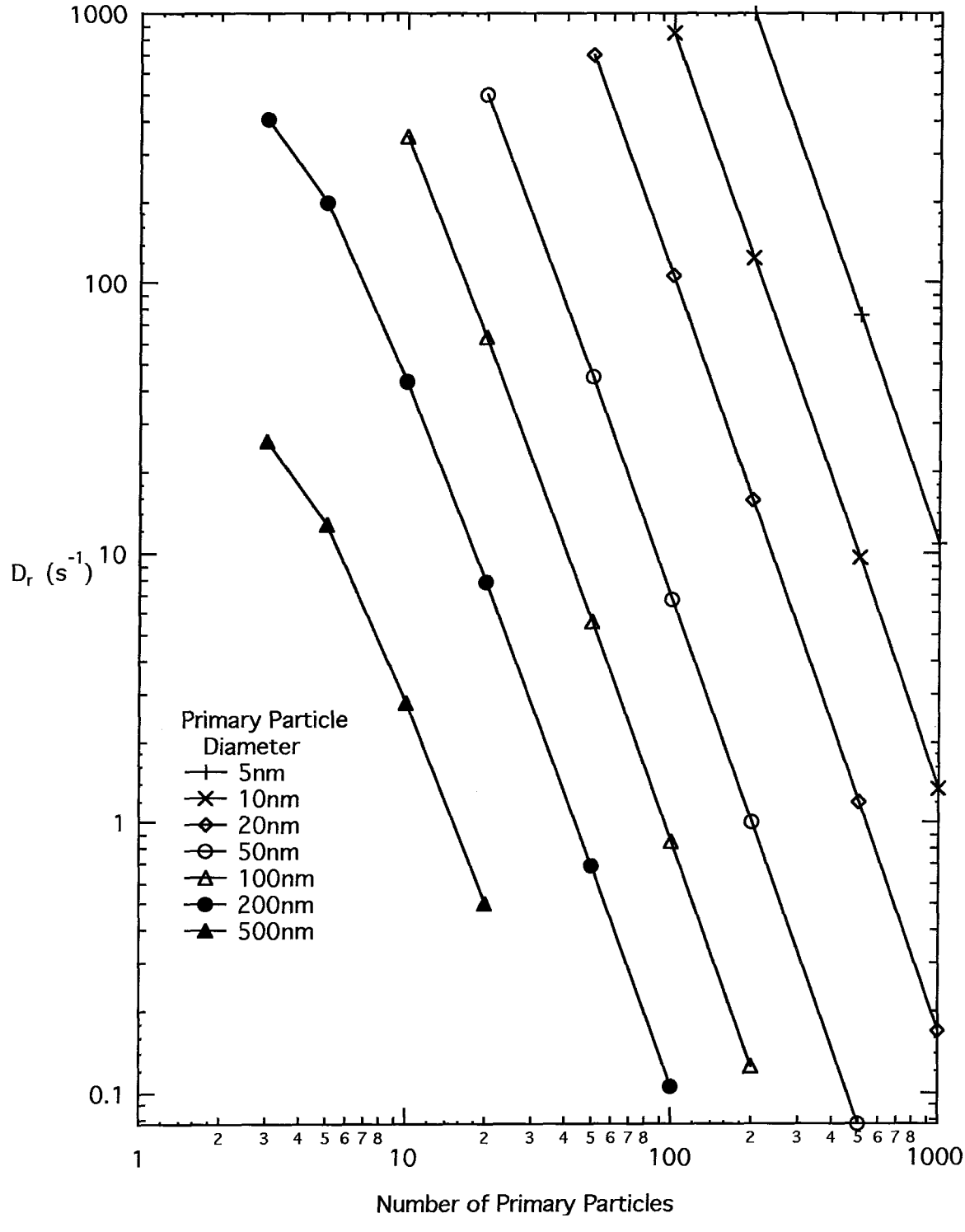

Figure 4.7: The rotational diffusivities of linear chain aggregates with varying number and primary particle diameter.

equation should apply to any electrical mobility analyzer. To illustrate the general applicability of the theory, previously published experimental results from a parallel plate capacitor, and from cylindrical DMAs will be examined.

Horvath (1979) measured the sedimentation velocities of doublets of 1.099 μm latex particles in the electric field of a parallel plate capacitor. Horvath states that complete orientation was attained at an electric field of 150,000 V m^{-1} or more. For the latex particle doublets under this field, the Γ is

$$\Gamma = \frac{eER_c}{kT} = \frac{1.601 \times 10^{-19} \times 150,000 \times 1 \times 10^{-6}}{1.38 \times 10^{-23} \times 298} = 5.84 \tag{4.60}$$

The temperature in Horvaths experiments was assumed to be 298K. The Γ value of 5.84 is large enought that significant orientation is predicted by our model.

Measurements of the drag force on α-Fe_2O_3 chain aggregates suggested that the chains were oriented along the field lines (Wen and Kasper, 1984c). To evaluate Γ for the DMAs used in these experiments, the characteristic field strength was taken to be that at the midpoint between the concentric cylinders. Wen and Kasper report the voltage across the DMA, and number of primary particles in the chain for many differing primary particle sizes. Chains of 45nm primary particle diameter of 19 and 45 primary particles and a chain made up of 32 100nm diameter primary particles were classified at voltages of 3, 6 and 10 kV respectively. Assuming the particle is singly charged with the charge located at the end of the chain, i.e., R_c is half the length of the chain, the calculated Γ values were 4.7, 22.4 and 58.1 respectively. In each case, strong orientation is expected.

Lunden(1995) studied the structural changes of mobility classified particles during sintering. The change in mobility diameter with sintering time can be seen in Figure (4.8). Initially the primary particles sinter together, forming necks of increasing width and decreasing the agglomerate's overall length. The mobility diameter decreases (mobility increases) as might be expected for such rearrangement. This trend is followed for sintering times below 3 seconds. One might expect the agglomerate mobility to continue to increase continuosly toward that of a dense sphere with volume equal to that of the initial aggregate. Instead the electrical mobility diameter increases at a sintering time of approximately 4 seconds. The increase has been attributed to a rearrangement of the primary particles to a preferred grain boundary orientations. This rearrangement is

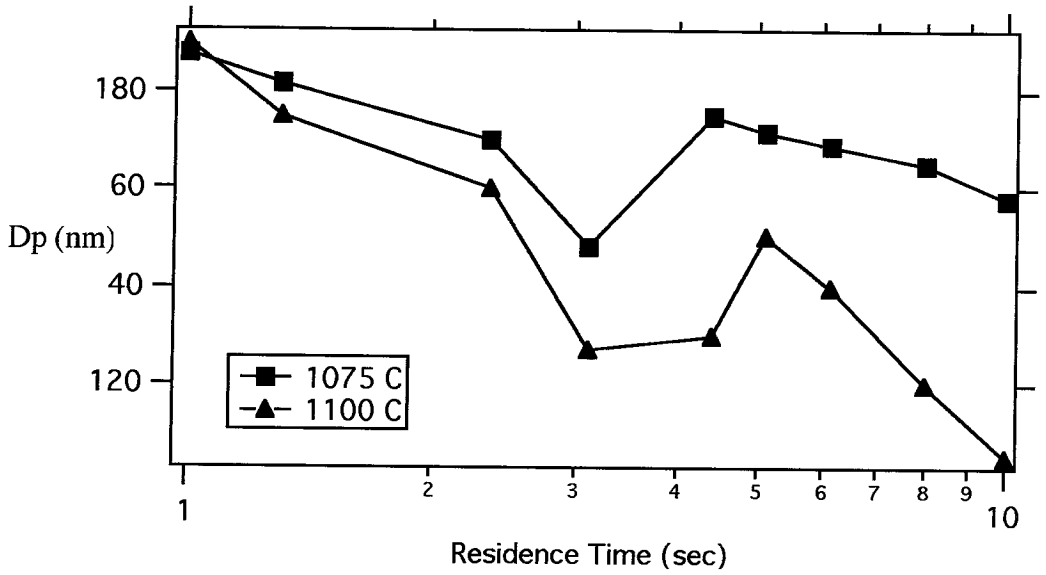

Figure 4.8: The electrical mobility diameter of silicon agglomerates with varying sintering times. Reprinted with permission from Lunden (1995)

shown in Figure (4.9). To explain the increase in electrical mobility, the TEM images for the 1100^{o}C case were examined. A typical silicon aggregate was a chain of 5 primary particles with a diameter of 75nm. The particles were sized by a TSI 3071 DMA, with a sheath flow of 7.0 liters per minute and a monodisperse flow of 1.58 liters per minute. The charge was assumed to be carried on the end of the agglomerate and so R_c was half the length of the chain. Using this data, the Γ factor for the aggregates described above is 1.8.

With the Γ defined a similar analysis to the example of a linear chain aggregate was carried out. The orientationally averaged electric mobility for the typical chain was 1.71 $\times 10^8$ m^2/Vs. The electrical mobility of the chain oriented perpendicular to the flow direction was 1.40 $\times 10^8$ m^2/Vs. The 1100^{o}C case shows the mobility to initially decrease with increasing sintering time, from to 130nm and then increase to 150nm before declining again. The electrical mobility of a 130nm diameter sphere with is 1.73 $\times 10^8$ m^2/Vs and the mobility of a 150nm diameter sphere is 1.46 $\times 10^8$ m^2/Vs. These mobilities agree well with the theoretical mobilities obtained for the chain.

Thus, it appears that the aggregates start out as a linear chain with the primary particles sintering together but, after about 3 seconds the primary particles begin to

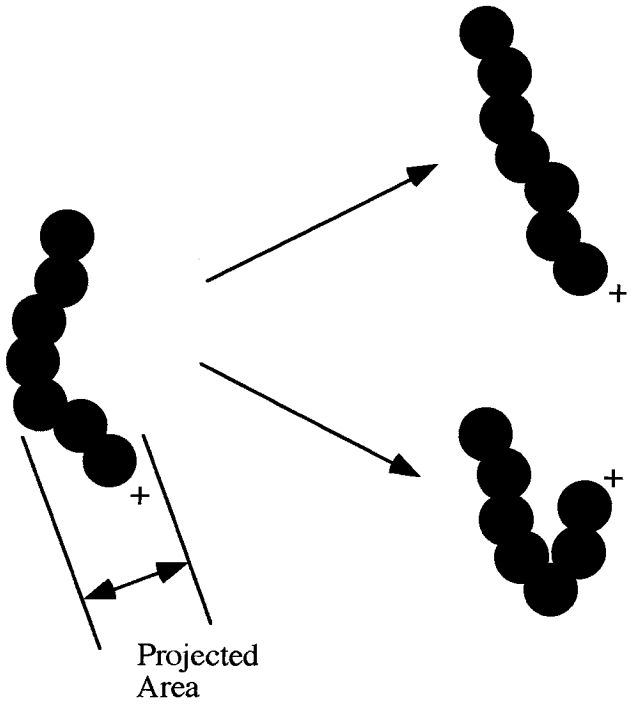

Figure 4.9: The rearrangement of a linear chain upon sintering, with the primary particles rotating to a preferred grain boundary orientation. Reprinted with permission from Lunden (1995)

rotate to preferred grain boundary orientations, distorting the linear chain. A bent chain is not able to align as efficiently as a straight chain. The mobility of the aggregate decreases to almost that of a linear chain aligned perpendicularly to the flow.

4.8 Summary

The convective-diffusive equation was used to analyze the orientation of charged aerosol agglomerates in an electric field. The orientation was found to be dependent on a single parameter Γ, which is the ratio of the Coulombic to the thermal energies. Numerical solutions were obtained for the orientation distribution function for a range of Γ. For small Γ the orientation probability was uniform over the entire range of θ, indicating that the rotational diffusion overwhelms any tendency for alignment. In the limit of large Γ, the orientation distribution function approaches a delta function at $\theta = \pi$. This limit corresponds to all the agglomerates being aligned with the electric field. Significant alignment was found to occur at $\Gamma \simeq 5.0$, when no agglomerates had an alignment between 0.0 and $\pi/2$.

An electrical mobility analyzer classifies according to electrical mobility. An aligned agglomerate may present a smaller cross section to flow than an agglomerate undergoing random rotations. The magnitude of this effect was quantified for a linear chain aggregate in a cylindrical DMA at two different flow rates. The criteria used was the ratio of the electrical mobility of chains with orientations according to the orientation distribution function divided by the electrical mobility of randomly oriented chains. In each case, a maximum was seen in the electrical mobility ratio. As the primary particle decreased the maximum occurred at larger numbers of primary particles in the chain, with the maximums decreasing in magnitude with decreasing primary particle diameter.

These trends can be explained by an examination by noting the dependence of the electric field applied across a DMA to the particle size. Small chains are collected at low voltages, giving small values of Γ. As the number of primary particles increases, the DMA voltage to collect them increases accordingly. This leads to an increase in Γ and orientation effects. Increasing the number of primary particles in the chain leads to the chain being in the continuum limit where the drag force is dependent solely on the

longest length of the chain, irrespective of orientation. This causes the decrease in the mobility ratio.

The theory was compared to experimental data. The condition that resulted in particle alignment in several previous experimental studies have been shown to be consistent with the present model, i.e., alignment occurs for $\Gamma \geq 5$.

4.9 Acknowledgements

The author wishes to thank; Dr. Melissa Lunden for reviewing the work and her considerable input into the experimental comparison section and Mr. Douglas Varela for his advice in the mathematical aspects of this paper. Funding support was given by NSF under grant CTS-9113193 and from the International Fine Particle Research Institute under grant FRR 20-07.

Bibliography

Alexander, A. and Johnson, P. (1949). *Colloid Science, Volume I.* Oxford University Press.

Chan, P. and Dahneke, B. (1981). Free-molecule drag on straight chains of uniform spheres. *Journal of Applied Physics*, 52(5):3106–3110.

Dahneke, B. (1973a). Slip correction factors for nonspherical bodies - I Introduction and continuum flow. *Journal of Aerosol Science*, 4:139–145.

Dahneke, B. (1973b). Slip correction factors for nonspherical bodies - III The form of the general law. *Journal of Aerosol Science*, 4:163–170.

Dahneke, B. (1982). Viscous resistance of straight-chain aggregates of uniform spheres. *Aerosol Science and Technology*, 1:179–185.

Doi, M. and Edwards, S. (1986). *Theory of Polymer Dynamics.* Oxford Science.

Eisner, A. and Gallily, I. (1981). On the stochastic nature of the motion of non-spherical aerosol particles, iii. The rotational diffusion diadic and applications. *Journal of Colloid and Interface Science*, 81(1):214–233.

Flagan, R. and Seinfeld, J. H. (1988). *Fundamentals of Air Pollution Engineering.* Prentice Hall, New Jersey 07632.

Fuchs, N. (1964). *The Mechanics of Aerosols.* Pergamon Press, New York.

Horvath, H. (1979). Method for the determination of dynamic shape factors of sphere aggregates by measuring the sedimentation velocity in a capacitor. *Journal of Aerosol Science*, 10:309–315.

Kasper, G. (1982). Dynamics and measurement of smokes. ii the aerodynamic diameter of chain aggregates in the transition regime. *Aerosol Science and Technology*, 1(1):201–215.

Kasper, G. and Shaw, D. (1983). Comparative size distribution measurements on chain aggregates. *Aerosol Science and Technology*, 2:369–381.

Knutson, E. and Whitby, K. (1975a). Accurate measurement of aerosol electric mobility moments. *Journal of Aerosol Science*, 6:453–460.

Knutson, E. and Whitby, K. (1975b). Aerosol classification by electric mobility: Apparatus, theory and applications. *Journal of Aerosol Science*, 6:443–451.

Krushkal, E. and Gallily, I. (1984). On the orientation distribution function of nonspherical aerosol particles in a general shear flow. *Journal of Colloid and Interface Science*, 99:141–152.

Lunden, M. (1995). *Ph.D. Dissertation.* California Institute of Technology.

McQuarrie, D. (1976). *Statistical Mechanics.* Harper Collins Publishers.

Millikan, R. (1923). Coefficients of slip in Gases and the law of reflection of molecules from the surfaces of Solids and Liquids. *Physical Review*, 21:217–238.

Rogak, S., Flagan, R., and Nguyen, H. (1993). The mobility and structure of aerosol agglomerates. *Aerosol Science and Technology*, 18:25–47.

Seinfeld, J. H. (1986). *Atmospheric Chemistry and Physics of Air Pollution.* John Wiley and Sons, New York.

T.S.I. Incorporated (1990). *Model 3071 Electrostatic Classifier Instruction Manual.* TSI Incorporated, St. Paul.

Van de Ven, T. (1989). *Colloidal Hydrodynamics.* Academic Press, New York.

Wen, H. and Kasper, G. (1984). Dynamics and measurement of smokes. III drag and orientation of chain aggregates in an electrical mobility spectrometer. *Aerosol Science and Technology*, pages 397–403.

Chapter 5 Conclusions

Hi motus animorum atque haec certamina tanta
Pulveris exigui lactu compressa quiescent.

These movements of souls and these contests, however great,
having been contained by the throwing of a little dust,
will be quiet.

Publius Vergilius Maro (Virgil)
Georgics no.4, l.176

5.1 Summary

The Brownian coagulation of spherical particles has been studied extensively but less is known about the coagulation of aerosol agglomerates. Although models of the collision frequency functions have been presented, they have not previously been experimentally validated. Most experimental investigations of the dynamics of aerosol agglomerates, have been performed in complex systems in which many processes proceed simultaneously. To isolate coagulation from competing effects, an experiment was devised to measure the coagulation coefficients of finely structured titania agglomerates. The agglomerates had a primary particle diameter of 6nm on average and the overall mobility diameters varied from 20nm to 250 nm. The experimentally determined coagulation coefficients agreed reasonably well with the predictions of Rogak anf Flagan.

Electrical image forces and Lifshitz-van der Waals forces have been shown to enhance Brownian coagulation for small particles. The experiments carried out here do not show a significant enhancement, as the smallest mobility diameter that could be measured was 20nm. The agglomerates do show an enhancement over the Fuchs theory for spheres, but this enhancement is predicted by the Rogak and Flagan theory. An interesting extension of the experiments would be to measure the coagulation coefficient of particles below 20nm in diameter. The cylindrical DMAs used in this study would have to be replaced with DMAs that are optimized for measurements of the smaller particles. In particular, higher transmission and charging efficiencies would be needed to make such measurements possible.

In order to analyze the coagulation experiments, the steady-state bipolar diffusion charge distribution of aerosol agglomerates was also studied. The experimental charge distribution was obtained from a tandem DMA apparatus and compared to the extended Fuchs theory. The agglomerates were found to carry more charges than a spherical particle of the same mobility diameter. The increase in charge was attributed to the agglomerate being able to position multiple charges on itself at greater distances than the diameter of a mobility equivalent sphere. Rotation of the agglomerates could also increase the collision probability with the ions.

The extended Fuchs theory is strongly dependent on the ion properties used. No

measurements of the ion properties or the relative humidity were carried out and so the ion properties were taken from Hussin et al. (1983). The charge equivalent diameter of the agglomerates was also calculated and found to approximately equal to 1.25. This value is structure specific and should change with fractal dimension.

Concern over possible experimental biases due to alignment of the particles with the electric field in the mobility classifier led to a theoretical investigation of agglomerate particle alignment. The tendency of a particle to align with the imposed field can be expressed in terms of the dimensionless ratio of the Coulombic to the thermal energies, Γ. For small Γ, the particle Brownian rotation dominates so there is no preferred orientation. For large Γ, the particle is strongly influenced by the Coulombic force and aligns in the electric field. The orientation distribution function becomes a delta function as $\Gamma \rightarrow \infty$.

A linear chain aggregate was used to develop the orientation theory. The electrical mobility ratio of the linear chain aggregate was found to have a maximum. As the chain length increases, the difference between the drag force at perpendicular and parallel orientations, decreases. The upper limit for this is in the continuum limit, where Stokes drag is dependent on the longest dimension, regardless of orientation. The Γ factor is directly proportional to the voltage applied across the DMA. So the maximum occurs where the alignment force is strong but the chain is too short to be in the continuum regime. Orientational effects have been seen in a number of experimental studies under conditions that are consistent with the present predictions.

The electrical mobility analyzers have become the workhorse of the aerosols field. The sizing of an aerosol agglomerate by such an analyzer is not a trivial task. Care needs to be taken in each stage of the inversion of the size distribution. To be exactly sure of the particles that are being sampled, a second sampling apparatus should be used. Electron microscopy analysis allows the particle structure to be determined. Once the particle structure is known the size distribution data can be inverted and the DMA can be used with confidence.

Appendix A Calibration of the Caltech Cylindrical DMA

A.1 Introduction

The differential mobility analyzer (DMA) is an instrument that uses the balance of drag and electrostatic forces to classify particles. The aerosol particles are introduced at the outer edge of two concentric cylinders. The particles experience a radial attraction (or repulsion depending on the charge) towards the central cylinder. There is a narrow slot in the central cylinder and a sample flow is collected here. Only particles with a narrow range of electrical mobility will be collected.

The DMA can be operated in two ways to obtain a size distribution. The first method is to set a voltage on the center rod, wait for the system to stabilise and then take a measurement of the number concentration. This step is repeated until all the sizes of interest have been counted. This method is time consuming and can take ten minutes to obtain enough data points to fully describe the size distribution.

The second method is to continuously alter the voltage that is applied between the cylinders. This is the scanning mode of operation and a DMA using scanning mode is sometimes called a Scanning Electrical Mobility Spectrometer (SEMS). The major advantage of this over the stepping mode is the time to take a distribution can be reduced to one minute. This allows the monitoring of distributions that change rapidly with time, such as the homogeneous nucleation of particles. The inversion of the data is not as straightforward as for the stepping mode but it can still be done easily by a personal computer. The derivation below follows that given by Wang and Flagan (1990).

There are two inlet flows into the DMA; the aerosol flow Q_a, and the sheath flow Q_{sh}. The sheath flow is a clean, dry gas stream which is used to separate the aerosol flow from the inner cylinder. The sheath flow is normally much larger than the aerosol flow, typically ten times larger. The sample outlet flow is denoted Q_s.

The voltage that is applied across the annulus creates a radial electric field. Neglecting end effects this field is;

$$E_r(r) = \frac{V}{r \ln \frac{r_1}{r_2}} = E_1 \frac{r_1}{r} , \tag{A.1}$$

where r_1 and r_2 are the radii of the collection rod and the outer cylinder respectively, V

is the voltage, and E_1 is the electric field at the collector rod surface.

The radial position of a particle with mobility Z_p varies with time as,

$$r^2(t) = r_{in}^2 + 2Z_p E_1 r_1 t \ , \tag{A.2}$$

where r_{in} is the radial position of the particle at the entrance to the analyzer column. Assuming uniform axial velocity, the time available for the particles to flow down the column is;

$$t_f = \frac{\pi\left(r_2^2 - r_1^2\right)L}{Q_a + Q_{sh}} \ , \tag{A.3}$$

where L is the distance between the aerosol entrance and the sample collection slot, Q_a is the aerosol inlet flowrate, and Q_{sh} is the sheath flowrate. At the aerosol entrance the particles are assumed to be uniformly distributed which means that some of the particles will start closer to the collection rod than others. Therefore the sample collected will contain a range of particles with different mobilities. There are two limiting cases, the first case is a large particle at the very inner edge of the inlet aerosol flow. This is the minimum mobility case and it can be found by substituting equation (A.2) into equation (A.1) with r_{in} being r_a. The minimum mobility is;

$$Z_{p,min} = \frac{Q_s - Q_{sh}}{2\pi r_1 E_1 L}, \tag{A.4}$$

where Q_s is the aerosol sampling rate form the DMA. Similarly the maximum mobility case can be found and it is for a smaller particle entering the DMA at r_1. The maximum mobility is;

$$Z_{p,max} = \frac{Q_a + Q_{sh}}{2\pi r_1 E_1 L}. \tag{A.5}$$

Only particles between these limits will contribute to the particles in the sample flow. Particles with intermediate mobilities will not be collected from all of the aerosol inlet flow. This means there is an instrument transfer function, Ω, describing the fraction of particles with a particular mobility that are collected. The transfer function for non diffusing particles is (Stolzenburg, 1988)

$$\Omega_{nd} = \frac{1}{2\beta\left(1-\delta\right)}\left[\left|\tilde{Z}_p - (1+\beta)\right| + \left|\tilde{Z}_p - (1-\beta)\right| - \left|\tilde{Z}_p - (1-\beta\delta)\right| - \left|\tilde{Z}_p - (1-\beta\delta)\right|\right] \tag{A.6}$$

where $\tilde{Z}_p$ is the dimensionless electric mobility, β and δ are dimensionless parameters. The parameters are defined by

$$\beta = \frac{Q_s + Q_a}{Q_e + Qsh} \tag{A.7}$$

$$\delta = \frac{Q_s - Q_a}{Q_s + Qa} \tag{A.8}$$

where Q_e is the excess flowrate from the DMA. The dimensionless electric mobility is defined as

$$\tilde{Z}_p = \frac{Z_p}{Z_p^*} = \frac{4\pi LVZ_p}{Q_e + Qsh} \ln\left(\frac{r_1}{r_2}\right), \tag{A.9}$$

where the centroid electric mobility is

$$Z_p^* = \frac{Q_e + Q_{sh}}{4\pi LV} \ln\left(\frac{r_1}{r_2}\right). \tag{A.10}$$

The particle mobility is found using the formula for the drag on the particle. It is;

$$Z_p = \frac{ieC_c}{3\pi\mu D_p}, \tag{A.11}$$

where i is the number of positive charges on the particle, e is the elementary unit of charge, μ is the gas viscosity and $C_c = C_c(Kn)$ is the Cunningham slip correction factor which accounts for the reduction in aerodynamic drag on a particle as the Knudsen number becomes large. These equations provide a relationship between size and diameter for the stepping mode.

The analysis of the SEMS mode is slightly more complicated. The electric field is not constant with time and the delay time between the DMA and the particle counter used must be taken into account. The voltage is varied exponentially which ensures that all particles with the same mobility follow the same path through the DMA. The analysis will not be shown for the SEMS mode as it progresses in a similar fashion to the stepping mode, see the paper by Wang and Flagan (1990) for more details.

A.2 Experimental

In order to carry out the agglomeration experiments described in the second chapter of this thesis, four Differential Mobility analyzers (DMAs) were required. Two DMAs used were the TSI 3077 cylindrical DMAs. The other two were the Caltech Cylindrical DMAs which had not previously been tested.

An experiment was devised to test the performance of the two types of cylindrical DMA. The aerosol needed had to be of known diameter and be easily produced with a steady concentration. Poly-styrene latex (PSL) particles from Duke Scientific were used. The PSL particles were diluted in distilled water and the resulting solution was atomized and passed to the DMA. The particles were counted with a TSI 3010 Condensation Nuclei Counter (CNC). For the TSI 3077 cylindrical DMA, the size distribution was scanned using an IBM PC to change the voltage in a 100 second SEMS scan. At the time of the experiment there was not a comparable program ready to run the Caltech DMA and so the size distribution was obtained by manually stepping the voltages and reading the output concentrations from the TSI 3010 CNC display.

Since the system used was identical except for the cylindrical DMA, the size inversion did not need to be inverted and comparisons were made using the raw data.

A.3 Results

The resulting size distributions from the scan of the TSI 3077 DMA and the step of the Caltech cylindrical DMA were plotted. The distributions can be seen in figure (A.1). Both DMAs show similar trends. The PSL solution contains poly-styrene latex particles as well as many surfactant compounds to stop the particles agglomerating in solution. Both DMAs have peaks at the same mobility diameter. There are four peaks that can be distinguished in the distribution, occurring at 120nm, 150nm, 180nm, and 220nm. The last peak at 220nm is from the PSL particles. The Caltech cylindrical DMA gives higher concentrations than the TSI 3077. There are three possible reasons for this. The Caltech DMA was designed to minimize particle losses as the aerosol stream enters and

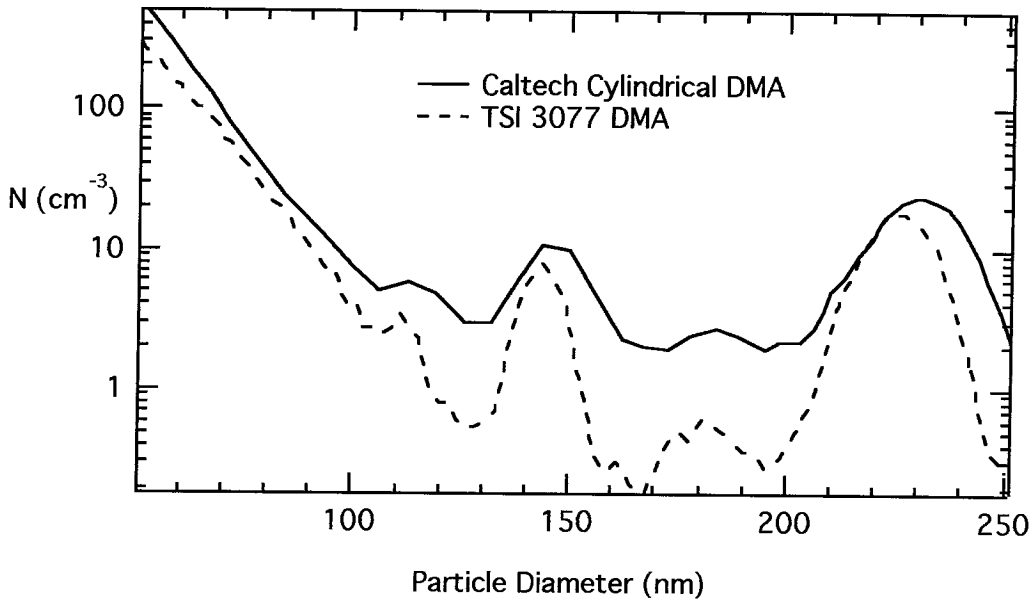

Figure A.1: A comparison of the Caltech and the T.S.I. 3077 Cylindrical DMAs.

flows through the instrument. Secondly the Caltech DMA was operated in stepping mode which avoids the lowering of peak height that occurs with fast SEMS scans. Thirdly the experiment required that the DMA be physically disconnected and the other DMA put in its place. The particle source may have changed in this time causing the difference in the two concentrations. However this would not have changed the peak sizes and these are seen to be similar between the two instruments.

The Caltech Cylindrical DMA has been used to size particles of known size and was compared with the TSI 3077 DMA. These experiments showed that the DMA could be used as a particle sizing instrument. To fully invert the size dstribution more experiments are necessary to determine the transmission efficiency of the DMA as a function of particle size. This experiment was carried out and can be found in Appendix Two.

Appendix B Caltech Cylindrical DMA Transmission Efficiency.

B.1 Introduction

One of the factors involved in inverting a size distribution is the DMA transmission efficiency. Particles can be lost in a DMA by inertial impaction in corners, diffusion to the walls of the tubing and by gravitational settling. The only way to accurately predict these losses is experimentally. The Caltech DMAs have a different design to the TSI 3071 DMA so the TSI transmission efficiency could not be used. The Caltech DMA was designed to minimize particle losses in the inlet and outlet sections of the instrument.

B.2 Experimental

A tandem DMA experiment was used to determine the transmission efficiency of the Caltech cylindrical DMA (see figure B.1). The first DMA was set at a voltage and is used to take a size cut from the particle source. This DMA is called the classifier DMA. The particles out of the first DMA are then passed to the second DMA which is set at the same voltage as the first DMA. The second DMA is called the analyzer DMA. By measuring the concentration of particles before and after the second DMA the transmission efficiency of the instrument can be calculated. Therefore the transmission efficiency η is;

$$\eta = \frac{\text{Concentration from Analyzer DMA}}{\text{Concentration from Classifier DMA}}. \tag{B.1}$$

The particle stream from the classifier DMA was switched between the CNC and the analyzer DMA by the use of two three-way valves. The length of tubing and the number of ninety degree bends was the same on each path. This avoids particle losses in the 1/4" copper tubing distorting the transmission efficiency. After a data point was taken the DMAs were set to the next voltage and the system was left for 5 minutes to allow steady state to be reached. This process was repeated until all the size range was covered.

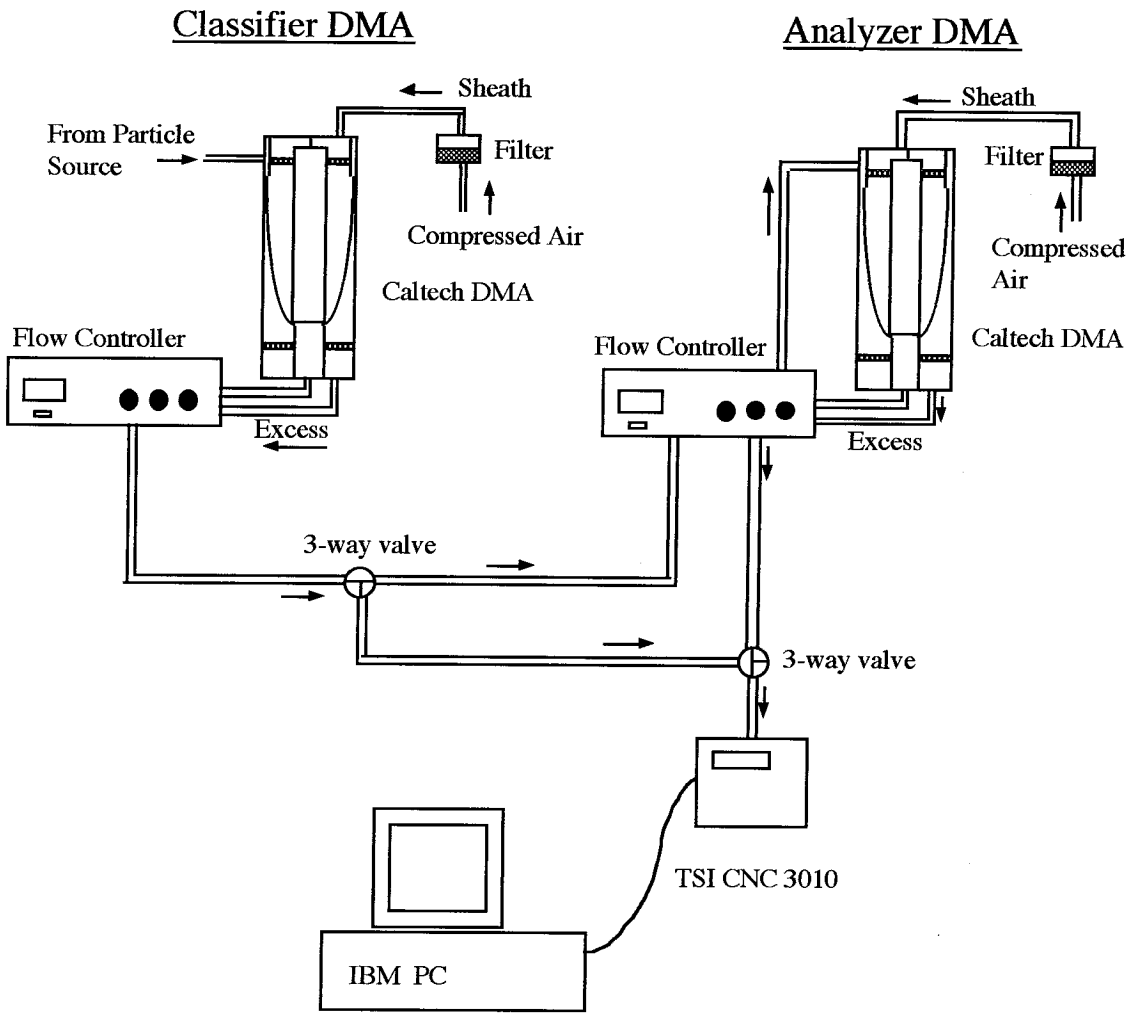

Figure B.1: Flow diagram of the Caltech cylindrical DMA transmission experiment.

B.3 Results

The transmission efficiency for each size was plotted versus particle diameter. A double exponential was fitted to the data. The curve of best fit for the transmission efficiency η is;

$$\eta = 61.5968 - 13.4742exp\left(-0.0283362D_p\right) - 87.0865exp\left(-0.145124D_p\right). \qquad \text{(B.2)}$$

The data and the fitted curve show the transmission efficiency to increase rapidly at small particle diameters. This increase is due to the decrease in particle diffusivity with increasing particle diameter. Larger particles diffuse more slowly to the walls of the DMA increasing the transmission efficiency.

Above 20nm the transmission efficiency tends to the limit of 66.6% as the particle diameter increases (see figure B.2). This limit is not reached as the particles are now lost by inertial impaction as well as diffusion. The largest particle diameter used in the experiment was 250 nm. At this size the efficiency was still close to the theoretical limit. At larger particle sizes, the transmission efficiency should decrease as inertial impaction becomes the dominant mechanism for particle loss.

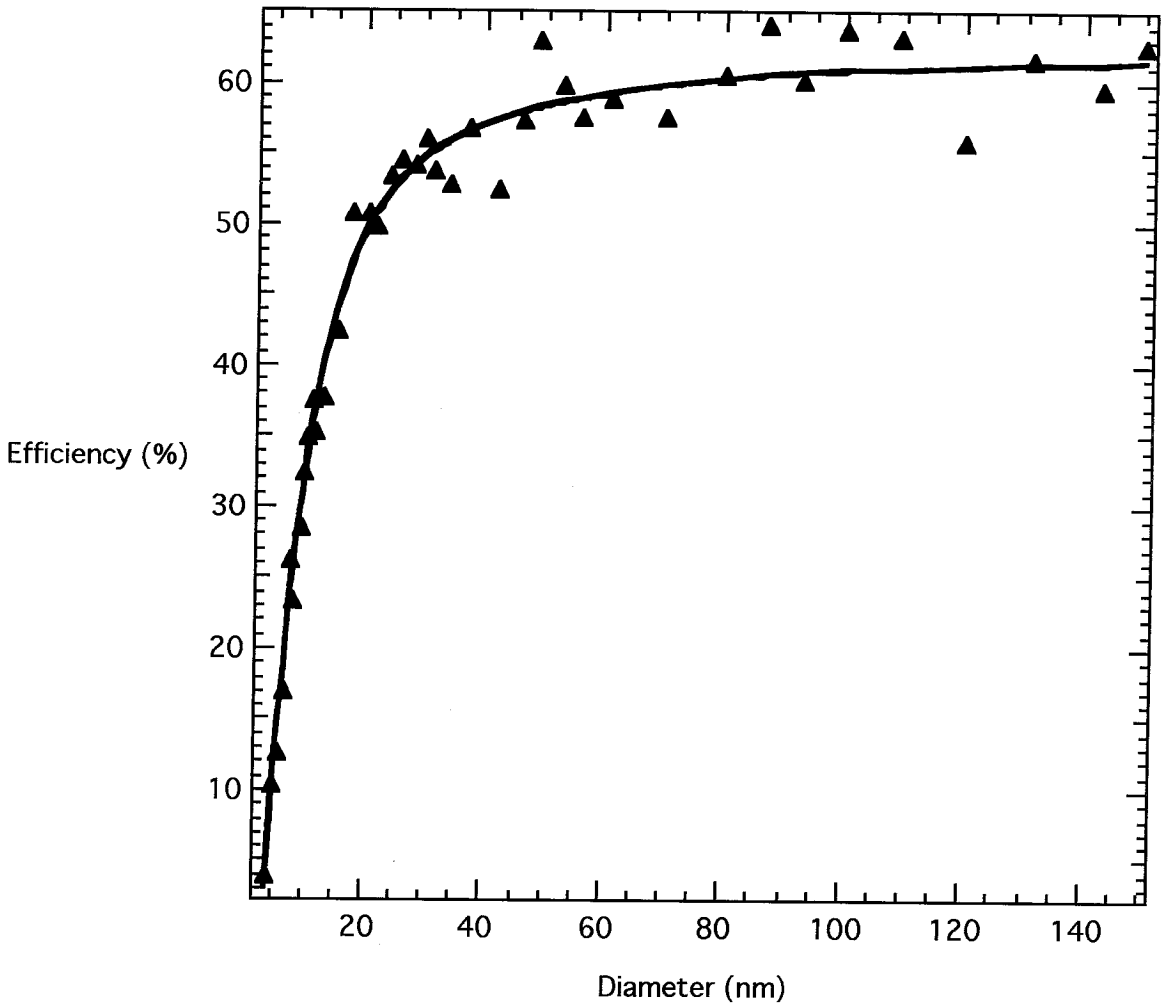

Figure B.2: The peak to peak transmission efficiency of the Caltech cylindrical DMA.

Appendix C Fortran Programs

C.1 Caltech Cylindrical DMA Distribution Inversion

In the agglomeration experiment in chapter two the Caltech Cylindrical DMAs were run simultaneously using the CAL22805.PAS program. The CAL22805.PAS program is an adaption of the SCN22805.PAS program written by Hali Forstner in 1994 to run two TSI 3077 DMAs simultaneously. The SCN22805.PAS program is in turn based on the SCAN2805.PAS program written by Shih-Chen Wang to run a SEMS scan using the TSI 3077 DMA. The SCAN2805.PAS uses a Data Translation 2805 A/D board to run the DMA voltage ramp and to take in the counts from the counting board.

The CAL22805.PAS differs from SCN22805.pas only in the procedure GetInvert-Table, where L, r1 and r2 are changed to the values of the Caltech cylindrical DMA. The Caltech Cylindrical DMAs have different dimensions to the TSI 3077 and therefore have a different voltage to diameter relation. Both programs run the DMAs with the same voltage on each DMA and use TSI 3760 CNCs to determine the particle concentrations. For the Caltech Cylindrical DMAs the inverted data that the program produces is not valid as the Caltech DMAs have different transmission efficiencies to the TSI 3077. Also the SCN22805.PAS program inverts the data assuming Fuch's distribution of charges and this is not valid for the $TiO_2.nH_2O$ agglomerates.

The CAL22805 program outputs time, mobility diameter and raw data for each second of the scan. This data was used to as an input to the size distribution program called DISTINV.FOR that was written to invert the Caltech cylindrical DMA data.

C.2 Size Distribution Inversion Theory

The counts measured by the CNC, N_i, differ from the number of particles entering the DMA in several ways. This relation is;

$$N_i = Q_a \int_{-\infty}^{\infty} n\left(D_p\right) \eta_{trans}\left(D_p\right)\ \eta_{cnc}\left(D_p\right)\ \Omega\left(Z_p\left(D_p =\right)\right)\ \rho(D_p)\ dD_p \tau_{count}, \qquad \text{(C.1)}$$

where; Q_a is the aerosol flowrate,
$n(D_p)$ is the real number of counts at size D_p,

η_{trans} is the transmission efficiency of the DMA,
η_{cnc} is the counting efficiency of the CNC used,
$\Omega\left(Z_p\left(D_p\right)\right)$ is the transfer function of the DMA,
$\rho(D_p)$ is the charging probability,
τ_{count} is the counting time of the CNC, one second in this study.

This equation is for a continuous size distribution. The data obtained from a SEMS scan is a discrete representation of the continuous distribution. A similar equation can be written with a sum instead of an integral and this is used in the program DISTINV.FOR to invert the CAL22805.PAS output data. The equation (C.1) becomes;

$$N_i = Q_a \ \ \tau_{count}\, n\left(D_p\right) \eta_{trans}\left(D_p\right) \ \ \eta_{cnc}\left(D_p\right) \rho(D_p) \sum_{i=1}^{imax} \Omega\left(Z_p\left(D_p\right)\right) \ \Delta D_p. \qquad \text{(C.2)}$$

This assumes that the charging probability, transmission efficiency, and the CNC counting efficiency are constants over the range of the transfer function. For our studies with the Caltech cylindrical DMA, the smallest particles analyzed had a diameter of 20nm and the flow ratio was 10:1. These conditions mean that the assumptions are valid over the ideal transfer function. The ideal transfer function is given in Appendix one for a cylindrical DMA.

The counting probability of the 3760 CNC for these experiments is assumed to be 1.00. The agglomerates of interest have mobility diameters over 20nm and in this range the 3760 counting efficiency approaches 1.00

The program gives two options for the charging probability. The user can choose either Fuchs charging distribution for +1 charge or use the +1 distribution for the $TiO_2.nH_2O$ agglomerates that was found experimentally. A detailed description of these experiments can be found in chapter two. The DMAs were always operated with a negative voltage applied between the concentric cylinders of the DMA and assumes that only particles with one positive charge are present. Multiple charging correction was carried out after the first data inversion by the program.

The transmission efficiency of the Caltech Cylindrical DMA can be found in Appendix two. The program uses the double exponential fit for the transmission efficiency.

The TSI 3760 CNC can count particle concentrations accurately up to 10,000 particles per cubic centimeter. Above this range coincidence errors become significant. To account for coincidence errors the following equation is used;

$$N_a = N_i \; exp\,(N_a \; Q \; t)\,, \tag{C.3}$$

where; N_a is the correct concentration (particles/ cm^3),
N_i is the indicated concentration (particles/ cm^3),
Q = 23.58 cm^3 sec^{-1},
t = 0.25 microseconds is the effective time each particle spends in the viewing volume. This equation is taken from the Model 3760 Condensation Nucleus Counter Instruction Manual from TSI.

C.3 Fortran Program for Caltech DMA Size Inversion

```
C     SEMS Size Distribution Inverter for the Caltech Cylindrical DMAs.
C     Written by Paul Drayton 11/8/95.
C     This program will take part of a 60 second scan from the
C     SEMS program and invert it, taking into account the DMA
C     transmission efficiency, the DMA transfer function, the
C     particle charging probability and the coincidence errors
C     in the 3760 TSI CNC.
C     The program first sets up an A matrix and then uses LU
C     decomposition to solve for the real counts. The two subroutines
C     LUDCMP and LUBKSB are taken from the numerical recipes in fortran
C     book by Press et al.
C     This program inverts two size distributions at once, but can
C     easily be altered to invert just one. The input file name and
C     the Y/N choice for the Fuchs charging must be entered
C     in apostrophes, e.g. 'Y'.
C
C     Defining the variables
C
      PROGRAM DISTINV
      IMPLICIT REAL (A-H,O-Z)
      INTEGER IN,INP
      CHARACTER*13 FNAME,HNAME
      DIMENSION A(60,60),W(60,60),B(60),DP(60),FIN1(60)
      DIMENSION RAW1(60),RAW2(60),SIGMA(60),VOLT(60),INDX(60)
C
C     Reading the input file
C
      WRITE(*,*)'INPUT THE DATA FILE THAT IS TO BE INVERTED'
      READ(*,*) FNAME
      OPEN(12,FILE=FNAME,ACCESS='SEQUENTIAL',STATUS = 'OLD')
```

```
      HNAME='SIZDIST.OUT'
      OPEN(13,FILE=HNAME,ACCESS='SEQUENTIAL',STATUS ='NEW')
C
C     Now enter all the constants needed in the inversion.
C
      WRITE(*,*)'Input no. of points in the size distribution'
      READ(*,*) IN
      INP=IN
C
C     Setting up the 60 by 60 matrix
C
      CALL DATAIN(DP,RAW1,RAW2,IN)
      WRITE(*,*)' Data File is Loaded'
      CALL VOLTS(DP,VOLT,QSH,QS,QA,QCNC,IN)
      WRITE(*,*) 'Now Setting up A matrix'
C
      CALL ASETUP(A,DP,RAW1,VOLT,QSH,QS,QA,QCNC,SIGMA,B,IN,W)
      WRITE(*,*)'A Matrix complete'
C
      CALL LUDCMP(A,IN,INP,INDX,D)
      WRITE(*,*)' First LU decomposition done'
C
      CALL LUBKSB(A,IN,INP,INDX,B)
      WRITE(*,*)'First Inversion done'
C
C     Have inverted the first size distribution, now to do the second.
C     Need to store the output from the LUBKSB subroutine in the INV1
C     array.
C
      DO 700 I=1,IN,1
      FIN1(I) = B(I)
      B(I) = RAW2(I)
700   CONTINUE
C
```

```
      CALL LUDCMP(W,IN,INP,INDX,D)
      WRITE(*,*)' Second LU decomposition done'
      CALL LUBKSB(W,IN,INP,INDX,B)
      WRITE(*,*)'Second Inversion done'
C
C     Store the results of the size inversion in the output file
C
      DO 800 I=1,INP,1
      WRITE(13,900) I,DP(I),FIN1(I),B(I)
900   FORMAT (2X,I2,3(2X,E15.8))
800   CONTINUE
      END
C
C
      SUBROUTINE DATAIN(DP,RAW1,RAW2,IN)
      IMPLICIT REAL (A-H,O-Z)
      DIMENSION DP(IN),RAW1(IN),RAW2(IN)
      DO 1000 I=1,IN
      READ (12,*) TIME, DP(I), RAW1(I), DN1, RAW2(I), DN2
1000  CONTINUE
C
C     Correct for coincidence errors in the TSI 3760 counter.
C
      DO 1020 J=1,IN
      RAW1(J) = RAW1(J)*EXP(RAW1(J)*23.58*.25e-6)
      RAW2(J) = RAW2(J)*EXP(RAW2(J)*23.58*.25e-6)
1020  CONTINUE
      RETURN
      END
C
C
      SUBROUTINE VOLTS(DP,VOLT,QSH,QS,QA,QCNC,IN)
      IMPLICIT REAL (A-H,O-Z)
      DIMENSION VOLT(IN),DP(IN)
```

```
      DMALEN = 0.4119
      R2 = 0.0192024
      R1 = 0.0094488
      PI = 3.1415926
      ECHARGE = 1.602E-19
      VISCOS = 1.81E-5
      WRITE(*,*)'SHEATH FLOW (l/min) ='
      READ(*,*) QSH
      WRITE(*,*)'SAMPLE FLOW (l/min) ='
      READ(*,*) QS
      WRITE(*,*)'AEROSOL FLOW (l/min) ='
      READ(*,*) QA
      WRITE(*,*)'Enter the flow from the counter (l/min) ='
      READ(*,*) QCNC
      QCNC = QCNC /60.0 * 1.0E-3
      QSH = QSH /60.0 * 1.0E-3
      QA = QA /60.0 * 1.0E-3
      QS = QS /60.0 * 1.0E-3
      QT = QSH + QA
      DO 1200 I=1,IN
      CONKN = 1.302E-7 / (DP(I)*1.0e-9)
      CC = 1.0 + CONKN*(1.257 + 0.40*EXP(-1.1/CONKN))
      ZPI = ECHARGE*CC/(3.0*VISCOS*PI*DP(I)*1.0e-9)
C
C     Now calculate voltage for each second of the scan.
C
      VOLT(I)=(QT-0.5*(QS+QA))*(LOG(R2/R1))/(2.0*PI*DMALEN*ZPI)
1200  CONTINUE
      RETURN
      END
C
C
      SUBROUTINE ASETUP(A,DP,RAW1,VOLT,QSH,QS,QA,QCNC,SIGMA,B,IN,W)
      IMPLICIT REAL (A-H,O-Z)
```

```
      CHARACTER*1 FUCHCHAR
      DIMENSION A(IN,IN),SIGMA(IN),B(IN),W(IN,IN)
      DIMENSION RAW1(IN),VOLT(IN),DP(IN)
      WRITE(*,*) 'Do you want Fuchs Charging Probability?(Y/N)'
      READ(*,*) FUCHCHAR
      DMALEN = 0.4119
      R2 = 0.0192024
      R1 = 0.0094488
      PI = 3.1415926
      ECHARGE = 1.602E-19
      VISCOS = 1.81E-5
      QT = QSH+QA
C
C     Calculating Charging Probability for all particle sizes. This
C     program gives you the choice of the distribution from the
C     TiO2nH2O agglomerates that were generated in the TTIP source
C     or the Fuchs distribution found in the paper by A. Wiedensohler
C     in the J.Aerosol Sci, Vol 19 No. 3 pp 387-389, 1988
C     Note: This assumes +1 charge, so you'll have to modify the
C     program if you want to include multiple charging effects.
C
      DO 1300 J=1,IN
      FUCHCON = ALOG10(DP(J))
      IF((FUCHCHAR.EQ.'Y').OR.(FUCHCHAR.EQ.'y')) THEN
      CHARPRO = 100*10**(-2.3484 +0.6044*FUCHCON
     &  +0.4800*FUCHCON**2.0 +0.0013*FUCHCON**3.0
     &  -0.1553*FUCHCON**4.0 +0.0320*FUCHCON**5.0)
      ELSE
      CHARPRO = -16.671 +1.3585*DP(J) -0.017926*(DP(J)**2.0)
     &  +0.00010579*(DP(J)**3.0) - 2.924E-7*(DP(J)**4.0)
     &  +3.0764E-10*(DP(J)**5.0)
      ENDIF
C
C     Calculating Transmission Efficiency for Caltech DMAs.
```

```
C
      TRANEFF = 61.5968 - 13.4742*EXP(-0.0283362*DP(J))
&     -87.0865*EXP(-0.145124*DP(J))
C
C     Calculating Transfer Function for the Caltech cylindrical DMA.
C
      DO 1400 K=1,IN
      CONKN = 1.302E-7/(DP(K)*1.0e-9)
      CC = 1.0+CONKN*(1.257 + 0.40*EXP(-1.1/CONKN))
      ZPK = ECHARGE*CC/(3.0*VISCOS*PI*DP(K)*1.0e-9)
      E1 = VOLT(J)/(R1*LOG(R1/R2))
      CONSTK = -2.0*PI*R1*E1*ZPK*DMALEN
      CONST1 = (QS-QSH+CONSTK)/QA
      CONST2 = (QA+QSH-CONSTK)/QA
C
C     CONST3 = QS/QA. For this program QS=QA.If it doesn't in your case you
C     will need to change the program here and in the logic commands to
C     determine SIGMA(K). Also to account for dilution before the counter
C     the factor QCNC/QA was added. This assumes that the aerosol flow
C     equals the monodisperse flow. If it doesn't then you'll have to
C     add a line to input QMONO and change the dilution factor to
C     QMONO/QCNC.
C
      IF (CONST1.LT.CONST2) THEN
      SIGMA(K) = CONST1
      ELSE
      SIGMA(K) = CONST2
      ENDIF
C     IF (CONST3.LT.SIGMA(K)) THEN
C     SIGMA(K) = CONST3
C     ENDIF
      IF (SIGMA(K).GE.1.0) THEN
      SIGMA(K) = 1.0
      ENDIF
```

```
      IF (SIGMA(K).LT.0.0) THEN
      SIGMA(K) = 0.0
      ENDIF
      A(J,K) = SIGMA(K)* CHARPRO * TRANEFF *1.0E-4 *QA/QCNC
      W(J,K) = A(J,K)
1400  CONTINUE
1300  CONTINUE
C
C     Now have the A matrix for the decomposition, need the b array.
C
      DO 1500 I=1,IN
      B(I) = RAW1(I)
1500  CONTINUE
      RETURN
      END
C
C
      SUBROUTINE LUDCMP(A,IN,INP,INDX,D)
      IMPLICIT REAL (A-H,O-Z)
      PARAMETER(INMAX=100,TINY=1.0E-20)
      DIMENSION A(INP,INP),VV(INMAX),INDX(IN)
C     INTEGER INDX(IN)
      D = 1.0
      DO 12 I=1,IN
      AAMAX=0.0
      DO 11 J=1,IN
      IF (ABS(A(I,J)).GT.AAMAX) THEN
      AAMAX=ABS(A(I,J))
      ENDIF
11    CONTINUE
      IF (AAMAX.EQ.0.) PAUSE 'Singular matrix.'
      VV(I)=1./AAMAX
12    CONTINUE
      DO 19 J=1,IN
```

```
      IF (J.GT.1) THEN
      DO 14 I=1,J-1
      SUM=A(I,J)
      IF (I.GT.1)THEN
      DO 13 K=1,I-1
      SUM=SUM-A(I,K)*A(K,J)
13    CONTINUE
      A(I,J)=SUM
      ENDIF
14    CONTINUE
      ENDIF
      AAMAX=0.
      DO 16 I=J,IN
      SUM=A(I,J)
      IF (J.GT.1)THEN
      DO 15 K=1,J-1
      SUM=SUM-A(I,K)*A(K,J)
15    CONTINUE
      A(I,J)=SUM
      ENDIF
      DUM=VV(I)*ABS(SUM)
      IF (DUM.GE.AAMAX) THEN
      IMAX=I
      AAMAX=DUM
      ENDIF
16    CONTINUE
      IF (J.NE.IMAX)THEN
      DO 17 K=1,IN
      DUM=A(IMAX,K)
      A(IMAX,K)=A(J,K)
      A(J,K)=DUM
17    CONTINUE
      D=-D
      VV(IMAX)=VV(J)
```

```
      ENDIF
      INDX(J)=IMAX
      IF(J.NE.IN)THEN
      IF(A(J,J).EQ.0.)A(J,J)=TINY
      DUM = 1./A(J,J)
      DO 18 I=J+1,IN
      A(I,J)=A(I,J)*DUM
18    CONTINUE
      ENDIF
19    CONTINUE
      IF(A(IN,IN).EQ.0.)A(IN,IN)=TINY
      RETURN
      END
C
C
C
      SUBROUTINE LUBKSB(A,IN,INP,INDX,B)
      IMPLICIT REAL (A-H,O-Z)
      DIMENSION A(INP,INP),INDX(IN),B(IN)
      II=0
      DO 25 I=1,IN
      LL=INDX(I)
      SUM = B(LL)
      B(LL) = B(I)
      IF(II.NE.0)THEN
      DO 24 J=II,I-1
      SUM = SUM - A(I,J)*B(J)
24    CONTINUE
      ELSE IF(SUM.NE.0.) THEN
      II=I
      ENDIF
      B(I) = SUM
25    CONTINUE
      DO 27 I=IN,1,-1
```

```
      SUM=B(I)
      IF (I.LT.IN) THEN
      DO 26 J=I+1,IN
      SUM=SUM-A(I,J)*B(J)
26    CONTINUE
      ENDIF
      B(I) = SUM / A(I,I)
27    CONTINUE
      RETURN
      END
```

C.4 Agglomeration Simulation Program, REACSIM.FOI

```
C     This program is a numerical simulation of the 3.5m long reactor
C     used by Paul Drayton for coagulation studies. It simulates the
C     coagulation of two sizes of particles. It uses the number
C     concentrations of each size at the start and the K11 and K22
C     coagulation coefficients, and the estimated K12 coagulation
C     coefficient to calculate the output concentrations.
C     Written by Paul Drayton (17/1/96)
C     Reminder don't forget the 's.
C
      PROGRAM REACSIM
      IMPLICIT REAL (A-H,O-Z)
      INTEGER RESTIME,I
      CHARACTER*1 PARAM,RERUN,PARAM2
100   WRITE(*,*)'Input number Conc1 at time zero(#/cm3)'
      READ(*,*) C10
      WRITE(*,*)'Input number Conc2 at time zero(#/cm3)'
      READ(*,*) C20
      WRITE(*,*) 'Input coagulation Rate11 (cm3/s)'
```

```
      READ(*,*) R11
      WRITE(*,*) 'Input coagulation Rate22 (cm**3/s)'
      READ(*,*) R22
300   WRITE(*,*)'Input estimate of coagulation Rate12 (cm**3/s)'
      READ(*,*) R12
      WRITE(*,*)'Do you want to change ALL the parameters? (Y/N)'
      READ(*,*) PARAM
      IF((PARAM.EQ.'Y').OR.(PARAM.EQ.'y')) THEN
      GOTO 100
      ELSE
      ENDIF
      RESTIME = 360
      C1T = C10
      C2T = C20
      DO 600 I = 1,RESTIME
      DELTA1 = - R11*C1T**2 - R12*C1T*C2T
      DELTA2 = - R11*C2T**2 - R12*C1T*C2T
      C1T = C1T + DELTA1
      C2T = C2T + DELTA2
600   CONTINUE
      WRITE (*,*) C10,C1T,C20,C2T
      WRITE(*,*)'Do you want to run again? (Y/N)'
      READ(*,*) RERUN
      IF((RERUN.EQ.'N').OR.(RERUN.EQ.'n')) THEN
      GOTO 800
      ELSE
      ENDIF
      WRITE(*,*)'Do you want to change JUST R12? (Y/N)'
      READ(*,*) PARAM2
      IF((PARAM2.EQ.'Y').OR.(PARAM2.EQ.'y')) THEN
      GOTO 300
      ELSE
      ENDIF
      IF((PARAM2.EQ.'N').OR.(PARAM2.EQ.'n')) THEN
```

```
      GOTO 100
      ELSE
      ENDIF
800   WRITE (*,*) 'GOOD BYE'
      END
```